4-23-2012 12:00 AM

Investigation of the Use of Micro-Mechanical Testing to Analyze the Mechanical Anisotropy of the Zr-2.5%Nb Pressure Tube Alloy

Richard O. Oviasuyi, *The University of Western Ontario*

Supervisor: Robert J. Klassen, *The University of Western Ontario*

A thesis submitted in partial fulfillment of the requirements for the Doctor of Philosophy degree in Mechanical and Materials Engineering

INVESTIGATION OF THE USE OF MICRO-MECHANICAL TESTING TO ANALYZE THE MECHANICAL ANISOTROPY OF THE ZR-2.5%NB PRESSURE TUBE ALLOY

(Spine title: Analyzing the Mechanical Anisotropy of the Zr-2.5%Nb Pressure Tube)

(Thesis format: Integrated Article)

by

Richard Omorodion Oviasuyi

Graduate Program in Engineering Science
Department of Mechanical & Materials Engineering

A thesis submitted in partial fulfillment
of the requirements for the degree of
Doctor of Philosophy

The School of Graduate and Postdoctoral Studies
The University of Western Ontario
London, Ontario, Canada

THE UNIVERSITY OF WESTERN ONTARIO
School of Graduate and Postdoctoral Studies

CERTIFICATE OF EXAMINATION

Supervisor

_____
Dr. Robert J. Klassen

Supervisory Committee

_____
Dr. John R. Dryden

_____
Dr. Xueliang. A. Sun

Examiners

_____
Dr. Jeff Wood

_____
Dr. Ovidiu-Remus Tutunea-Fatan

_____
Dr. Amin Rizkalla

_____
Dr. Brad Diak

The thesis by

Richard Omorodion Oviasuyi

entitled:

Investigation of the use of Micro-Mechanical Testing to Analyze the Mechanical Anisotropy of the Zr-2.5%Nb Pressure Tube Alloy

is accepted in partial fulfillment of the
requirements for the degree of
Doctor of Philosophy

_____ _____
Date Chair of the Thesis Examination Board

Abstract

Maintaining a safe operation of nuclear power plants is the primary requirement of nuclear power generating organizations worldwide. This necessitates the use of highly effective methods for assessing the mechanical properties of reactor materials and components. This is important since all components located in a nuclear reactor core experience high levels of neutron irradiation which cause defects to be formed in the metals' crystal structure. The density of these crystal defects increases with increasing exposure to neutrons and cause the crystalline metal to become harder and simultaneously more brittle. This change in mechanical properties is potentially detrimental to the safe performance of the nuclear reactor.

The use of two micro-mechanical testing techniques for assessing the mechanical anisotropy of a common Zr-2.5%Nb alloy pressure tube material used in CANDU reactors will be evaluated. Three different types of experiments were performed; the first two were based upon the use of uniaxial compression of cylindrical pillars while the third was based on the use of spherical micro-indentation. The techniques, and their subsequent data analysis, are presented. It is then demonstrated how these techniques can be applied to assess the anisotropic yield stress and work-hardening behavior of the test material, both in its as-received and its Zr^{+} irradiated conditions, over a temperature range from 25^{o}C to 300^{o}C.

Data from uniaxial compression tests on extruded and cold-drawn Zr-2.5%Nb pressure tube were used to determine the Hill's anisotropy coefficients F = 0.38 $\pm$ 0.01, G = 0.202 $\pm$ 0.001 and H = 0.62 $\pm$ 0.01. These coefficients were found to be independent of temperature and plastic strain. The calculated *F*, *G* and *H* values were then used to determine the equivalent stress versus equivalent plastic strain for this pressure tube. These values were also used to modify the yield stress value used in spherical indentation equations in deducing average stress-strain curves for mechanically anisotropic materials.

Keywords: Micro-mechanical testing, Uniaxial compression testing, Micro-pillar compression testing, Spherical indentation testing, Mechanical anisotropy, Equivalent stress, Equivalent plastic strain, Hill's anisotropy coefficients, Zr-2.5%Nb

Co-Authorship Statement

The research presented in this thesis is composed of three manuscripts, one published and two under review in the Journal of Nuclear Materials, which are co-authored by Richard Omorodion Oviasuyi and Dr. Robert J. Klassen.

The experiments, data analysis and manuscript drafting were performed by Richard Omorodion Oviasuyi. The data interpretation and editing of the manuscript were performed by Dr. Robert J. Klassen.

Dedications

To my beloved Mom and Dad,

Lady Victoria Eboikpomwen & late Sir Samson Eboikpomwen

Acknowledgments

I wish to express my sincere gratitude to Professor Robert J. Klassen for his time, support, guidance and ideas provided throughout this project. Without his help, the successful completion of this thesis and the quality of work achieved would not have been possible. His contributions and help are greatly appreciated.

I also wish to thank my past and present colleagues whom I worked with at our Micro Mechanical testing laboratory, and all those who have been involved with this project one way or the other for their time and support.

Table of Contents

List of Figures

List of Tables

Nomenclature

Symbols	Definition
F	Hill's Anisotropy Coefficient in the axial normal direction
G	Hill's Anisotropy Coefficient in the transverse normal direction
H	Hill's Anisotropy Coefficient in the radial normal direction
β	βeta-Zr, Angle of contact between the tangent to the indenter at the point of contact and the sample surface
β'	βeta-Nb
α	Alpha-Zr, Angular direction in the plane of a tube
L	Liquid phase
P_{ref}	Measured property in a crystal direction
$P_{[0001]}$	Single crystal properties parallel to the [0001] direction
$P_{\perp[0001]}$	Single crystal properties perpendicular to the [0001] direction
V_i	Volume fraction of crystals in a [0001] direction
ϕ_i	Tilt angle to reference direction
f	Summation of orientation parameter
σ	Flow Stress, True Stress
σ_0	Initial Yield Stress
σ_y	Yield Stress
σ_{ij}	Multiaxial Applied Stress
$\sigma_{xx}, \sigma_{yy}, \sigma_{zz}$	Normal Stresses acting in the x, y and z directions
$\sigma_{xy}, \sigma_{yz}, \sigma_{zx}$	Shear Stresses on the plane perpendicular to the *i* axis in the direction of the *j* axis
σ_{ind}	Indentation Stress
$\bar{\sigma}_{ind}$	Equivalent Indentation Stress
σ_e	Engineering Stress
σ_{eq}, $\bar{\sigma}$	Equivalent Stress
σ_{avg}	Average Stress

ε_e	Engineering Strain
ε_p	Plastic Strain
$\varepsilon_{p\,eq}$, $\bar{\varepsilon}_p$	Equivalent Plastic Strain
$\bar{\varepsilon}_{ind}$	Equivalent Indentatation Plastic Strain
ε_{avg}	Average Strain
K, A	Material Strength, Material Constant
n	Work Hardening Exponent
Q	Thermal Activation Energy
R	Boltzmann Constant
T	Temperature
h_c	Contact Displacement / Depth
h_f	Plastic Displacement / Depth
h, δ	Displacement
h_{max}	Maximum Displacement / Depth
h_s	Elastic displacement of the material from the original position
P, F	Indentation Force
P_{max}, F_{max}	Maximum Indentation Force
P_m	Mean Contact Pressure
c	Pile-up or Sink-in factor, Ratio of maximum strain to minimum strain
S	Initial slope of unloading curve in a F-h curve
D	Indenter Diameter
φ	Constraint Factor
a	Radius of the indentation
a_c, r_c	Contact Radius
E	Elastic Modulus
E^*	Reduced Modulus
d	Diameter of the indentation
R	Indenter Radius
ϕ	Plasticity / Dimensionless Parameter
T	Temperature

Abbreviations	**Definition**
CANDU	CANada Deuterium Uranium
PT	Pressure Tube
D_20	Deuterium oxide (Heavy water)
^2H	Deuterium
Zr	Zirconium
Nb	Niobium
Zr-2.5%Nb	Zirconium 2.5% wt. Niobium
AN, A	Axial Normal
RN, R	Radial Normal
TN, T	Transverse Normal
F_A	Calculated Basal Pole Fractions parallel to the axial direction along the (0001) plane of the pressure tube
F_R	Calculated Basal Pole Fractions parallel to the radial direction along the (0001) plane of the pressure tube
F_T	Calculated Basal Pole Fractions parallel to the transverse direction along the (0001) plane of the pressure tube
FIM	Field Indentation Microprobe
ABI	Automated Ball Indentation
NDE	Non-Destructive Evaluation
BHN	Brinell Hardness Number

Chapter 1

1. Introduction

1.1. Background

The development of the CANDU[1] reactor system can be traced as far back as 1898 when Lord Rutherford, a pioneer in the field of atomic physics was appointed Professor of Experimental Physics at McGill University. However, the development of nuclear reactors for commercial production of electricity in many countries including Canada did not start until the early 1950's. After a careful consideration of possible designs, Canadians recognized the unique advantages of the pressurized heavy water reactors. This choice enabled the reactor to be fueled with natural uranium, thus avoiding the need to either build costly uranium enrichment plants or the importation of enriched fuel. CANDU reactors can operate on the use of natural uranium because deuterium (heavy water) has a low neutron absorption cross-section [1-3]. However, the use of deuterium for neutron moderation and cooling will require the construction of very large pressure vessels. To avoid this situation, CANDU reactors utilize the fuel channel design which incorporates the pressure tube. The service life of the fuel channel is determined by the pressure tube since it is the component within the unit that is subjected to the most severe conditions during operation. In the last few years, tremendous improvements have been made to the Zr-2.5%Nb pressure tubes which have resulted in them having longer service lives and greater safety margins.

All metal components located in a nuclear reactor core experience high levels of neutron irradiation. The interaction of the neutrons with the metal atoms causes defects to be formed in the metals' crystal structure. The density of these crystal defects, which are typically of the form of atomic point defects (referred to as Frenkel Pairs) or very small dislocation loops, increases with increasing exposure to neutrons and cause the crystalline metal to become harder and simultaneously more brittle (i.e. to become irradiation

[1] The acronym CANDU refers to CANada Deuterium Uranium and refers to a type of thermal neutron fission reactor that utilizes non-enriched uranium fuel and neutron moderation via heavy water.

hardened and irradiation embrittled). This change in mechanical properties is potentially detrimental to the safe performance of the metal components. Two common consequences of these radiation induced changes on the pressure tube properties include a change in dimensions of the tube often referred to as radiation induced deformation and a decrease in the resistance to fracture resulting in a reduction in toughness of the tube.

1.2. Need for research

Maintaining a safe operation of nuclear power reactors is the primary requirement of operation codes used by all nuclear power generating organizations worldwide. This necessitates the use of highly effective methods of detection and mitigation of degraded reactor systems, structures and components throughout the design service life of the plant. Nuclear power reactor operators carry out periodic maintenance, testing, and examination of all mechanical components located within the reactor core. In the case of the CANDU reactors, this inspection process can be quite involved due to the complexity of the core (figure 2.1).

The latest fuel channels have been designed to have a lifespan of over 30 years. These channels, and in particular the pressure tube, are considered to have reached their end of service life when they can no longer meet their design and service demands. The combination of neutron flux, high temperature and pressure induced stresses over time results in a degradation of the properties of the pressure tubes. To an extent, the pressure tubes have been designed to accommodate extreme working conditions, but cracking have seldom occurred during operation [4-6]. Although the current CANDU reactor design has the capacity to withstand the consequences of a rupture of the pressure tube, researchers continue to strive to minimize the possibility of a fracture. The cost penalties of an unscheduled shutdown in operation in order to carry out repairs associated with any rupture and determine their cause has huge economic implications on the plant. Also, if such ruptures began to occur frequently, there would be an increase in the risk of them escalating to a more serious accident.

Despite the large pool of information available on the design, operation and maintenance of CANDU nuclear reactors, researchers are still very interested in finding new and more

effective methods to mechanically test these components for deterioration from the influence of stress, temperature, irradiation etc., and to determine whether they are still safe for operation. The fact that material removed from a nuclear reactor is highly radioactive, and therefore exceedingly difficult to test with conventional mechanical tests, means that new methods of small-sample mechanical testing must be devised to allow for the direct assessment of the mechanical strength and ductility of irradiated components extracted from in-service nuclear reactors.

1.3. Scope and objectives of this research

This thesis focuses on finding new techniques for testing the mechanical anisotropy of the Zr-2.5%Nb pressure tube. Mechanical anisotropy is a common property in metals that arises from their crystal structure or by virtue of their manufacturing route. The Zr-2.5%Nb pressure tube is predominantly made up of over 97% Zirconium, an element that possesses an hcp crystal structure, whose single crystals are anisotropic in addition to the large amount of cold-working the pressure tube has been subjected to during fabrication. This implies that their mechanical properties like yield stress and elastic modulus would change with direction. It is therefore necessary to test these tube's properties with respect to direction. The experiments performed in this thesis are tailored towards determining the anisotropic stress – strain curves for the CANDU pressure tube with respect to their orthogonal directions. This study does not extend to the kinetics of the local plastic deformation of the tubes but considers the mechanisms of the deformation in a bid to explain some of the results obtained from these tests. Experiments are performed at room temperature and also at elevated temperatures of 100, 200 and 300 °C with respect to direction, to assess the effect of temperature on the deformation process.

In order to achieve these goals, new methods for testing irradiated pressure tubes from nuclear reactors will be explored. Three new types of experiments will be performed and studied using different techniques. The results from the tests will be compared to those already published in order to verify the effectiveness of my experimental approach. The first two experiments are based upon the use of uniaxial compression of macro- and micro-sized cylindrical pillars while the second is based on the use of spherical indentation to determine the yield stress and the work-hardening behavior of the test

sample. These techniques will be used to assess the effect of temperature and irradiation hardening on the mechanical anisotropy of extruded and cold-drawn Zr-2.5%Nb CANDU pressure tube material.

1.4. Structure of thesis

The structure of this thesis is in accordance with the Integrated Article Format of the school of Graduate and Post-graduate studies (SGPS) at The University of Western Ontario, ON, Canada. It is made up of six chapters, three of which are experimental research designed to investigate new methods for testing irradiated pressure tubes from nuclear reactors.

Chapter two of this thesis presents a review of the relevant previously published information related to CANDU nuclear reactors, the plastic deformation of mechanically anisotropic Zr-2.5%Nb pressure tubes, in both the irradiated and the non-irradiated conditions, used in CANDU fuel channels, and the theory describing the complex stress/strain state invoked during spherical indentation. As the test material used in this thesis is extruded and cold-drawn Zr-2.5%Nb CANDU pressure tubing, it will be of importance to briefly discuss the manufacturing process, which leads to its uniquely elongated microstructure and crystallographic texture. The use of ion irradiation to simulate the effect of neutron irradiation on the microstructure of these components will be discussed. The effect of temperature on the mechanical properties of pressure tubes and their properties will also be discussed, and finally a description of the theory and principle behind the use of spherical micro-indentation to deduce stress-strain curves that are similar to those obtained from uniaxial tensile / compression tests will also be discussed.

Chapter three will cover the use of standard uniaxial compression tests to assessing the anisotropic yield stress and work-hardening behaviour of the extruded and cold-drawn Zr-2.5%Nb pressure tube material. The use of the compression test is widely accepted in research and its results have been used to effectively characterize. The results of these tests will be used to determine Hills anisotropy factors, F, G, and H that describe the mechanical anisotropy of this material over the temperature range from ambient to

300^{o}C. This chapter has been submitted for publication in the Journal of Nuclear Materials [R.O. Oviasuyi, R.J. Klassen, (02-15-2012)].

Chapter four presents the results of a study of the use of spherical micro-indentation to determine the stress - plastic strain response of mechanically anisotropic material. The results from spherical indentation tests performed on non-irradiated Zr-2.5%Nb samples over a range of temperature from 25^{o}C to 300^{o}C are compared with equivalent data from the uniaxial macro- and micro-pillar tests to validate this new indentation-based test method. This chapter has been submitted in the Journal of Nuclear Materials [R.O. Oviasuyi, R.J. Klassen, (03-06-2012)].

Chapter five will describe a new micro-mechanical testing technique that uses uniaxial compression testing of small (5 μm) diameter micro-pillars to determine the yield stress and work-hardening rate of extruded and cold-drawn Zr-2.5%Nb pressure tube material. The small size of these micro-pillars allows them to be used to assess the mechanical properties of ion-irradiated pressure tube material and, therefore, allows for an assessment to be made of the role of irradiation hardening on the degree of anisotropy of the yield stress and the work-hardening rate of the Zr-2.5%Nb pressure tube material. This chapter has been published in the Journal of Nuclear Materials [R.O. Oviasuyi, R.J. Klassen, J. Nucl. Mater. 421 (2012) 54].

Chapter six presents a discussion of all the results from the previous chapters and comes up with a final assessment of: i) the effect of neutron irradiation on the mechanical anisotropy of extruded and cold-drawn Zr-2.5%Nb pressure tube material and ii) the usefulness of uniaxial micro-pillar compression and spherical indentation for obtaining the equivalent stress-plastic strain response of mechanically anisotropic material and, ultimately the usefulness of these techniques as in-cell automated tests for assessing the mechanical response of radioactive nuclear materials.

1.5. Contributions

This research introduces a variety of new testing techniques that can be developed and applied to the testing of both as-received and neutron irradiated nuclear reactor

components. While the use of uniaxial tensile and compression tests of conventional sized samples have been used for a long time in evaluating the mechanical properties of the pressure tube, the use of spherical micro-indentation and compression of micro-sized pillars in the testing of these tube materials have never been performed.

The use of spherical micro-indentation offers a new dimension because it can be used to assess the local properties of the components at regions of interest and doesn't require the preparation of full-sized testing specimens. It is a Non-Destructive-Test that requires the polishing of the sample surface on which the test is to be performed after which the material is then deformed with a spherical indenter. While spherical micro-indentations tests are well established for testing isotropic materials, its use in the characterization of anisotropic materials is scarce. This technique has been introduced for testing anisotropic materials by modifying the plasticity parameter to account for the anisotropy of the deformation process. The results obtained in my study were comparable to those obtained using conventional tensile testing techniques.

The use of micro-pillar compression testing has become common in testing small volumes of material. This testing technique will be applied in studying the effect of high levels of self-similar ion irradiation damage in a bid to simulate the effect of neutron irradiation on the pressure tube material. The results obtained using this technique were found to also be very comparable to results obtained using other techniques, thus making it very effective.

References

[1] G.L. Brooks, A Short History of the CANDU Nuclear Power System, Ontario Hydro Demand/Supply Plan Hearing, 1993.

[2] J.R. Lamarsh, A.J.Baratta, Introduction to Nuclear Engineering, Prentice Hall, 2001.

[3] C.E. Coleman, B.A. Cheadle, C.D. Cann, J.R. Theaker, ASTM STP, 1295 (1996) 884.

[4] IAEA Report on Assessment and Management of ageing of Major Nuclear Power Plant Components Important to Safety, IAEA-TECDOC_1037, 1998.

[5] R. Dutton, A Layman's Guide to Radiation-Induced Deformation Processes in Zirconium Alloys, AECL-10158, 1990.

[6] L.C. Walters, A.F. Williams, CANDU Fuel Bundle Deformation Model, AECL, 2003.

Chapter 2

2. Review of the relevant literature

The purpose of this research is to assess the effectiveness of two micro-mechanical testing techniques to obtain data that are equivalent to those from conventional large-specimen mechanical tests. All experimental results reported in this thesis were obtained from tests performed on Zr-2.5%Nb CANDU pressure tube material and therefore, it is important to first give a brief description of the operation of a CANDU nuclear reactor and the method by which the pressure tubes are fabricated. Previous work on expressing the mechanical anisotropy of textured Zr-2.5%Nb CANDU pressure tube are then discussed and then finally, the theory and principles involved with pillar (macro-sized and micro-sized) compression testing and spherical micro-indentation testing are presented.

2.1. The CANDU nuclear reactor

The CANDU nuclear reactor design uses heavy-water (D_2O) for cooling and for neutron moderation. Two primary advantages of this design are: i) its ability to operate with natural, non-enriched, uranium fuel and ii) its ability to refuel specific fuel channels within the core while the reactor continues to operate. These features are accomplished by using a reactor core that consists of a very large horizontal cylindrical tank, the calandria vessel, which contains the D_2O moderator along with about 380 horizontal fuel channels each extending the length of the tank (Figure 2.1). Each fuel channel contains twelve fuel bundles within a Zr-2.5%Nb pressure tube [1-3]. Zirconium alloys are used for the structural components throughout a CANDU reactor core because zirconium metal has a very low tendency to absorb neutrons which greatly improves the neutron efficiency of the core.

Figure 2.2 shows a cut away illustration of a fuel channel assembly used in a CANDU reactor. Pressurized D_2O coolant enters one end of the Zr-2.5%Nb pressure tube at about 250 °C to 270 °C and passes over the fissioning uranium fuel pellets located within the

pressure tube. The heat generated from the fission process increases the temperature of the coolant to 300 °C to 310 °C by the time it exits the pressure tube.

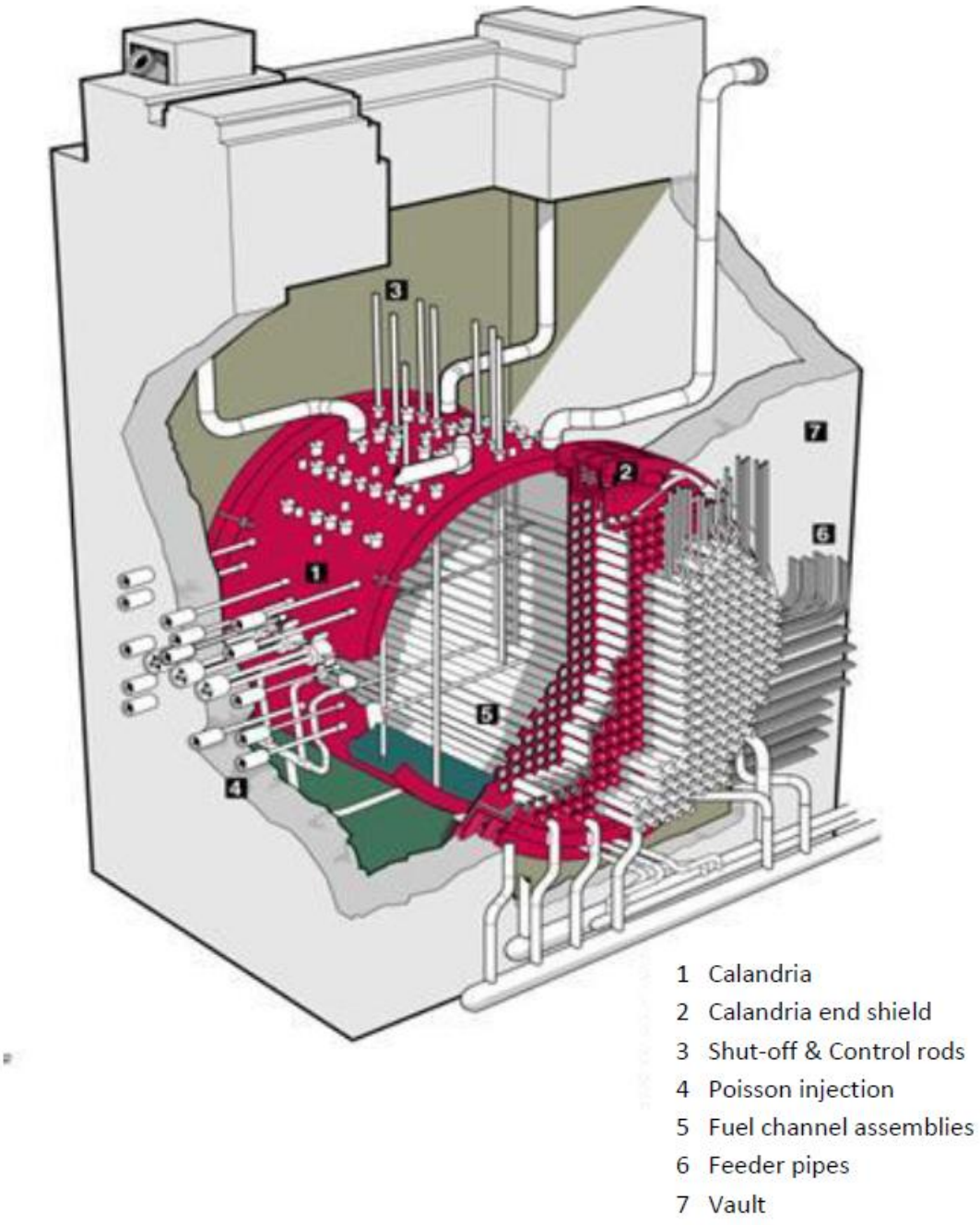

Figure 2.1. The core of a CANDU nuclear reactor showing the calandria vessel containing about 380 fuel channel assemblies [1].

To minimize heat loss from the pressure tube to the surrounding D_2O neutron moderator, an insulating gas annulus is contained between the outer surface of each pressure tube and a thin walled zirconium alloy tube referred to as the calandria tube (Figure. 2.2). The ring-like annulus spacers located between the calandria tube and the pressure tube wraps around the pressure tube, holding it in a central position and prevents sagging of the tube.

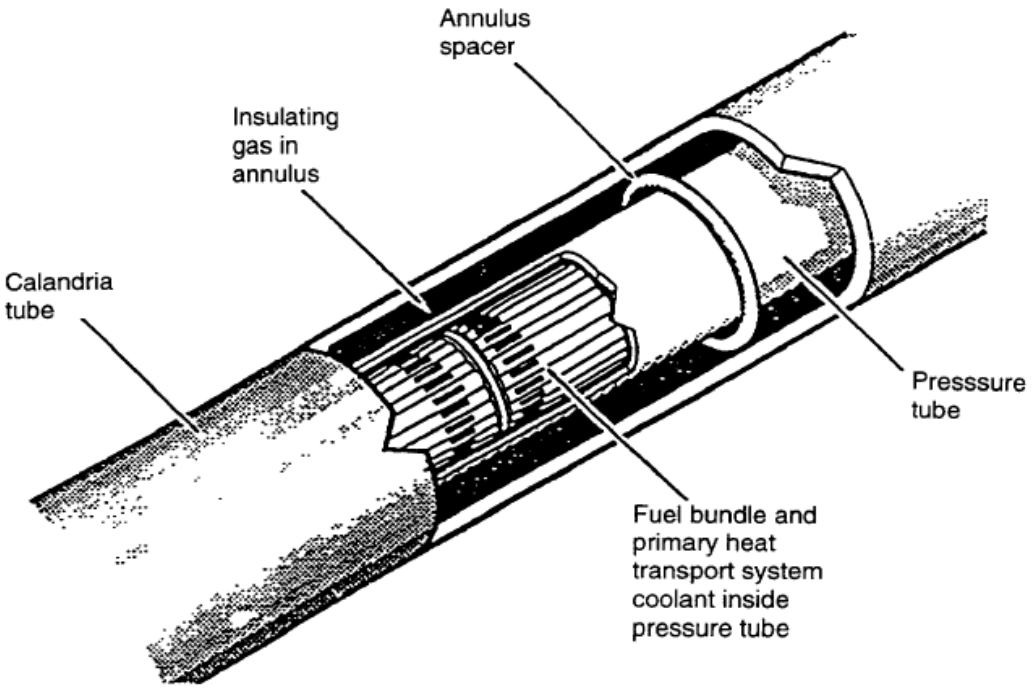

Figure 2.2. An illustration showing a cut-away section of a CANDU fuel channel revealing the primary components like the fuel bundle, pressure tube, and the thin-walled calandria tube [2].

2.2. The CANDU pressure tube

The seamless Zr-2.5%Nb pressure tubes used in CANDU nuclear reactors are fabricated through an extrusion and cold-drawing process. The chemical composition of the Zr-2.5%Nb pressure tube alloy is shown in Table 2.1.

Element Name	% Composition
Zirconium	97.2 – 97.5
Niobium	2.4 – 2.6
Oxygen	0.09 – 0.12
Iron	0.1
Carbon	0.03
Chromium	0.02
Tantalum	0.02
Hafnium	0.01

Table 2.1. Tabular presentation of the elements contained in a reactor grade Zr-2.5%Nb alloy and their percentage composition.

A CANDU pressure tube is approximately 6 m in length, 100 mm inner diameter, and 4 mm thick. A typical Zr-2.5%Nb pressure tube is fabricated by the following steps (Figure 2.3).

i) Ingot fabrication:

Zirconium silicate ore is refined to produce a porous pure zirconium sponge material which is then compacted into briquettes along with additions of other metals such as niobium to attain the desired composition (Table 2.1). The briquettes are electron beam welded together to form long rods that are then transferred to a consumable electrode arc furnace to be melted into Zr-2.5%Nb ingots. The ingots are about 0.6 m in diameter. Each ingot has a capacity to form between 30 and 40 pressure tubes [2].

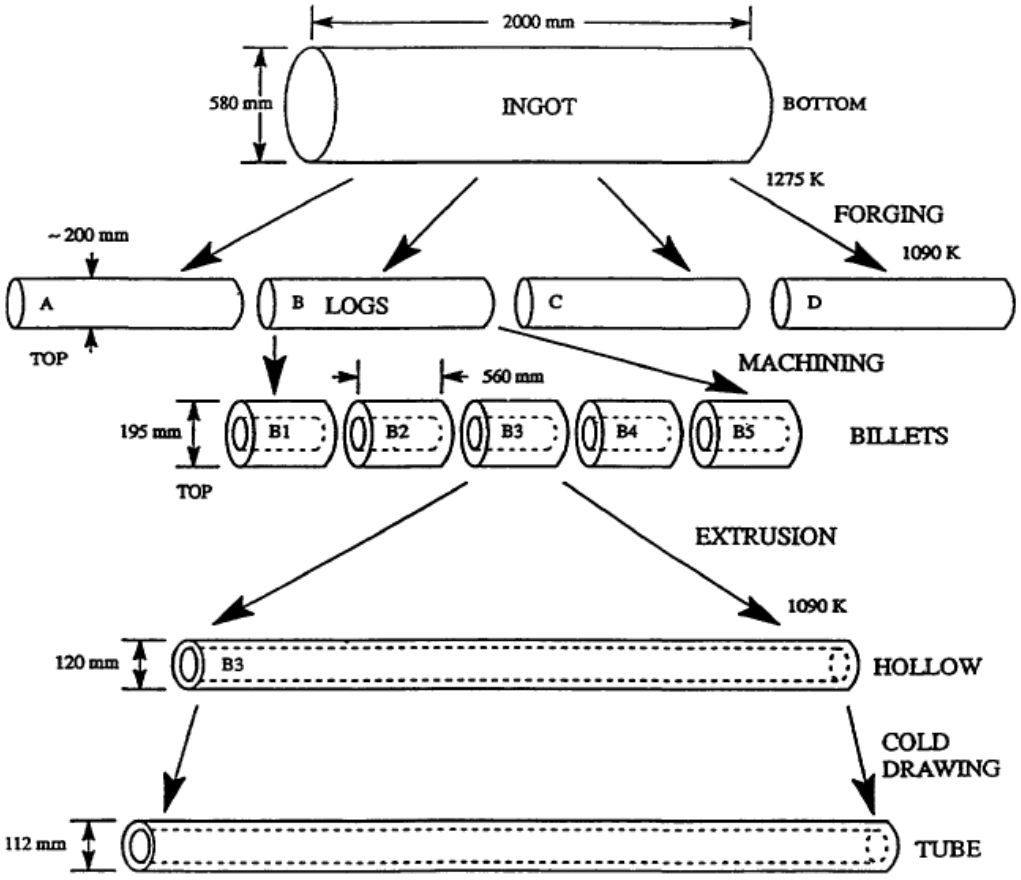

Figure 2.3. A detailed illustration of the production route for a typical Zr-2.5%Nb CANDU pressure tube [2].

ii) Forging the ingot:

The ingots are forged, using a press and rotary forges, into cylindrical "logs" of 0.2m diameter at a temperature of around 1000°C. A hole is then drilled through the centre of the log to create a hollow billet. The billets are then quenched from a temperature of 1000°C, within the 100% bcc β-phase region of the Zr-2.5%Nb alloy (Figure 2.4), to create a consistent microstructure of refined hcp α phase grains [2].

iii) Extrusion of the billets:

The hollow quenched billets are then preheated to about 815°C and extruded, with an extrusion ratio of 10.5:1, into hollow tubes. The extrusion temperature corresponds to the (α+β)-phase field of the Zr-2.5%Nb alloy (Figure 2.4). Air-cooling of the extruded tubes

from this temperature results in a dual-phase microstructure consisting of large grains of the hcp α phase, the primary constituent of the microstructure, which are elongated in the axial, extrusion, direction of the tube surrounded by a thin film consisting of about 25% bcc β'-phase lathes and 75% hcp α-phase grains. The average grain size of the α-phase is about 0.2, 1.0 and 5.0 μm in the radial, circumferential and axial directions of the tube respectively [4]. An important feature of this microstructure is that the extrusion process results in the crystal structure of the hcp α phase grains being highly aligned (i.e. textured) with the <0001> basal pole direction of most of the grains aligned along the circumferential direction of the tube. The extent of this texture is depicted by the pole figure (Figure 2.5) which shows the degree of orientation of the <0002> basal pole direction along the Axial (A), Radial (R), and Transverse (T) directions of the Zr-2.5%Nb tube.

iv) Cold-drawing of the extruded tubes:

The extruded tubes are then cold-drawn in two passes to a total reduction of cross-sectional area between 24 to 30%. The inner part of tubes is then honed to remove any surface flaws while the outside surface undergoes grinding to achieve the specified tube thickness. The final tube is then stress relieved at 400°C for 24 hrs in a steam autoclave to reduce the residual elastic strain remaining from the previous forming operations and to create a protective surface oxide layer [2].

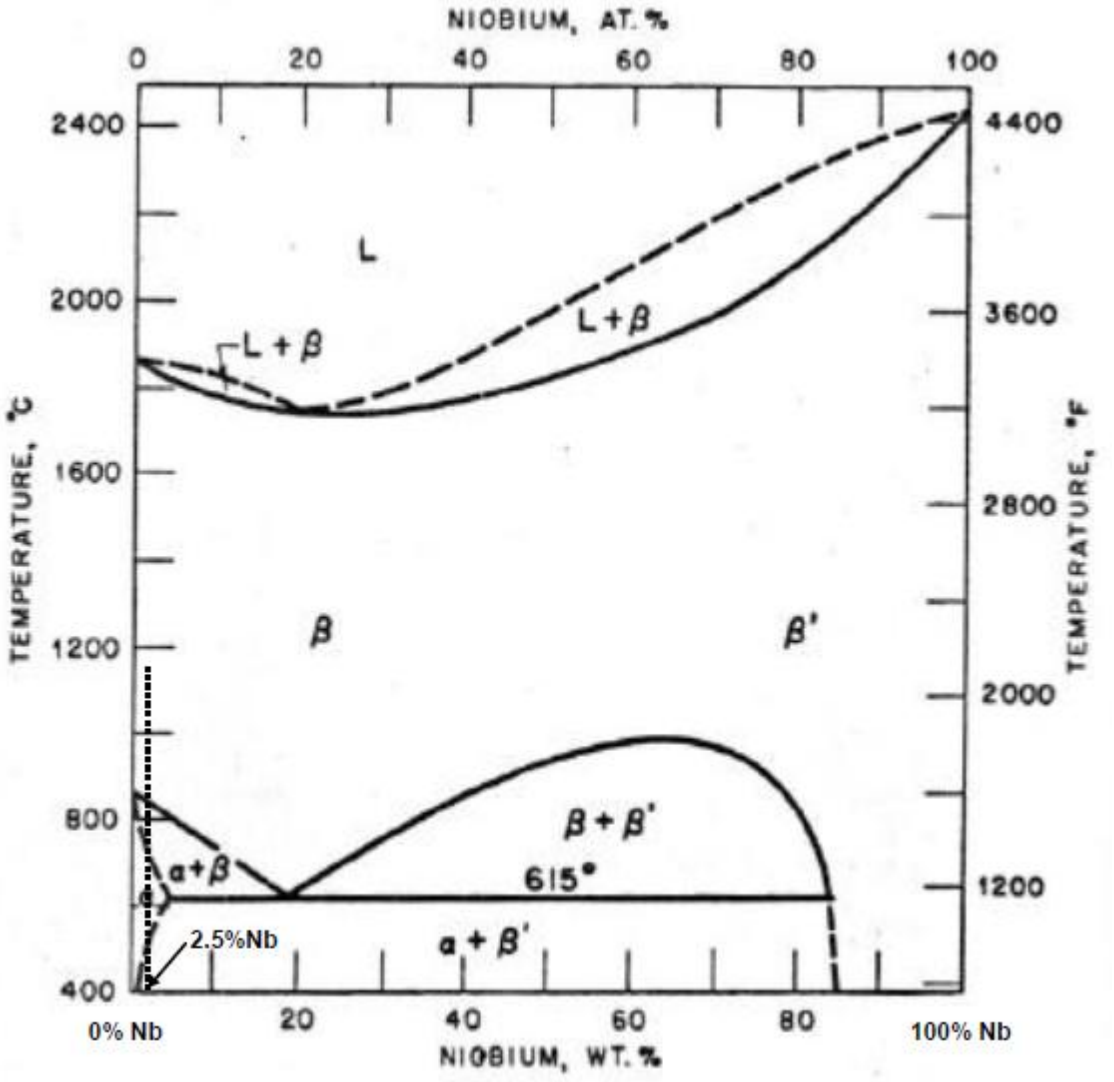

Figure 2.4. The Zirconium-Niobium equilibrium binary phase diagram. In this figure, *L* refers to liquid phase, *β* refers to β-Zr, *β′* refers to β-Nb and *α* refers to α-Zr [5].

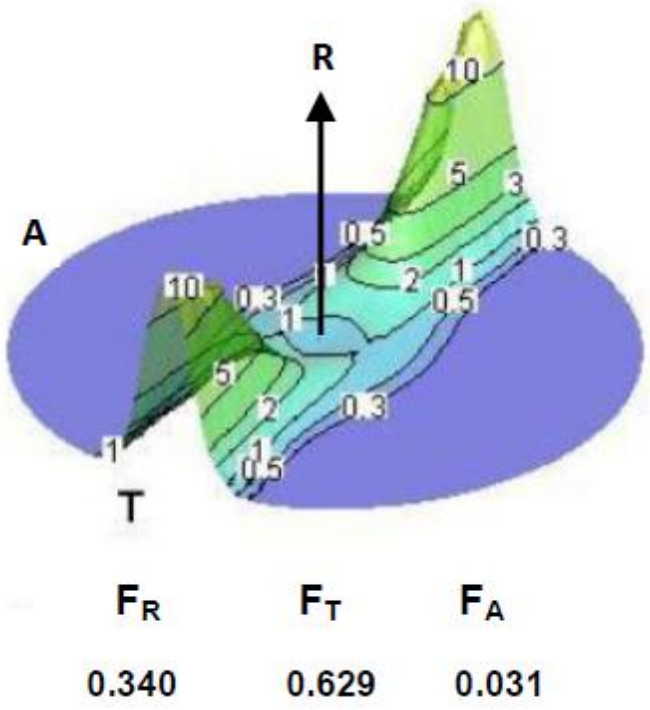

Figure 2.5. X-ray diffraction pole figure indicating the preferential alignment of the <0002> basal poles along the circumferential (transverse) direction of a typical extruded and cold-drawn Zr-2.5%Nb pressure tube. (F_R), (F_T) and (F_A) refer to the calculated basal pole fractions aligned parallel to the radial, transverse, and axial directions respectively along the (0001) plane of the tube. This pole figure and the pressure tube material used in this study were provided by AECL.

2.2.1. The crystallographic texture of Zr-2.5%Nb pressure tubes

Most of the mechanical properties exhibited by Zr-2.5%Nb pressure tubes are a result of its crystallographic texture associated with its fabrication route. This texture is controlled by the direction of major strain during the billet extrusion and the subsequent cold-drawing stages [6-8]. The mechanical yield stress of single crystal hcp α-phase zirconium is considerably larger along the <0001> direction than along any other direction thus the crystallographic texture of the extruded and cold-drawn Zr-2.5%Nb pressure tubes, with its high proportion of <0001> basal plane normals aligned in the transverse

(circumferential) direction, has optimal resistance to hoop stress resulting from the pressurized D_2O coolant. Another advantage of the textured microstructure is that it has been shown to result in improved resistance to delayed hydride cracking and irradiation induced deformation [8-9].

It is acknowledged with this material that single crystal anisotropic behavior is evident in the difference in yield stress values obtained when measured along different orientations of the crystal. One technique of characterizing preferred orientation in hcp materials is by the use of X-rays. When making use of this method of analysis, it is assumed that the bulk property in any direction set as a reference in a polycrystalline sample is the weighted summation of this property in its individual crystals. For hcp single crystals, Kearns [10] found that the contribution to the bulk property will depend on the angle between the reference direction and the [0001] crystal direction, and can be expressed using the equation:

$$P_{ref} = P_{[0001]}cos^2\phi + P_{\perp[0001]}(1 - cos^2\phi) \tag{2.1}$$

In Eq. (2.1), P_{ref} refers to the measured property in the crystal direction chosen as reference, $P_{[0001]}$ and $P_{\perp[0001]}$ represents the material single crystal properties parallel and perpendicular to [0001] direction respectively and ϕ is a measure of the angle between the reference direction and [0001]. To estimate the volume fraction V_i of crystals that have their [0001] oriented at a tilt angle of ϕ_i to the reference direction, X-ray measurements are performed on the material and the results obtained using Eq. (2.1) is used to estimate their contribution to the property exhibited by the test sample. The property of the bulk sample in the reference direction can then be calculated from the summation of $\phi_i = 0$ to $\phi_i = \pi/2$ using Eq. (2.2).

$$P_{ref} = P_{[0001]}\sum V_i cos^2\phi_i + P_{\perp[0001]}\sum V_i - P_{\perp[0001]}\sum V_i cos^2\phi_i \tag{2.2}$$

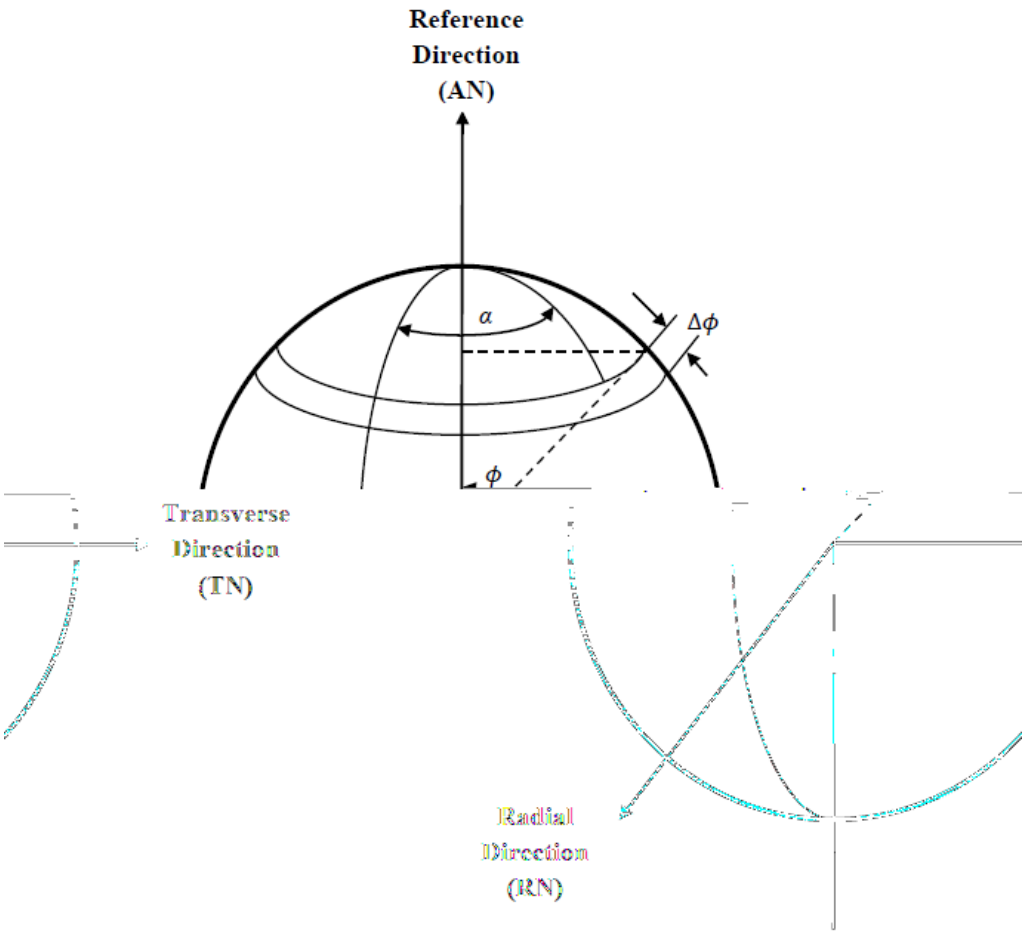

Figure 2.6. Schematic illustration of an intersecting reference sphere showing (0001) poles of a random sample [10].

In order to simplify our expression, a single parameter *f* defined as the summation of the orientation parameter can be introduced and expressed as:

$$f = \sum V_i cos^2 \phi_i \tag{2.3}$$

Equation (2.3) can be expressed in the form of an integral as:

$$f = \int_0^{\pi/2} I(\phi)\, sin\phi\, cos^2\phi\, d\phi \tag{2.4}$$

The function $I(\phi)sin\phi$ is used to obtain the volume distribution of crystals as a function of orientation while f, defined earlier as the orientation parameter refers to the effective fraction of cells aligned with their [0001] axis parallel to the reference direction [10]. Equation 2.2 can then be defined as:

$$P_{ref} = f\ P_{[0001]} + (1\ - f)P_{\perp[0001]} \tag{2.5}$$

The function f therefore has a single value used to calculate anisotropic material properties from data obtained from single crystal data. When this method of analysis is applied to a tube such as the CANDU reactor pressure tubes, the value of f will resolve the random distribution of [0001] orientations into an effective fraction aligned in each of the three principal directions of the tube. When the value of f is either 0 or 1.0, it implies that there is a perfect alignment of the [0001] crystals in the perpendicular or parallel direction, respectively, to the direction of interest.

The sum of f in the three principal directions gives a value equal to unity and a value of 1/3 in each direction defines a state of isotropy. The angle ϕ is the tilt of (0001) poles to the reference direction and α is the direction in the plane of the tube [10].

2.2.2. The deformation of Zr-2.5%Nb pressure tubes

The Zr-2.5%Nb pressure tubes undergo continuous deformation while in service in a CANDU nuclear reactor. The rate of this deformation can vary from tube to tube since it depends upon several factors including the microstructure of the tube, the magnitude of the components of the applied stress, the temperature, the neutron flux and the accumulated neutron fluence [11]. The strong crystallographic texture of Zr-2.5%Nb pressure tubes causes their yield strength and resistance to time-dependent creep and growth deformation[2] to be strongly anisotropic.

High levels of neutron flux, such as that endured by the central regions of the pressure tubes, cause the continuous input of energy, and thus continuous atomic displacements, to

[2] In nuclear materials, time-dependent deformation resulting from the application of an external stress is referred to as creep deformation while time-dependent deformation resulting in the absence of an external applied stress is referred to as growth. The presence of high levels of neutron flux in nuclear reactors can cause the metals to undergo considerable irradiation-driven growth.

the pressure tube material. For example, the central region of a Zr-2.5%Nb PT can endure approximately 30 displacements per atom over its forty year lifetime in a CANDU reactor as a result of neutron bombardment. These atomic displacements both harden the material and cause the creep and growth rate of the pressure tube to increase by facilitating both the motion of dislocations past obstacles and the anisotropic diffusion of irradiation-induced crystal defects within the material (resulting in the volume-conserving shape change of the material referred to as irradiation growth). One primary objective of this thesis is to study the effect of irradiation induced crystal damage (i.e. irradiation hardening) on the anisotropic plastic flow properties of Zr-2.5%Nb pressure tubes. Therefore the studies reported in subsequent chapters focus only on the effect of prior accumulated irradiation damage, and not on the effect of continuous irradiated damage, on the anisotropic plastic flow properties of the pressure tube material.

2.3. Constitutive equations describing the plastic deformation of Zr-2.5%Nb tubes

When a metal sample is subjected to an applied stress, it initially deforms elastically until the applied stress exceeds a certain yield condition σ_0, beyond which the material deforms plastically. During plastic deformation most metals undergo a certain amount of strain-hardening where an increase in plastic strain leads to a corresponding increase in the yield stress, referred to as the flow stress, beyond the initial yield stress σ_0. The dependence of the flow stress upon plastic strain ε_p is often expressed by the following empirically-based power-law expression:

$$\sigma\left(\varepsilon_p, T\right) = \left(\sigma_0 + K\varepsilon_p^n\right)e^{-Q/RT} \tag{2.6}$$

where σ_0, K, n, and Q are material-specific constants.

Under uniaxial loading macroscopic plastic deformation begins at the uniaxial yield σ_y however the initiation of plastic yielding when a material is subjected to a multiaxial applied stress σ_{ij} is thought to occur when more complex yield criteria is met. Perhaps the most common yield criteria used to predict the onset of plastic deformation in metals

subjected to multi-axial loading is that proposed by von Mises [12] which can be expressed as

$$\bar{\sigma} = \sigma_{yield} = \frac{1}{\sqrt{2}}\left[\left(\sigma_{xx} - \sigma_{yy}\right)^2 + \left(\sigma_{yy} - \sigma_{zz}\right)^2 + \left(\sigma_{zz} - \sigma_{xx}\right)^2 + 6\left(\sigma_{xy}^2 + \sigma_{yz}^2 + \sigma_{zx}^2\right)\right]^{1/2} \qquad (2.7)$$

where $\bar{\sigma}$ is referred to as the von Mises equivalent stress, σ_{yield} is the uniaxial yield stress of the material, the remaining stress terms on the right hand side of the equation are the components of the applied stress tensor σ_{ij}. The corresponding von Mises equivalent plastic strain $\bar{\varepsilon}_p$ is then given as

$$\bar{\varepsilon}_p = \frac{2}{3}\left[\frac{3}{2}\left(\varepsilon_{\sigma_{xx}}^2 + \varepsilon_{\sigma_{yy}}^2 + \varepsilon_{\sigma_{zz}}^2\right) + \frac{3}{4}\left(\varepsilon_{\sigma_{xy}}^2 + \varepsilon_{\sigma_{yz}}^2 + \varepsilon_{\sigma_{zx}}^2\right)\right]^{1/2} \qquad (2.8)$$

where the plastic strain terms on the right hand side of the equation are the components of the resulting plastic strain tensor $\varepsilon_{p_{ij}}$. The dependence of $\bar{\sigma}$ upon $\bar{\varepsilon}_p$ then follows the power-law form given in Eq. 2.6.

As plastic deformation progresses the mechanical properties, including the plastic flow stress, of the deforming material becomes more anisotropic. Individual crystal grains become elongated in the direction of loading resulting in a deformation-induced crystallographic texture. In the case of a hcp structured material, such as the Zr-2.5%Nb used in this study, the basal planes gradually rotate towards an orientation such that their normal vector, the basal plane normal, is aligned to the direction of loading. The deformation of isotropic materials can be extended to cater for anisotropy in materials whose crystals have a preferred orientation. To simplify this approach, consideration will only be given to states of anisotropy that possess three mutually orthogonal planes of symmetry at every point. The von Mises yield criterion can be modified to account for the effect of anisotropy in the material. Following the method proposed by R. Hill in 1948 [13] the von Mises equation (Eq. 2.7) can be modified as follows to describe the equivalent stress and the yield condition for a mechanically anisotropic material

$$\bar{\sigma} = \sigma_{yield} = \left[F\left(\sigma_{xx} - \sigma_{yy}\right)^2 + G\left(\sigma_{yy} - \sigma_{zz}\right)^2 + H\left(\sigma_{zz} - \sigma_{xx}\right)^2 + 2\left(L\sigma_{xy}^2 + M\sigma_{yz}^2 + N\sigma_{zx}^2\right)\right]^{1/2} \quad (2.9)$$

In this equation *F, G, H, L, M,* and *N* are experimentally obtained constants determined such that, for any multiaxial loading condition the resulting $\bar{\sigma}$ at the initiation of plastic yielding corresponds to the uniaxial yield stress σ_{yield} along a prescribed direction in the sample.

We can obtain the anisotropy factors *F, G,* and *H* by performing uniaxial tensile stress tests to determine the uniaxial yield stress in the x, y, and z directions of the material and then applying the following relations:

$$\begin{aligned} F &= \frac{1}{2}\left(\frac{1}{\sigma_{yield_y}^2} + \frac{1}{\sigma_{yield_z}^2} - \frac{1}{\sigma_{yield_x}^2}\right) \\ G &= \frac{1}{2}\left(\frac{1}{\sigma_{yield_z}^2} + \frac{1}{\sigma_{yield_x}^2} - \frac{1}{\sigma_{yield_y}^2}\right) \\ H &= \frac{1}{2}\left(\frac{1}{\sigma_{yield_x}^2} + \frac{1}{\sigma_{yield_y}^2} - \frac{1}{\sigma_{yield_z}^2}\right) \end{aligned} \quad (2.10)$$

For experiments in which the yield loci is calculated using crystallographic analysis and where the yield loci of the samples tend not to be elliptical, Hill proposed a modified criterion where under normal loading, the anisotropy can be estimated as a non-quadratic criterion in the form

$$F\left|\sigma_y - \sigma_z\right|^a + G\left|\sigma_z - \sigma_x\right|^a + H\left|\sigma_x - \sigma_y\right|^a = 1 \quad (2.11a)$$

where *a* has a value much greater than 2 and depends on the value of the average strain ratio *R* at a strain of 20%. Another yield criterion for analyzing the anisotropy of materials is the Logan-Hosford yield criterion for anisotropic plasticity that takes the form similar to the Hill's non-quadratic criterion (Eq. 2.11a)

$$F\left|\sigma_y - \sigma_z\right|^n + G\left|\sigma_z - \sigma_x\right|^n + H\left|\sigma_x - \sigma_y\right|^n = 1 \qquad (2.11b)$$

The primary difference between the two criteria is that in (Eq. 2.11a), the value of *a* depends on the value of *R* while in (Eq. 2.11b), the value of *n* is independent of this ratio. Other yield criteria exist for analyzing the anisotropy of metals but are more complex and need the determination of more material constants from experiments [14]. The cylindrical macro-pillars used for our compression tests had elliptical cross-sections after deformation, and hence the Hill's quadratic criterion (Eq. 2.9) which is simple and self-sufficient for this purpose was used in our analysis of the anisotropy of the Zr-2.5%Nb CANDU pressure tube in this study.

2.4. Development and representation of crystallographic texture

Predicting the anisotropy of polycrystals from single crystal properties involves two fundamental steps: (a) determination of texture by measuring the orientations of all crystals and data processing for presenting the texture in a suitable form; and (b) execution of a physically accurate averaging analysis for combining single crystal properties into polycrystal behaviour. For a comprehensive treatment, mechanical interaction between the individual grains of a polycrystal must be analyzed in a similar manner as using the model of Eshelby and Kröner where a grain is treated as an elastic inclusion in a homogeneous matrix with the average properties of the aggregate.

The actual orientation distribution in a polycrystal is the result of the manufacturing route and thus texture can be interpreted to represent the detailed information about the production history of a specimen. Since texture has a strong influence on the properties exhibited by a polycrystal, it can be used to estimate the relationship between processing parameters and performance [15].

Textures in many materials develop during solidification from the melt where crystallites grow very fast along lattice direction aligned with the main direction of heat flow. The combined effect of deformation and recrystallization on the microstructure results in a complex combination of different physical processes that offers various possibilities with regards to the manipulation of texture.

The development of texture can have a great effect on the yield stress, ductility, and fracture toughness of a material. In polycrystalline materials any strain in one grain is often accommodated by strain in the adjacent grains which often results in lattice bending and fragmentation. This sometimes raises the local stresses sufficiently to initiate other high stress deformation systems not observed in single crystals. A simple way to develop texture in metals is by drawing, extruding and rolling. A preferred orientation can be detected by X-rays after about 20 to 30% reduction in cross-sectional area by cold-working. At this stage there will exist some considerable amount of scatter in the orientation of individual crystals about the ideal orientation. The scatter will continue to decrease until about 80 to 90% reduction, when the texture development is assumed to be complete [15].

Texture can be determined quantitatively by a number of techniques which commonly include x-ray diffraction and EBSD (Electron Back Scattered Diffraction) using SEM. Textures are normally represented by pole figures which illustrates the distribution of a pole of a crystallographic plane (conventional pole figure) or the distribution of all the planes in a particular specimen direction (inverse pole figure).

2.5. Simulation of neutron damage with ion irradiation

The Zr-2.5%Nb pressure tubes in a CANDU reactor undergo considerable microstructure deformation due to exposure to neutron irradiation during operation. Several studies have described how neutron irradiation induces the nucleation of point defects and small dislocation loops within such material [16-24]. These uniformly dispersed atom-sized crystal defects similar to Frenkel pairs and small dislocation loops of size in the order of tens of nanometer increase with increasing exposure to neutrons and are known to raise the yield stress of the irradiated material by impeding dislocation glide. Some characteristics of neutron irradiation damage in hcp metals, such as zirconium alloys, are that dislocation loops form as the result of the diffusion, accumulation, and collapse of irradiation induced vacancies on the close packed planes (i.e. the (0001) basal planes). The actual dislocation loop habit planes, the interstitial or vacancy nature of the loops, and the tendency for cavity formation due to the accumulation of irradiation induced vacancies can vary significantly depending upon material purity [25].

Neutron irradiated pressure tube materials are highly radioactive and have to be tested with remote manipulators in specially constructed cells containing sufficient radiation-shielding. This has restricted the amount of studies that has been carried out on these materials over the years. Scientists have therefore looked for alternative methods of inducing similar crystallographic defects to materials of interest in order to qualitatively study the mechanisms of neutron irradiation hardening and its effects. Several studies [25-30] have irradiated test samples with various types of charged particles such as heavy ions, protons, and electrons to induce crystallographic damage similar to that from neutron irradiation. The clear advantage of these techniques is that the test specimens do not become radioactive and hence can be tested upon in a conventional laboratory.

Heavy ion simulation of irradiation damage is one method of irradiating test materials and it involves bombarding the surface of a test sample with ions of the same element as the parent material being tested. In the case of Zr-2.5%Nb CANDU pressure tube, this can be accomplished by irradiating with samples cut out from the tube with high kinetic energy Zr^+ ions. Bose *et al* [29-30] carried out a study in which they irradiated samples cut out of the three orthogonal directions of the Zr-2.5%Nb pressure tube material and irradiated them with 8.5 MeV Zr^+ ions to investigate the effect of ion irradiation on the mechanical anisotropy and kinetics of plastic deformation of the material. With the help of the Monte Carlo simulations carried out using the SRIM software, they were able to estimate the interaction level of the Zr^+ ions with the Zr-2.5%Nb alloy. Polished surfaces of prepared samples with and without any Zr^+ irradiation were then subjected to constant force Berkovich indentation creep tests after which electron transparent foils of about 500 nm thickness were extracted by using focussed ion beam milling from within the resulting plastic zone of non irradiated and Zr^+ ion irradiated samples (Figs. 2.7-2.8). It can be inferred from these images that Zr^+ ion irradiation induces regions of mottled contrast that are usually found in uniform distribution of very small nanometer sized dislocation loops in the microstructure comparable to those that have been reported with neutron irradiation.

It was also observed from the results of indentations tests performed that Zr^+ ion irradiation reduced the anisotropy of the tube. The ratio of the average indentation stress

on the transverse normal (TN) plane relative to that on the axial normal (AN) and radial normal (RN) planes was 1.3 and 1.2 respectively before irradiation. After the samples were irradiated with Zr^{+} ions, the ratio of the *TN* plane relative to the *AN* and *RN* planes became 1.04 and 1.08 respectively [29].

The large kinetic energy of these heavy Zr^{+} ions are capable of inducing significant crystallographic damage that could extend to about 5 μm thick layer beneath the surface of the test material. While these methods can be very effective in simulating the microstructure alteration created by neutron irradiation, the challenge posed by this kind of analysis is that the damage created by these ions may not be exactly the same as those from neutron irradiation. Recent studies have however shown that these ions do create similar damages on the material like the formation of dislocation loops, increase in yield stress and altering of the strain conditions close to precipitates within the material [25-30].

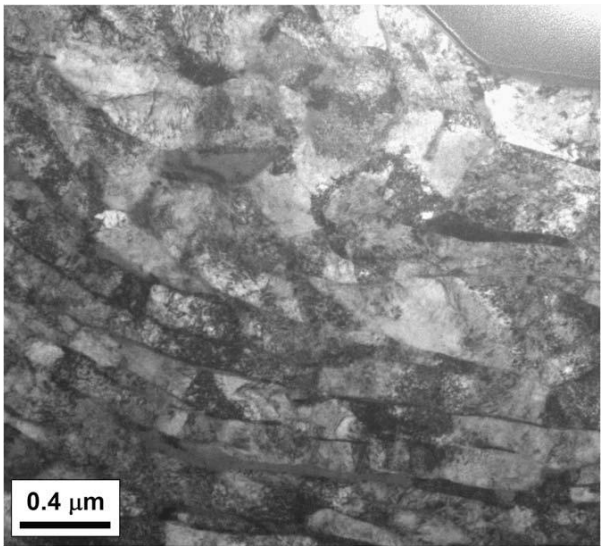

Figure 2.7. TEM image of the indentation plastic zone in the non-irradiated Zr-2.5%Nb sample. The dislocation distribution within the sample is inhomogeneous and attributed to the fabrication route [29].

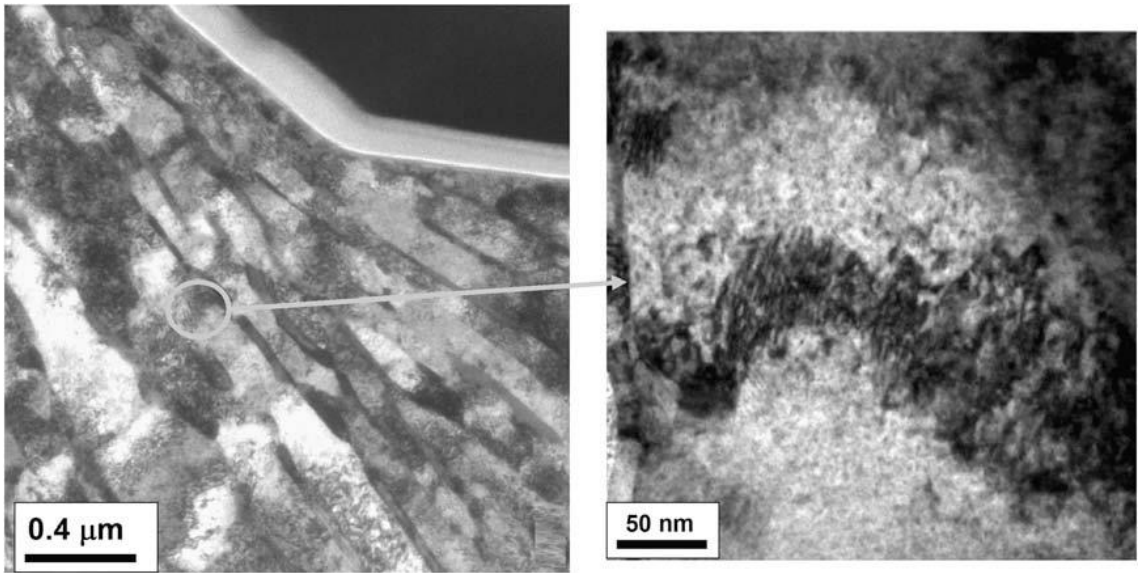

Figure 2.8. TEM image of the indentation plastic zone of a Zr^{+} irradiated Zr-2.5%Nb sample. The image on the right is a higher magnification of the inset on the left. It reveals regions of mottled "salt and pepper" contrast which were not observed in fig. 2.7 and can therefore be attributed to diffraction contrast resulting from the growth and uniform distribution of small dislocation loops due to Zr^{+} irradiation [29].

2.6. Instrumented indentation testing

The interest in, and the ability to perform, high-precision instrumented indentation testing has grown very rapidly over the last two decades. This can be associated, at least in part, with the increased interest in understanding the mechanical properties of very small volumes of materials such as, for example, thin deposited metal films. Indentation testing involves the use of a hard indenter, of conical, pyramidal, cube-corner, or spherical geometry, to press against the flat surface of the test material while continuously recording the indentation force and depth (Figure 2.9). The indentation depth resolution limits for such techniques now often exceed ± 10 nm and, thus, it is possible to measure local variations in the hardness, and thus the plastic flow stress, of materials with a spatial precision on the order of several atomic spacing.

Spherical indentation, while not having nearly the spatial resolution afforded by sharp-tip pyramidal or cube-corner indentation, provides the unique possibility for obtaining the

entire $\bar{\sigma}_{ind}$ - $\bar{\varepsilon}_{p_{ind}}$ response of the indented material from a single load cycle or multiple load cycle indentation test. This i**s** because**,** unlike the case for indentations made with geometrically self-similar shaped indenters[3], such as the conical, pyramidal and cube-corner indenters, the average equivalent plastic strain $\bar{\varepsilon}_{p_{ind}}$ beneath a spherical indenter increases with increasing indentation depth. The difference between geometrically self-similar indenters and spherical indenters is clearly illustrated in figure 2.10. In Fig. 2.10(a), an increase in the load on the indenter will not result in any change in the ratio of the length of the diagonal to the indentation depth (d_1/δ_1) but with a spherical indenter (Fig. 2.10(b)), an increase in the load P, will lead to a change in the ratio of the indentation radius to the indentation depth (a_1/δ_1) [31]. This property of spherical indenters has tremendous potential for assessing the mechanical properties of materials from which fabrication of full-size uniaxial tension test samples is impossible.

[3] An indenter shape is said to be geometrically self-similar if the ratio of the indentation width to depth remains constant regardless of indentation depth.

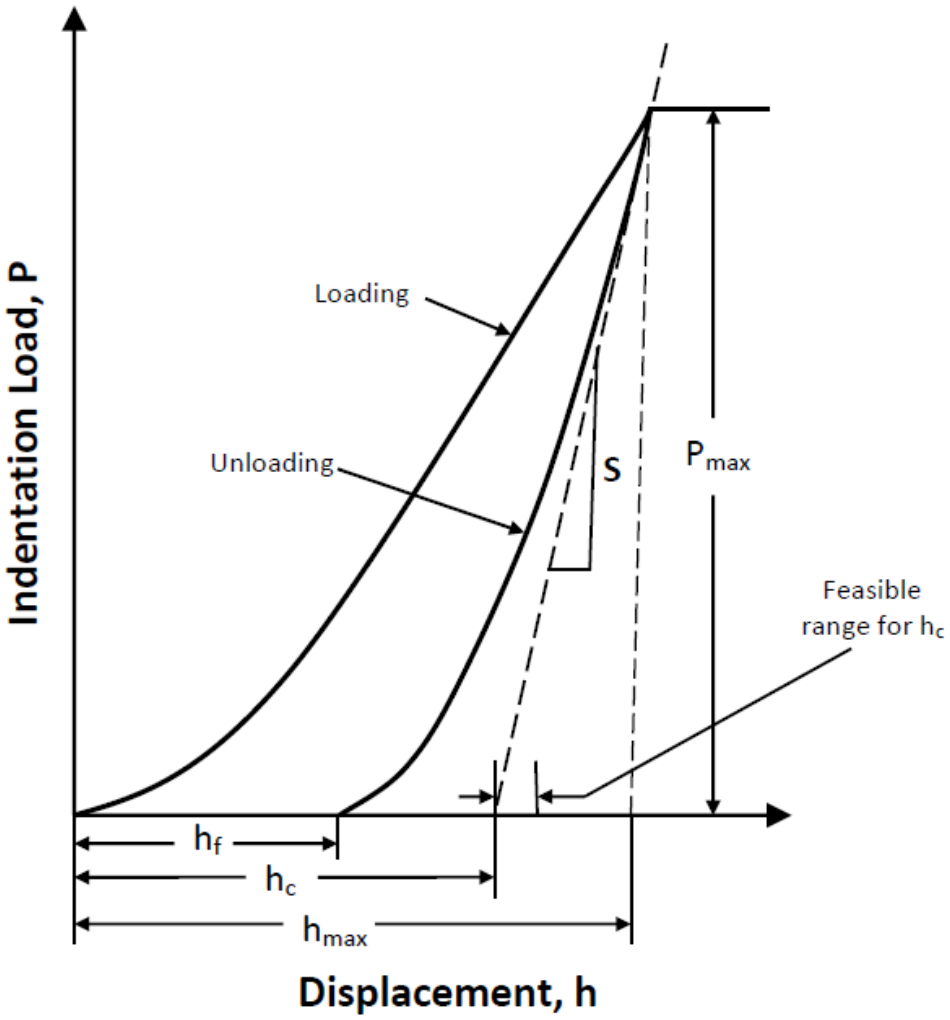

Figure 2.9. Schematic representation of an idealized indentation load versus indentation displacement (depth) curve resulting from an indentation test, where h_f is the plastic depth, h_c is the contact depth and h_{max} is the maximum depth attained by the indenter.

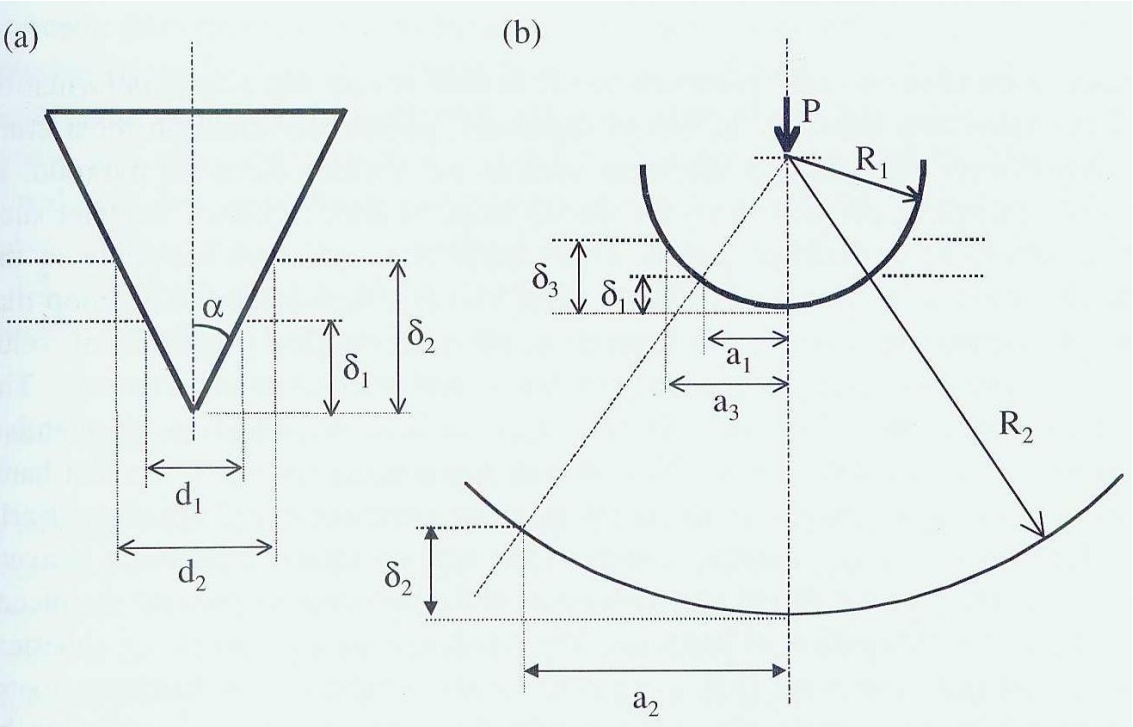

Figure 2.10. A schematic illustration describing the difference in the ratio of indentation width with indentation depth for (a) pyramidal / conical indenters and (b) spherical indenters [31].

2.6.1. Pile-up and sink-in phenomenon

During the elastic deformation of a material subjected to an indentation, it has been observed that the surface of the material will be elastically deformed inwards and downwards around the indenter which typically results in a slight sinking-in of the surface of the material underneath and around the indenter . When the elastic limit of the material is exceeded and plastic deformation begins, more material is displaced from underneath the indenter. This may sometimes lead to the upward displacement of material around the indenter in regions close and in contact with the surface of the material. In fig 2.11(a), an indenter load *P* is applied to the material surface causing the displaced portion of the material to flow between ‘ac’ and ‘bd’. This effect, which causes

an elevation of the material around the indenter is referred to as pile-up and occurs mostly in materials that are highly cold-worked, sometimes resulting in a substancial increase in the contact diameter of the indentation.

For materials that are annealed, the kind of deformation noticed is illustrated in figure 2.11(b). There is a depression noticed around the rim of the indentation referred to as ‘sinking-in’. However, at a little distance away from the depression, an elevated surface is observed which is as a result of an early displacement of material as the indenter was pushed into the material. This displaced material in the region ‘ab’ quickly becomes work-hardened and then begins to displace adjacent material that lies beneath it resulting in the displaced portion flowing out outside the perimeter ‘cd’. [31-32].

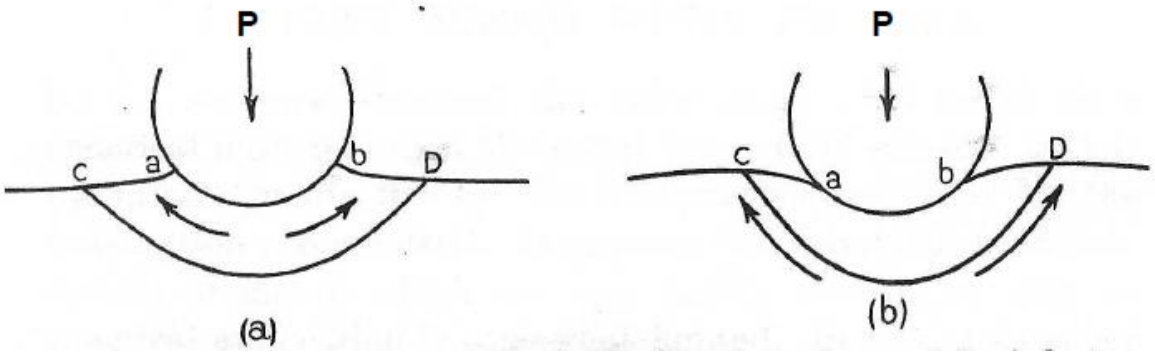

Figure 2.11. (a) An illustration showing the pile-up of material around the edges of the indenter in contact with the surface of the material for highly worked metals and (b) sink-in of the surface of the material in regions that are in contact with the indenter as a result of the material being in an annealed state [32].

2.6.2 Experimental evaluation of average strain resulting from spherical indentation

Figure 2.12 depicts the cross-section of a spherical indentation made in a ductile material. The spherical indenter, of radius *R*, creates an indentation of actual contact radius, a_c. The parameter h_c refers to the depth through which contact is made between the indenter and the material (contact depth of the indentation) while *h* is the maximum indentation depth. *P* is the applied indentation load, β is the angle of contact between the tangent to the indenter at the point of contact and the sample surface ($\tan\beta \approx h_c/a_c$), and c is the pile-up / sink-in factor.

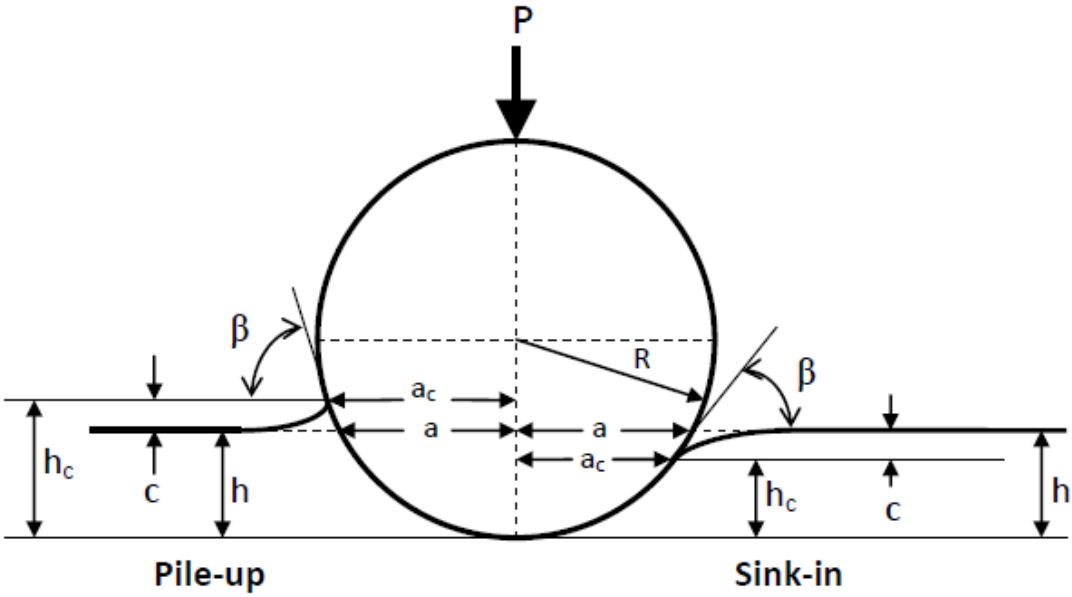

Figure 2.12. Cross section of an idealized spherical indentation showing the phenomena of pile-up and sink-of the test material around the indenter.

The plastic zone created beneath the spherical indenter clearly contains a non-uniform distribution of plastic strain the magnitude of which has been measured experimentally [32] for mechanically isotropic materials. Theoretical predictions and the experimental data suggest that the average indentation contact pressure P_m can be used to determine the equivalent flow stress $\bar{\sigma}$ of the indented material when subjected to a level of equivalent

plastic strain $\bar{\varepsilon}_p$ characteristic of the average equivalent plastic strain in the plastic zone of the spherical indentation. The relationship between P_m and $\bar{\sigma}$ can be expressed as:

$$P_m = \frac{P}{\pi a_c^2} = \psi \bar{\sigma} \tag{2.12}$$

In this equation ψ is the constraint factor, which reflects the complex triaxial stress state beneath the spherical indenter [33-36].

If the indentation of contact radius a_c is created with a spherical indenter of radius R, the average equivalent plastic strain $\bar{\varepsilon}_p$ within the indentation plastic zone will be a function of the ratio a_c/R as:

$$\bar{\varepsilon}_p = f\left(\frac{a_c}{R}\right) \tag{2.13}$$

The function $f\left(\frac{a_c}{R}\right)$ can be determined through experimentation by plotting P_m versus a_c/R from spherical indentation tests performed on the same material but with spheres of different radii. Figure 2.13 shows such a plot obtained from multiple spherical indentations made in annealed copper. The shape of the curve in Figure 2.9 is similar to that of the uniaxial σ - ε_p curve for annealed copper. This suggests that ψ is a direct function of $\bar{\sigma}$ and $f\left(\frac{a_c}{R}\right)$ is a linear function of a_c/R.

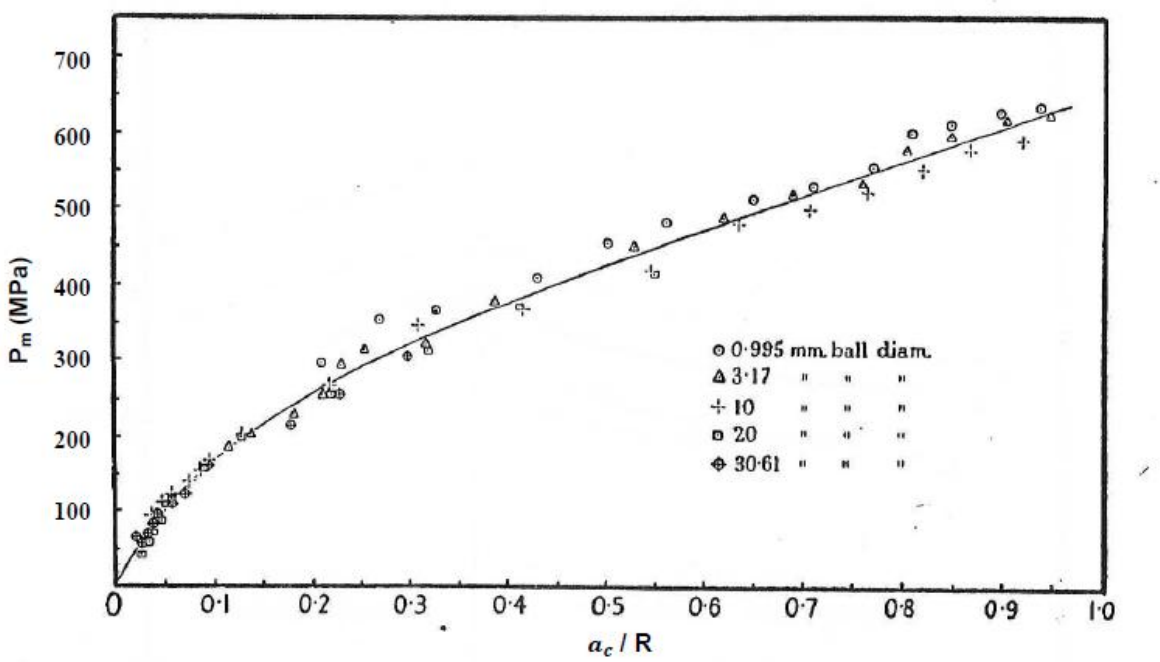

Figure 2.13. Plot of P_m versus a_c/R for annealed copper for different applied loads and different indenter diameters [32].

In an attempt to analyze the relationship between the mean contact pressure P_m and the yield stress σ_y during an indentation test, Tabor [32] used a pyramidal indenter with a large apex angle to determine the hardness around the impressed geometry of an indentation. Making use of an indenter with a large apex angle, guarantees that the hardness value will be relatively constant irrespective of the size of the applied load. Compression tests were first performed on blocks of mild steel and annealed copper and their Vickers hardness numbers were determined (Fig. 2.14). He then used the Vickers numbers to determine the corresponding strain values and the approximate yield stress of the metals.

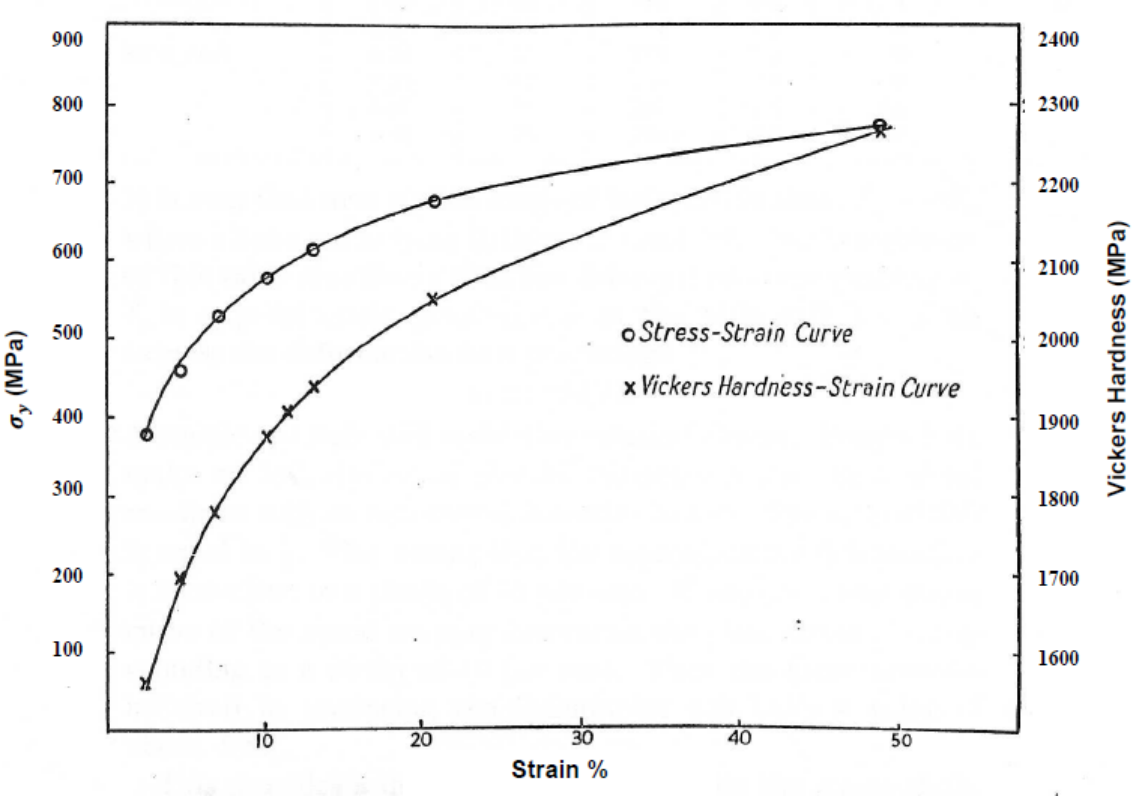

Figure 2.14. Yield stress values on the left axes and Vickers hardness values on the right axes plotted against the percentage strain for mild steel [32]

Spherical indentation tests were then performed on samples of mild steel and annealed copper after which Vickers hardness tests at small loads were used to determine the various levels of plastic strain within the permanent impression (Table 2.2) [32]. Tabor noted that over a wide range of indentation sizes, the constraint factor ψ has a value ranging from 2.6 and 2.8. He also observed that, by comparing the shape of the $\bar{\sigma} = P_m/\psi$ versus a_c/R with the $\bar{\sigma}$ versus $\bar{\varepsilon}_p$ curve obtained from the uniaxial tensile tests that

$$\bar{\varepsilon}_p = f\left(\frac{a_c}{R}\right) \approx 0.20\left(\frac{a_c}{R}\right) \tag{2.14}$$

Metal	Size of Impression (a_c/R)	σ_y (MPa)	P_m (MPa)	P_m/σ_y	% deformation corresponding to σ_y
Annealed Copper	0.27	102.9	264.6	2.6	5
	0.37	137.2	382.2	2.8	8
	0.5	156.8	431.2	2.8	9
Mild Steel	0.23	499.8	1293.6	2.6	6
	0.49	558.6	1558.2	2.8	9
	0.69	617.4	1577.8	2.6	15
	0.84	686	1862	2.7	20

Table 2.2. This table shows the values of P_m and σ_y obtained from tests performed on annealed copper and mild steel. These data were then used to estimate the value of the plastic strain during the spherical indentation test [32].

2.6.3. Evaluation of the average stress resulting from spherical indentation

Although the early experimental work provides very simple, and useful, approximations of $\bar{\sigma}$ and $\bar{\varepsilon}_p$ as a function of the measured P_m and a_c/R from a spherical indentation test, considerable effort has gone into simulating the local stress and plastic strain state around a spherical indentation such that $\bar{\sigma}$ can be determined more accurately from the high precision data afforded by modern instrumented indentation tests.

During an instrumented spherical indentation test the indentation force versus total indentation depth data are recorded. The actual contact depth h_c can be derived, using a method proposed by Oliver and Pharr [37], by considering the initial slope S of unloading

curve in the the force-depth plot (Fig. 2.9). From figure 2.9, one can express the total indentation depth h_{max} as:

$$h_{max} = h_c + h_s \tag{2.15}$$

where h_s is the elastic displacement of the material surface from its original position as a result of the application of the indentation load. The indentation contact radius a_c is a function of h_c and h_c can be calculated from the measured h_{max} when h_s is known. An analysis of the elastic surface displacement resulting from indentations performed with a variety of indenter shapes was reported by Sneddon [38] who demonstrated that h_s could be expressed in terms of the contact stiffness S (the initial slope of the unloading indentation force – depth curve, Figure 2.9) of the indented material as

$$h_s = \alpha \frac{P_{max}}{S} \tag{2.16}$$

where the geometric constant α is given as 0.75 for spherical indenters. With the value of h_c determined, the actual contact radius a_c can then be expressed as [39]:

$$a_c = \left(c(2Rh_c - h_c^2)\right)^{1/2} \tag{2.17}$$

where R is the radius of the indenter and c is the pile-up parameter. Following the derivation by Hill *et al*. [13, 40], the pile–up parameter c around the spherical indenter can be estimated as:

$$c = \frac{5}{2}\left(\frac{2-n}{4+n}\right) \tag{2.18}$$

where n is the work hardening exponent of the material.

For anisotropic materials, the values of contact radius a_c for each indentation may not be constant since the degree of metal pile-up or sink-in around the indentation may vary due to directional variation in the yield stress and work hardening exponent of the sample [41-43].

The average indentation stress $\bar{\sigma}$ is calculated from the mean contact pressure P_m as described in Eq. 2.12. Johnson [33] suggested that there are three distinct deformation stages occurring during a spherical indentation process. He referred to them as the elastic, elastic-plastic and fully plastic regimes and determined from experimental data that the constraint factor ψ followed a different functional dependence upon a_c/R in each region. In the case of very deep indentations where the general plastic strain far exceeds the elastic strain, the plastic zone is considered to be "fully plastic" and ψ becomes constant (in agreement with the previously mentioned experimental findings of Tabor), however for smaller indentations, where elastic deformation represents a significant component of the deformation, ψ is not constant and is in fact a function of a_c/R and the ratio of the modified elastic modulus to the yield stress (E^*/σ_y) of the indented material as will be shown.

Francis [35], after an analysis of a large amount of available published data on spherical indentation including those by Johnson and Tabor, reported that the fundamental independent geometric variable for the deformation process was the ratio h_c/a_c (This is also in agreement with the earlier work by Johnson). He then correlated the influence of the material parameter (σ_y/E^*), which he defined as a measure of elastic strain capacity, to a non-dimensional function ϕ as

$$\phi = \frac{E^*}{\sigma_y}\frac{h_c}{a_c} \tag{2.19}$$

where σ_y is the uniaxial yield stress of the material and E^* is the modified Young's modulus expressed as:

$$E^* = \frac{E}{(1-\upsilon^2)} \tag{2.20}$$

In Eq. 2.20, E is the Young's modulus and υ is the Poisson's ratio of the indented material.

Johnson demonstrated that the constraint factor ψ is a function of the single non-dimensional function ϕ and that in the case of a two-dimensional plane-strain indentation, ϕ has a value less than 2 during purely elastic deformation. However, when the value of ϕ becomes greater than 100, the regime is said to be fully plastic and the constraint factor ψ will have an average value of 2.87 (identical to that reported by Tabor (Table 2.2). When the value of ϕ is between 2 and 100, the deformation is considered to be in the elastic-plastic regime and the value of ψ can be predicted by the non-linear relationship expressed as

$$\psi = 1.1 + 0.017468\phi \tag{2.21}$$

Equation 2.21 was derived from a linear fit to the plot of P_m/σ_y versus $ln\phi$ (Fig. 32, Ref [33]).

The end result of these analysis is that one can perform spherical indentation tests with an instrumented indenter and obtain indentation force *P* versus indentation depth *h* data and, provided the tests involve partial un-loadings such that the indentation stiffness *S* can be obtained, the equivalent $\bar{\sigma}_{ind}$ - $\bar{\varepsilon}_{p_{ind}}$ response of the indented material can be obtained. This method of analysis requires that the initial yield stress σ_{yield}, and the strain-hardening exponent *n* of the material be known.

2.7. Haggag's field indentation microprobe

The theory and procedure of using spherical indentation to evaluate, by a non-destructive testing process, the mechanical properties of metals has been around for some time. Notably amongst them is the field indentation microprobe (FIM) apparatus that was designed, developed and patented by Haggag [44]. In it, he described how an automated ball indentation testing system could be used to measure the flow properties and to estimate the fracture toughness in metallic materials.

The FIM apparatus is an automated technology that measures the mechanical properties of test samples by performing a ball (spherical) indentation and acquiring the Force-Depth data over a reasonable indentation depth. Figure 2.15 illustrates the apparatus of

this equipment that can be mounted on any test equipment by a number of different methods. One of such involves the use of a tripod mechanism that can attach itself to the sample with the help of magnets or clamps. Once the mounting has been done in such a manner that the ball indenter is perpendicular to the surface of the sample, the load can then be applied by hydraulic, pneumatic, or mechanical means. FIM is made up of two main units that include an automated ball indentation (ABI) unit used to evaluate the integrity of metals and a nondestructive evaluation (NDE) unit that consists of ultrasonic transducers and a video camera for analyzing properties like crack size, material pile-up around indentations and to determine the presence of residual stresses.

Most of its operations are automated to reduce testing time like the motion of the X-Y testing head for positioning the indenter in the proper test location and the motion of the ultrasonic transducers attached to the testing head for scanning the surface of the sample. Other automated operations include the cyclic loading and partial unloading of the ball indenter during indentation at a pre-specified strain rate and the acquisition and analysis of test data.

The test procedure involves multiple indentation test cycles at same location using a ball indenter of either a 760 or 1,590 μm diameter to indent the material to a pre-determined maximum load or maximum depth. The F-h data from each unloading sequence is then fitted with a straight line equation to obtain a linear fit which is then extrapolated to zero-load to obtain the corresponding displacement. The maximum cycle load at each displacement is used to determine the yield strength and other mechanical properties [44-45].

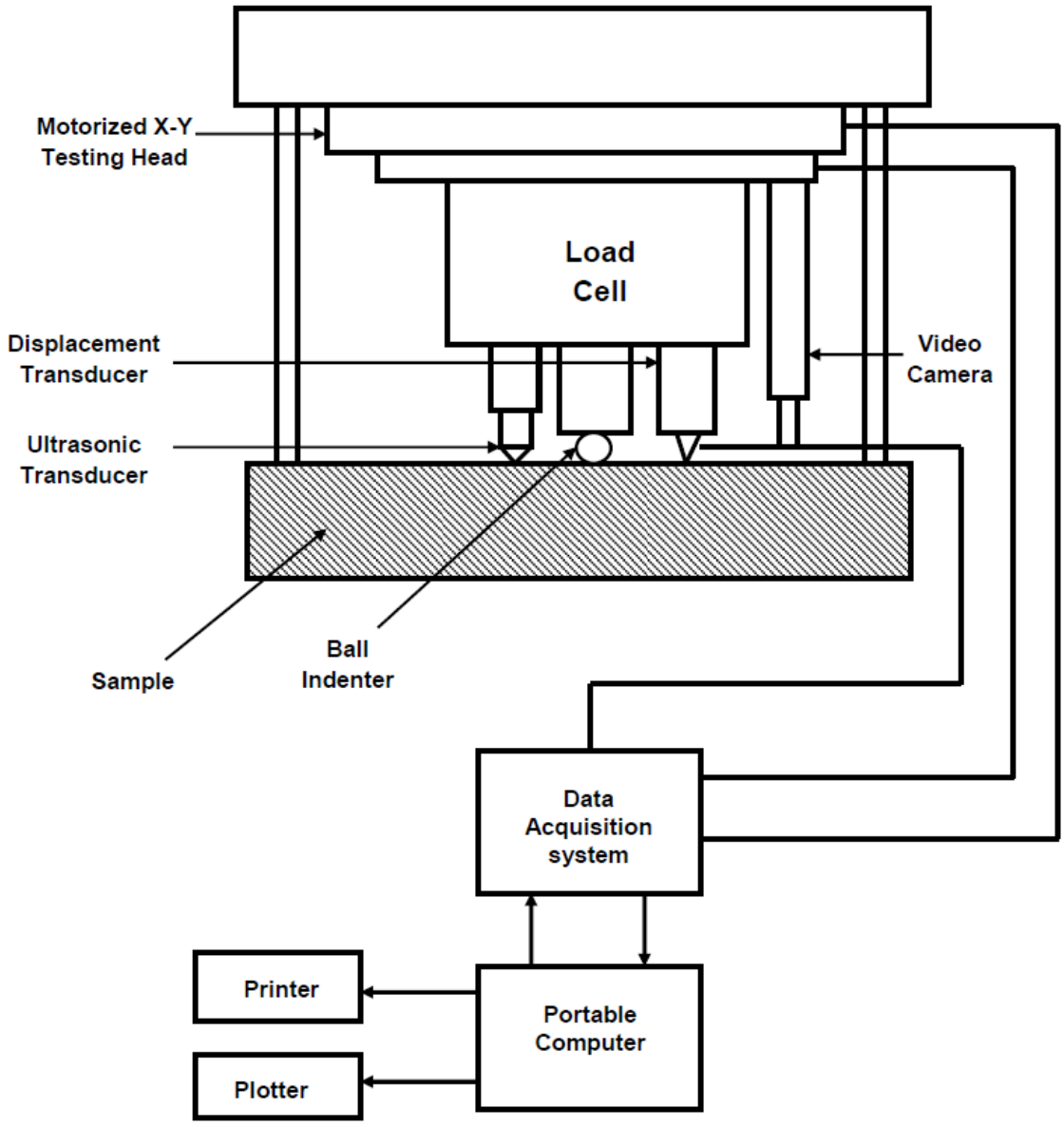

Figure 2.15. A schematic illustration showing the basic components of a field indentation microprobe (FIM) apparatus [45].

2.8. Applications of spherical microindentation

In 1900, Johan Brinell introduced the Brinell hardness test in which a hard spherical indenter was pressed onto the polished surface of a specimen with a fixed normal load until equilibrium was attained. After the load and indenter were removed, the Brinell Hardness Number (BHN) was calculated as the ratio of the maximum applied load to the curved area of the indentation. Since then, several researchers have modified Brinell's original technique to suit varying applications.

Weiler [46] used spherical indentation tests to study the effect of grain size on the mechanical properties of die-cast magnesium AM60B alloy. Since the grain size was a function of the cooling rate, there will always be a variation in the grain sizes throughout the microstructure. Grains near the surface tend to cool at a faster rate that those within the core of the casting especially in complex die-castings where the cross-section may vary with thickness. Several samples were cut from the skin region (areas of the alloy with finer grain sizes) and the core region (areas with larger grain sizes and dendrites). Spherical micro-indentation tests were then performed on these samples and the force-displacement curve obtained was used to determine the plastic flow stress properties of the samples.

Another example where spherical micro-indentation testing may be useful is in the characterization of the mechanical anisotropy of Zr-2.5%Nb pressure tubes (both in the non-irradiated and the neutron irradiated conditions). Since these pressure tubes are only about 4 mm thick, it is practically impossible to construct conventional uniaxial tensile samples to assess the yield stress in the radial direction of the tubes. Without these data a complete assessment of the degree of anisotropy of the $\sigma - \varepsilon_{plastic}$ response cannot be known since it is impossible to obtain sufficient data from which to deduce the anisotropy factors *F*, *G*, and *H* (Equations 2.10). Spherical indentation is also potentially useful for assessing the $\bar{\sigma}_{ind} - \bar{\varepsilon}_{p_{ind}}$ response of radioactive Zr-2.5%Nb pressure tube material since performance instrumented spherical micro-indentation tests could be performed remotely in a radiation-shield cell. What follows is a description of the current state of knowledge on the theory involved in determining the $\bar{\sigma}_{ind} - \bar{\varepsilon}_{p_{ind}}$ response of a ductile material from

the indentation load - depth data obtained from a spherical indentation test. This work is presented in Chapters 4 of this thesis.

2.9. Testing equipments

During the investigations carried out in this thesis, several sample preparation, testing and analysis equipments were used to achieve our research objectives and what follows is a concise description of some of the important equipments, their operation and uses.

2.9.1. The NanoTest indentation platform

The spherical indentation tests and micro-pillar compression tests carried out in this study were performed on a NanoTest indentation machine which is a nano/micro-mechanical property testing platform designed and manufactured by Micro Materials Ltd. Wrexham, United Kingdom [47]. The machine consists of three separate modules that include: indentation, scanning and impact testing. All three modules are designed to work in conjunction with the low load head (0.1-500 mN) or the high load head (0.1-20 N).

As shown in the illustration in fig. 2.16, the NanoTest platform is made up of a pendulum that has the freedom to rotate on a friction-less pivot. At the bottom end of the pendulum is attached the probe (indenter) and at the top end is mounted a copper coil that is attracted to a permanent magnet once a coil current is introduced. This attraction of the coil causes a movement of the probe towards the sample and the distance moved is proportional to the magnitude of the current in the coil. The resulting displacement of the probe is measured by a parallel plate aluminum capacitor that has one of the plates attached to the probe holder. Any change in the distance between the capacitor plates as a result of the movement of the probe, translates into a change in the capacitance which is measured by a capacitance bridge located in close proximity to the measuring capacitor to reduce the effects of stray capacitance.

The sample to be tested is attached to a stage whose motion can be manipulated by means of three DC motors in an X-Y-Z configuration. These DC motors are controlled from a motherboard that has three power modules, an electronic interface module and a backlash control unit. Power supply to the system is from the computer while magnetic encoders

control the motor positioning. When current is applied to the coil, the probe's maximum movement and pendulum orientation are determined by the limit stop setting.

The machine works by measuring the motion of a probe (indenter) when in contact with a material surface. The sequence begins by applying an increasing amount of force on the probe to either indent or compress the surface of a polished sample or feature to a predetermined force/depth at a defined loading rate. The force, depth and time of the test are recorded by the NanoTest software installed on the computer system to collate and process the data and determine the mechanical properties of the material. The shape of the unloading curve is determined by the elastic and plastic properties of the sample and the slope of the initial unloading data extrapolated to zero force on a force-displacement plot, referred to as the stiffness of the contact is an important parameter used to calculate the reduced modulus and depth through which contact is made between the probe and sample. The geometry of the probe used to carry out the test sometimes determines the kind of properties that can be extracted from the data collected from indentation tests.

For high temperature testing, a high temperature testing probe is used along with independently controlled heating stages to ensure that both the probe and the sample are at the same temperature. Both heaters are controlled by separate temperature controllers. The probe is attached to an aluminum shield and the surrounding area around the probe and sample are covered with insulating material to minimize any heat loss to the environment.

To run a test schedule, it is sometimes necessary to perform a number of test calibrations of which the two most important are the load and depth calibrations to ensure that the platform is running optimally to be guaranteed output data that is accurate. Load calibrations are performed by hanging three weights whose mass are known to the pendulum while the machine records the voltage required to the actuator coil to balance the pendulum in a vertical position. Depth calibration on the other hand is performed using a sample of known material properties (fused silica). No force is applied to the indenter during this test, rather the DC motor is used to move the stage with the sample attached to make contact with the indenter until the signal coming from the aluminum

capacitor plates is a quarter of the initial value. The movement of the motor the reverses while the change in signal amplitude is continually monitored against the displacement of the calibration sample. A good calibration range for the Nano-Test head will yield a result of about 0.05-0.06 nm/bit while the micro-test head will have a value of about 0.2-0.3 nm/bit.

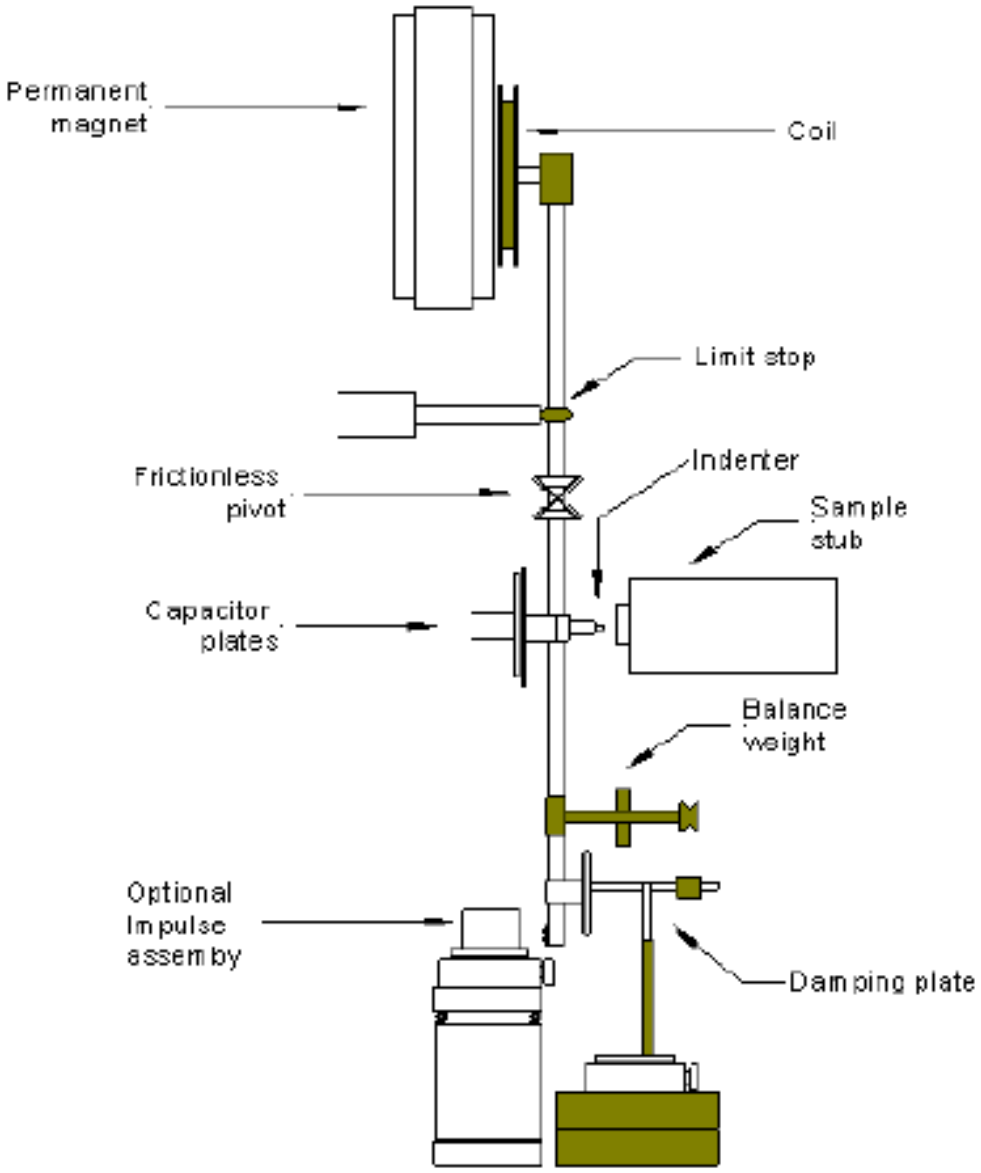

Figure 2.16. Schematic description of the hardware components of a NanoTest platform [47].

2.9.2. The focussed ion beam instrument (FIB)

The focused ion beam (FIB) instrument is very similar to the scanning electron microscope (SEM). While FIB instruments can be stand-alone equipments, the one used in our investigations, LEO (Zeiss) 1540XB FIB/SEM, was incorporated with an SEM to form a dual platform system with enhanced capabilities. The FIB ion column is mounted at an angle of 54° to the sample stage in a horizontal position. This system is fitted with a sample transfer airlock compartment that allows for rapid sample change without causing significant disruption to the high vacuum of the main chamber. It is also fitted with a six-axis sample stage that allows for complex sample manipulation. Other major components include liquid metal ion source, an ion column, an electron column, detectors gas inlets and a computer system used to control and operate the instrument.

Figure 2.17 shows the schematic of a basic FIB instrument without the electron column. Micromachining is carried out by sputter milling that basically involves sputtering of atoms from the surface of the material. For milling purposes, a liquid metal ion source (LMIS) is needed. Ga^{+} ions are commonly used for this purpose because of its low melting point at 29.8 °C which reduces the reaction between the ion and tungsten needle substrates. Other reasons include low volatility, low surface free energy, low vapor pressure and excellent mechanical, electrical and vacuum properties and finally it possesses high angular intensity with a small energy spread. The advantage of having an electron column is that the milling process can be monitored real-time at high resolution [48].

For very complex micromachining operations, this instrument is equipped with a nanometer pattern generation system (NPGS) which is a lithographic system designed to provide a flexible environment for delineation of complex structures. The pattern is generated using a pattern design after which a run-file is created and finally a pattern writing with an optional alignment for multilevel lithography.

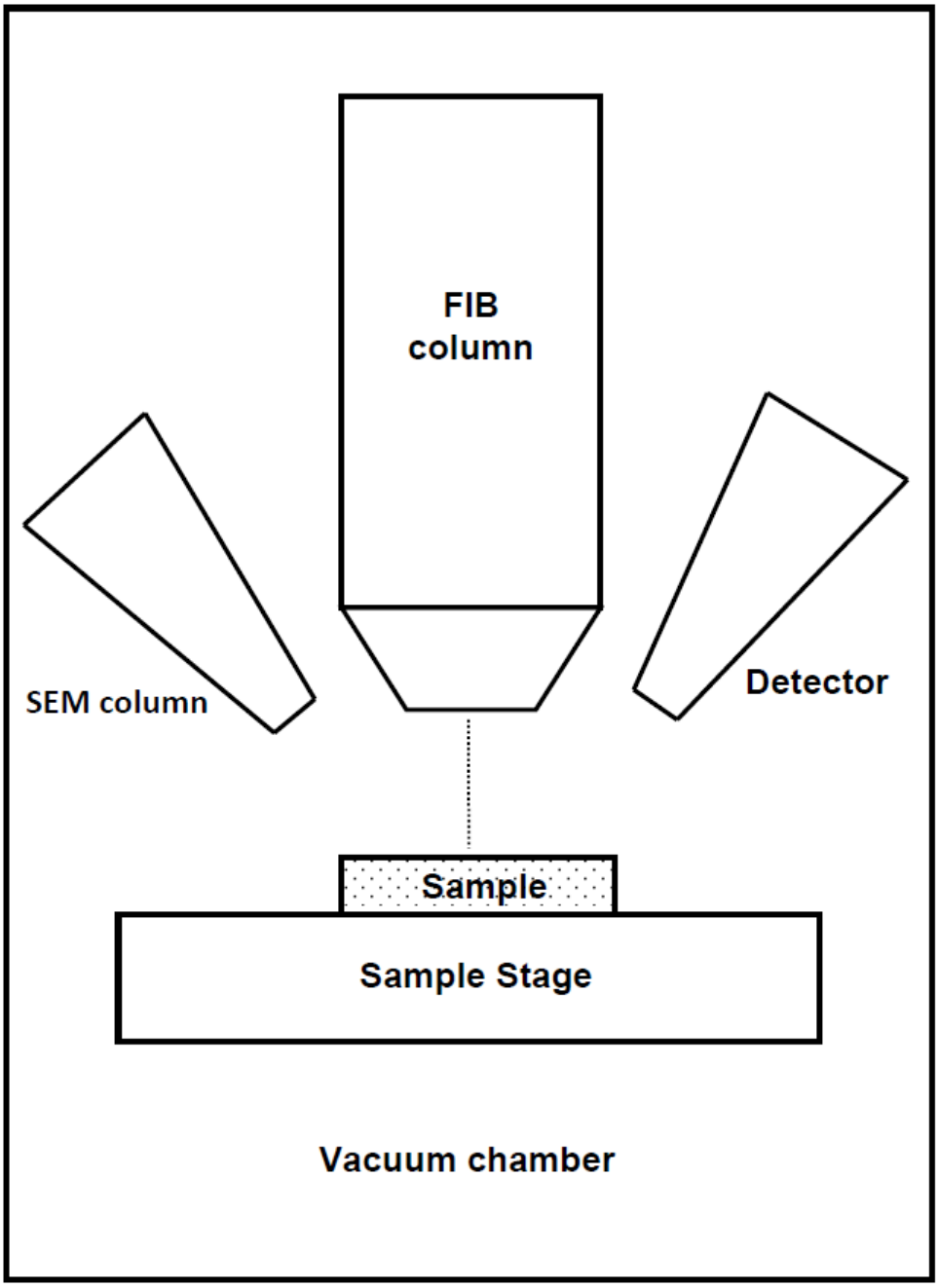

Figure 2.17. A schematic diagram of a basic FIB system showing the major components [48].

2.9.3. The 1.7 MV Tandetron ion accelerator

The 1.7MV Tandetron ion accelerator is a sophisticated system designed to generate ion beams of almost every element in the periodic table for the purpose of altering the properties of materials for simulation and other analysis. It is equipped with a built in magnetic suppression system that minimizes the effects of backstreaming electron energy gain thereby preventing any disruptions from X-ray radiation during operation [49-50].

Figure 2.18 shows a schematic of the Tandetron ion accelerator used in our investigation assembled by High Voltage Engineering Europa, Netherlands. Unlike ion accelerators that have their power supply from a current source, this one gets its power from a voltage source, which eliminates the need for corona stabilization to eliminate differences in beam and charging currents. Also, since its power supply is solely electronic, there are no moving parts within the unit that create unwanted vibrations that may give rise to terminal voltage fluctuations and ripples within the system.

It is equipped with two ion sources, the duoplasmatron source and the sputter source. The duoplasmatron source is specially suited for producing light ions like hydrogen and helium ions, while the sputter ion source used in this study can produce ions from a very wide variety of materials. The base material employed was Zirconium hydride from which negative zirconium ions were generated and passed through a stripper canal to convert them to positive zirconium ions. Low energy magnets are then used to attracts the Zr^{+} ions towards the accelerator tube where specially designed lenses are used to match the characteristics of the injected beams with the ion optics of the accelerator before making use of the electromagnetic field within the unit to propel the ions towards the accelerator terminal while ensuring that there is no significant change to their beam diameter. On exiting the accelerator, the ion beams are attracted towards the implantation chamber by high energy magnets where they are used for implantation or for carrying out other material surface property transformation. An image of the implantation chamber is shown in Fig. 2.19.

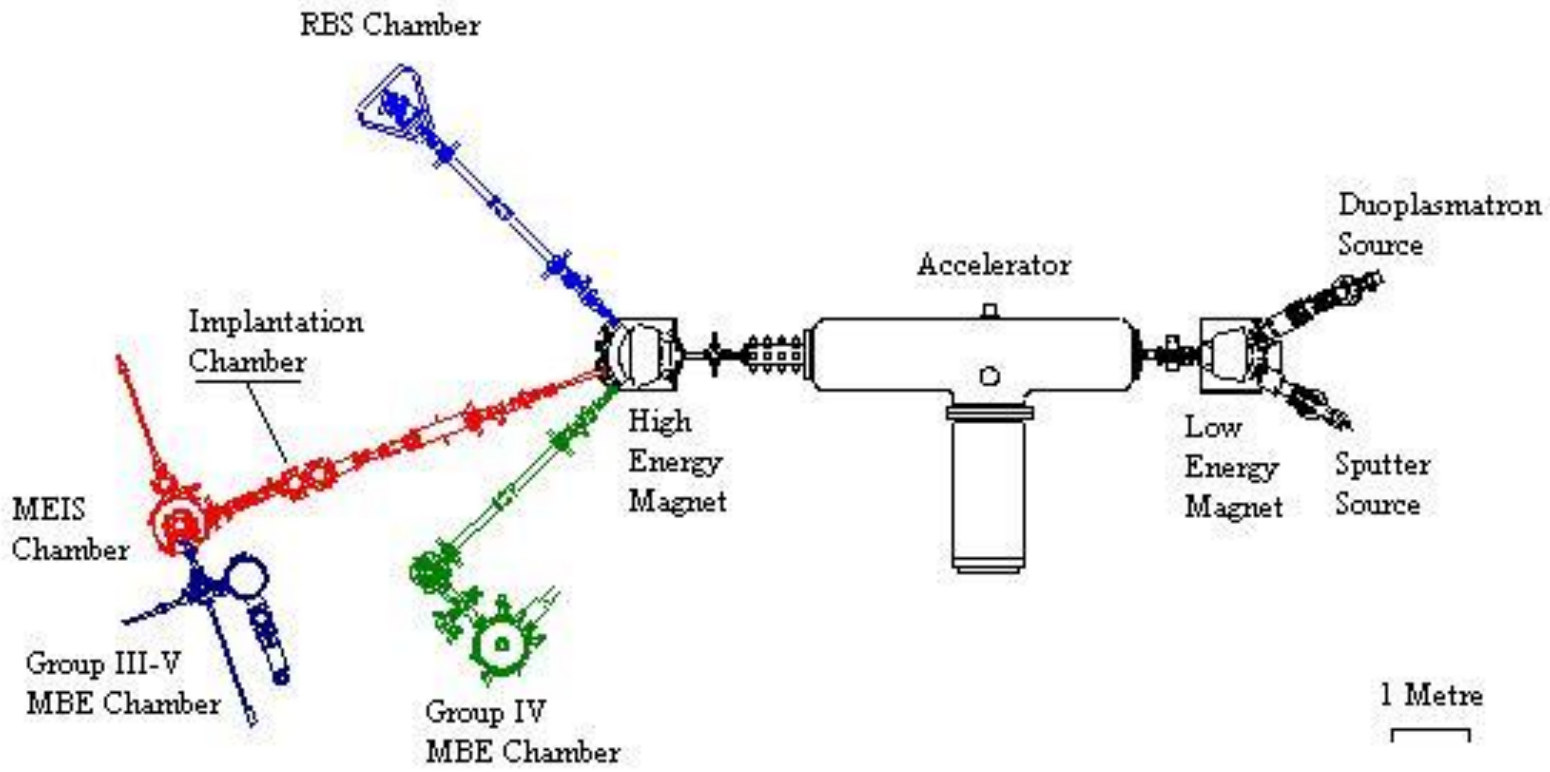

Figure 2.18 Schematic illustration of the tandetron ion accelerator showing the major components of the equipment [49]. An enlarged image of the implantation chamber is shown in Fig. 2.19.

This equipment has the capability to carry out implantation of surfaces with diameters of up to 50 mm at temperatures ranging from -195 to 600°C. The samples to be implanted are usually mounted on a nickel block that can be heated or cooled to temperature within the range specified and the temperature can be monitored using three different thermocouples embedded within the nickel block.

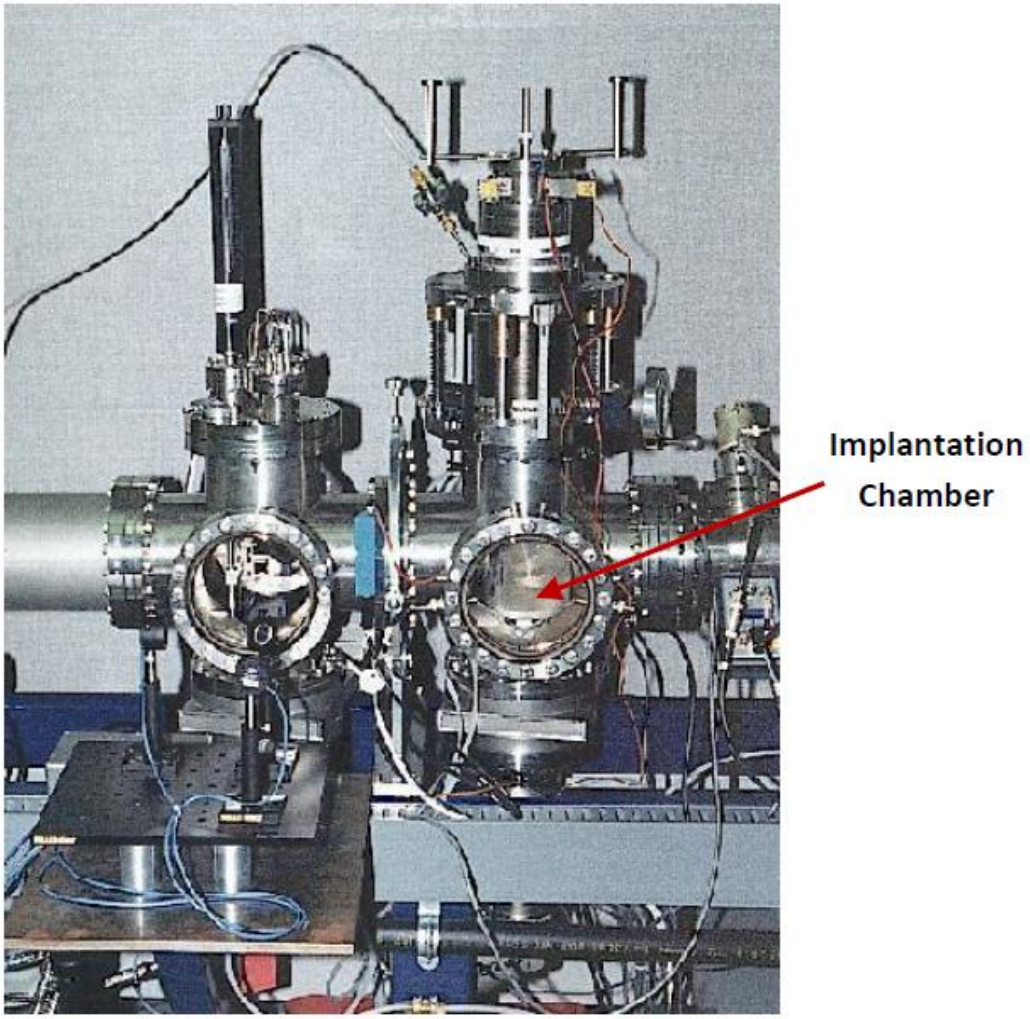

Figure 2.19. An image of the implantation chamber of the 1.7 MV tandetron ion accelerator at the Interface Science Research Center [49].

2.10. Summary

This chapter has introduced the fundamental concepts that apply to the research described in the subsequent chapters of this thesis which is tailored towards exploring new methods for testing irradiated pressure tubes from nuclear reactors. The techniques described will be used to assess the effect of temperature and irradiation hardening on the mechanical anisotropy of extruded and cold-drawn Zr-2.5%Nb CANDU pressure tube material. The three investigations carried out here include the following:

- The use of uniaxial macro-pillar compression tests to investigate the mechanical anisotropy of non-irradiated Zr-2.5Nb alloys at temperatures ranging from 25 to 300 °C. This research is presented in Chapter 3.
- An assessment of the usefulness of spherical micro-indentation to deduce the equivalent stress – plastic strain response of anisotropic Zr-2.5%Nb at temperatures ranging from 25 to 300 °C. This research is presented in Chapter 4.
- The use of uniaxial compression of small-diameter micro-pillars to investigate the effect of Zr+ ion irradiation on the mechanical anisotropy of Zr-2.5% Nb samples. This research is presented in Chapter 5.

References

[1] P. Mani Mathew, T. Nitheanandan, S.J. Bushby, Severe Core Damage Accident Progression within a CANDU 6 Calandria Vessel, (AECL).

[2] Assessment and Management of Aging Major Nuclear Power Plant Components important to safety, IATA-TECDOC-1037 (1998).

[3] J.R. Lamarsh, A.J. Baratta, Introduction to Nuclear Engineering, Prentice Hall, 2001.

[4] N. Christodoulou, P.A. Turner, C.N. Tomé, C.K. Chow, R.J. Klassen, Metallurgical and Materials Transactions A, 33A (2002), p. 1103.

[5] B. Lustman, F. Kerze Jr, The Metallurgy of Zirconium, McGraw-Hill (1955) p. 466.

[6] B.A. Cheadle, C.E. Ells, W. Evans, J. Nucl. Mater. 23 (1967) 199.

[7] B. A. Cheadle, S.A. Aldridge, C.E. Ells, Can. Metall. Quart. 11 (1972) 121.

[8] R.A. Holt, P. Zhao, J. Nucl. Mater. 335 (2004) 520.

[9] W.K. Alexander, V. Fidleris, R.A. Holt in: Proceedings of 3rd International symposium on Zirconium in the Nuclear Industry, ASTM STP 633, 1977, p. 344.

[10] J.J. Kearns, Report No. WAPD-TM-472, Westinghouse Co., Pittsburgh PA, 1965.

[11] N. Christodoulou, A.R. Causey, R.A. Holt, C.N. Tome, N. Badie, R.J. Klassen, R. Sauve, C.H. Woo, in: Proceedings of the 11th International Symposium on Zirconium in the Nuclear Industry, ASTM STP 1295, 1996, p. 518.

[12] G.E. Dieter, Mechanical Metallurgy, McGraw-Hill Book Company, 1988.

[13] R. Hill, The Mathematical Theory of Plasticity, Oxford at the Clarendon Press, 1971.

[14] W.F. Hosford, The Mechanics of Crystals and Textured Polycrystals, Oxford Science Publications, 1993.

[15] U.F. Kocks, C.N. Tome, H.R. Wenk, Texture and Anisotropy, Cambridge University Press, 2000.

[16] R.A. Holt, A.R. Causey, M. Griffiths, E.T.C. Ho, in: Proceedings of the 12th International Symposium on Zirconium in the Nuclear Industry, ASTM STP 1354, 2000, p. 86.

[17] R.A. Holt, J. Nucl. Mater. 372 (2008) 182.

[18] N. Badie, R.A. Holt, C.W. Schulte, R.G. Sauve, in: Proceedings of the Ninth Annual Conference of the Canadian Nuclear Society, June 1988.

[19] R.A. Holt, A.R. Causey, V. Fidleris, Proceedings of the International Conference on Dimensional Stability of Irradiated Metals and Alloys, vol. 1, British Nuclear Energy Society, 1983, p. 175.

[20] R.A. Holt, N. Christodoulou, A.R. Causey, J. Nucl. Mater. 317 (2003) 256.

[21] R.A. Holt, E.F. Ibrahim, Acta Metall. 27 (1979) 1319.

[22] E.F. Ibrahim, R.A. Holt, J. Nucl. Mater. 91 (1980) 311.

[23] V. Fidleris, J. Nucl. Mater. 159 (1988) 22.

[24] A.R. Causey, R.A. Holt, S.R. MacEwen, in: Proceedings of the Eighth International Symposium on Zirconium in the Nuclear Industry, ASTM-STP 824, 1984, p. 269.

[25] M. Griffiths, J. Nucl. Mater, 205 (1993) 225.

[26] R.O. Oviasuyi. R.J. Klassen, J. Nucl. Mater. 421 (2012) 54-57.

[27] C.K. Chow, R.A. Holt, C.H. Woo, C.B. So, J. Nucl> Mater. 328 (2004) 1.

[28] C.D. Cann, C.B. So, R.C. Styles, C.E. Coleman, J. Nucl. Mater, 205 (1993) 267.

[29] B. Bose, R.J. Klassen, J. Nucl. Mater. 399 (2010) 32.

[30] B. Bose, R.J. Klassen, J. Nucl. Mater, 405 (2010) 138.

[31] A.C. Fischer-Cripps, Nanoindentation, 2002.

[32] D. Tabor, The Hardness of Metals, Oxford Press, 1951.

[33] K.L. Johnson, J. Mech. Phys. Solids, 18 (1970) 115.

[34] S.D. Mesarovic, A. Fleck, Proc. R. Soc. Lond. A 455 (1999) 2707.

[35] H. A. Francis, J. Eng. Mater. Tech. Trans. ASME (1976) 272.

[36] M. Beghini, L. Bertini, V. Fontanari, Intern. J. Comp. Appl. Tech. 15 (2002) 168.

[37] W.C. Oliver, G.M.Pharr, J. Mater. Res. 7 (1992) 1564.

[38] I.N. Sneddon, Int. J. Eng. Sci. 3 (1965) 47.

[39] J-H. Ahn, D. Kwon, J. Mater. Res., 16 (2001) 3170.

[40] B. Taljat, G.M. Pharr, Int. Jour. Sol. Struc. 41 (2004) 3891.

[41] M. Bocciarelli, G. Bolzon, G. Maier, Mech. Mater. 37 (2005) 855.

[42] T. Nakamura, Y. Gu, Mech Mater. 39 (2007) 340.

[43] A. Yonezu, K. Yoneda, H. Hirakata, M. Sakihara, K. Minoshima, Mater. Sc. & Eng. A 527 (2010) 7646.

5999.

[44] F.M. Haggag, U.S. Pataent #4852397 (1990)

[45] F.M. Haggag, R.K. Nanstad, J.T. Hutton, D.L. Thomas, R.L. Swain, Applications of Automation Technology to Fatigue and Fracture Testing, ASTM 1092 (1990) 188.

[46] J.P. Weiler, J.T. Wood, R.J. Klassen, R. Berkmortel, G. Wang, J. Mater. Sc. 40 (2005)

[47] B. Beake, S. Goodes, S. Jones, R. Parkinson, N. Pickford, J. Smith, NanoTest Help File, Micro Materials Ltd, 2004.

[48] F.A. Stevie, L.A. Giannuzzi, Introduction to Focussed Ion Beam, Springer, 2005.

[49] Interface Science Western Research (www.uwo.ca/isw)

[50] Tandetron Accelerator Systems (www.highvolteng.com/media/brochures)

Chapter 3

3. Assessment of the anisotropic flow stress and plastic strain of Zr-2.5%Nb pressure tubes at temperature from 25°C to 300°C[4]

In this chapter uniaxial compression testing is used to assess the stress versus plastic strain response in the axial, radial and transverse directions of the mechanically anisotropic Zr-2.5%Nb CANDU pressure tube material over the temperature range from 25 to 300°C. The data from these tests are used to determine the Hill's anisotropy coefficients $F = 0.38 \pm 0.01$, $G = 0.202 \pm 0.001$, and $H = 0.62 \pm 0.01$ of the pressure tube material. These coefficients were found to be independent of temperature and plastic strain. The anisotropy coefficients were applied to calculate the equivalent stress versus equivalent plastic strain corresponding to stress – plastic strain data for Zr-2.5%Nb pressure tube material obtained from a variety of sources including from this study. In all cases the stress – plastic strain data fell upon a single equivalent stress versus equivalent plastic strain curve when the anisotropy coefficients *F*, *G*, and *H* obtained from this study were used to calculate the equivalent stress and plastic strain.

The results of this study represent the only experimentation-based determination of the Hill's anisotropy coefficients *F*, *G*, and *H* of extruded and cold-drawn Zr-2.5%Nb CANDU pressure tubes over a wide temperature range extending up to the 300°C in-service temperature of these pressure tubes.

3.1. Introduction

Extruded and cold-drawn Zr-2.5%Nb tubes are used to transport pressurized heavy water coolant, at temperature from 250°C to about 310°C, through the core of CANDU nuclear reactors. The mechanical properties of these pressure tubes are highly anisotropic due to the strong transverse (circumferential) crystallographic texture of the (0001) basal plane normals of the hcp α-Zr grains that are the principal constituent of these tubes'

[4] The manuscript in this chapter is currently under review in the Journal of Nuclear Materials [R.O. Oviasuyi, R.J. Klassen, (submitted 15-02-2012)]

microstructure. For example, at 25°C the uniaxial yield stress in the transverse *TN* direction of the tube is 25% to 30% greater than in the axial *AN* direction. While the uniaxial yield stress and the stress-strain response in the transverse and axial directions of Zr-2.5%Nb tubes has been well characterized over the temperature range from 25°C to about 800°C [1], the temperature dependence of the yield stress in the through-thickness, Radial, *RN* direction of the pressure tube has not been reported. This may simply be the result of the practical difficulty involved with preparing and testing uniaxial specimens cut from the small, 4 mm, thickness of the pressure tubes.

Recently high temperature micro-indentation tests have reported that the ratio of the average indentation stress in the *TN* direction relative to the *RN* directions was 1.29:1 while that of the indentation stress in the *TN* direction relative to the *AN* directions was 1.26:1 at 25°C. These ratios decreased to 1.22:1 and 1.05:1 at 400°C [2]. While these findings suggest that the temperature dependence of the flow stress of the Zr-2.5%Nb tubes is dependent upon the loading direction, the fact that micro-indentation involves multi-axial stress / strain states prevents the accurate quantitative assessment of the mechanical anisotropy from indentation data. Uniaxial stress testing in the *TN*, *RN* and *AN* directions must ultimately be done to fully characterize the temperature-dependence of the mechanical anisotropy of extruded and cold-worked Zr-2.5%Nb CANDU pressure tube material.

The Hill's anisotropy criteria [3] has been used to describe the equivalent flow stress $\bar{\sigma}$ and equivalent plastic strain $\bar{\varepsilon}_p$ for textured Zr-2.5%Nb and other similarly anisotropic materials subjected to multiaxial stress σ_{ij} and resulting multiaxial plastic strain $\varepsilon_{p_{ij}}$ as [1, 4-8]

$$\bar{\sigma} = \sqrt{F(\sigma_{yy} - \sigma_{zz})^2 + G(\sigma_{zz} - \sigma_{xx})^2 + H(\sigma_{xx} - \sigma_{yy})^2 + 2L\sigma_{yz}^2 + 2M\sigma_{zx}^2 + 2N\sigma_{xy}^2} \qquad (3.1a)$$

and

$$\bar{\varepsilon_p} = \sqrt{F(\varepsilon_{p_{yy}} - \varepsilon_{p_{zz}})^2 + G(\varepsilon_{p_{zz}} - \varepsilon_{p_{xx}})^2 + H(\varepsilon_{p_{xx}} - \varepsilon_{p_{yy}})^2 + 2L\varepsilon_{p_{yz}}^2 + 2M\sigma_{p_{zx}}^2 + 2N\sigma_{p_{xy}}^2} \qquad (3.1b)$$

where *x*, *y*, and *z* represent three orthogonal directions in the material and *F*, *G*, *H*, *L*, *M*, and *N* are the anisotropy coefficients.

The Hill's anisotropic yield criteria (Eqs. 3.1 (a, b)) is perhaps the most widely-used approach for expressing the yield condition of mechanically anisotropic material subjected to multi-axial loading and has found extensive application in numerical techniques, such as finite element analyses. Given that numerical techniques are now universally used to predict the local stress and strain state in Zr-2.5%Nb pressure tube material it is important to have experimentally measured values of the Hill's anisotropy parameters *F*, *G*, and *H* that are specific to this material over the range of temperature up to, and including, the in-reactor operating temperature.

In this study, uniaxial compression tests are performed over the temperature range from 25^{o}C to 300^{o}C on small diameter cylindrical specimens cut from the *TN*, *RN*, and *AN* directions of an as-fabricated extruded and cold-drawn Zr-2.5%Nb CANDU pressure tube. The measured yield stress and flow curves in each direction are then analysed to obtain values for *F*, *G*, and *H* and to quantify their dependence upon temperature and the level of plastic strain.

3.2. Experimental procedure

3.2.1. Test material

The Zr-2.5%Nb pressure tube used in this study was supplied by the Atomic Energy of Canada Ltd, Chalk River Laboratories. The tube was fabricated by 11:1 extrusion of an annular billet at 720^{o}C followed by 27% cold-drawing at room temperature and a 24 hours stress relief autoclave treatment at 400^{o}C. The microstructure of the tube consists of hcp α-Zr grains (the primary micro-constituent), elongated in the axial direction of the tube, surrounded by a thin discontinuous layer of Nb-rich bcc β precipitates. The α grains have average dimensions of about 0.2, 1.0 and 5.0 μm in the *RN*, *TN* and *AN* directions of the tube respectively.

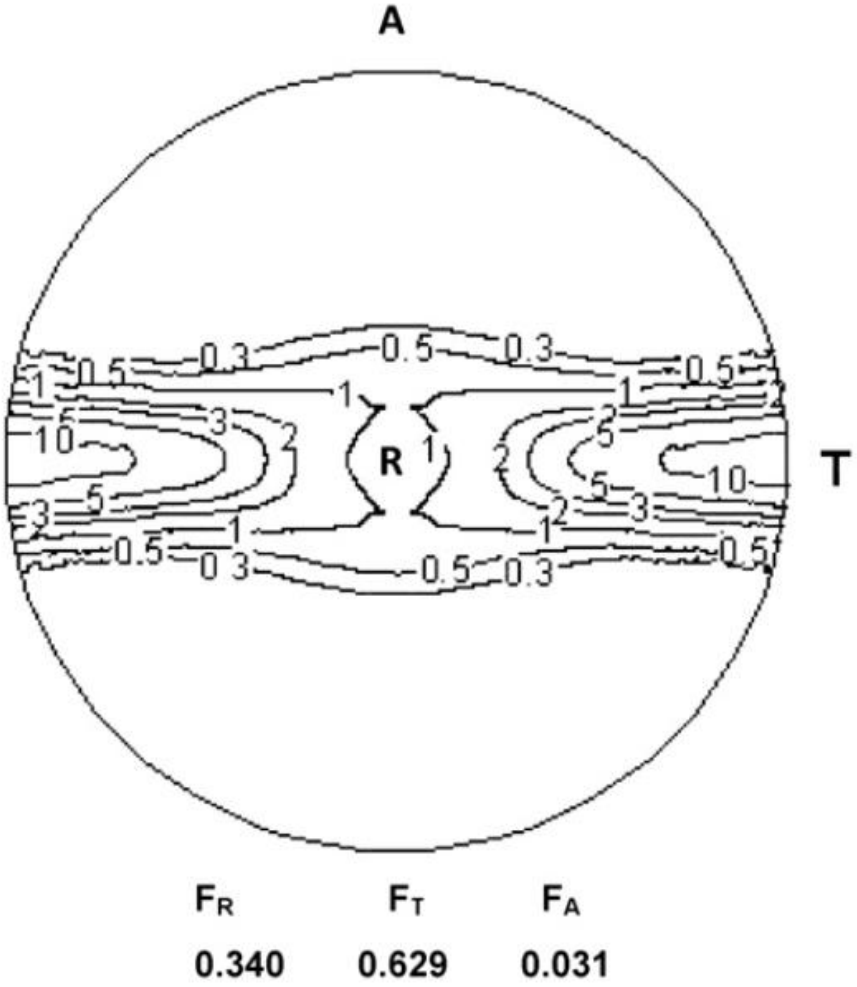

Figure 3.1. (0002) basal pole figure of the extruded and cold drawn Zr-2.5%Nb CANDU pressure tube used in this study. This pole figure was supplied, along with the pressure tube test material, by the Atomic Energy of Canada Ltd, Chalk River Laboratory. The letters *A, T,* and *R* refer to the Axial, Transverse, and Radial directions of the pressure tube. The quantities F_R, F_T, and F_A refer to the calculated basal pole fraction aligned in the radial, transverse and axial directions respectively as calculated by the method of Kearns [14].

The α-grains are textured with the majority of the (0002) basal plane normals aligned parallel to the transverse direction of the pressure tube [1-2, 9-13]. The (0002) basal pole figure of this material is shown in Figure 3.1. This pole figure was obtained from x-ray diffraction measurements where the intensity of the (0002) Bragg reflection was measured as a function of angular orientation within the test sample. Following the method proposed by Kearns [14] one can determine, from such an assessment, the "resolved orientation parameter *f*" which essentially expresses the effective fraction of (0002) poles aligned parallel to the principal directions of the sample. The orientation distribution of the basal pole normals within the Zr-2.5%Nb pressure tube material used in this study resulted in $f_{AN} = 0.03$, $f_{RN} = 0.34$, and $f_{TN} = 0.62$.

3.2.2. Mechanical testing

Three groups of cylindrical specimens, each specimen of 2 mm diameter and 3 mm length, were tested in uniaxial compression at 25, 100, 200, and 300^{o}C. Each group contained cylindrical specimens machined with their axial direction aligned along the *TN*, *RN* and *AN* directions of the pressure tube (Figure 3.2).

Uniaxial compression tests were performed with a screw-actuated load frame. The cylindrical specimen was compressed, at a constant cross-head velocity of 0.022 mm/s, to different pre-specified strain levels and then unloaded. The elevated temperature compression tests were performed by fitting a proportionally-controlled split-zone electrical resistance furnace around the test specimen and the compression platens.

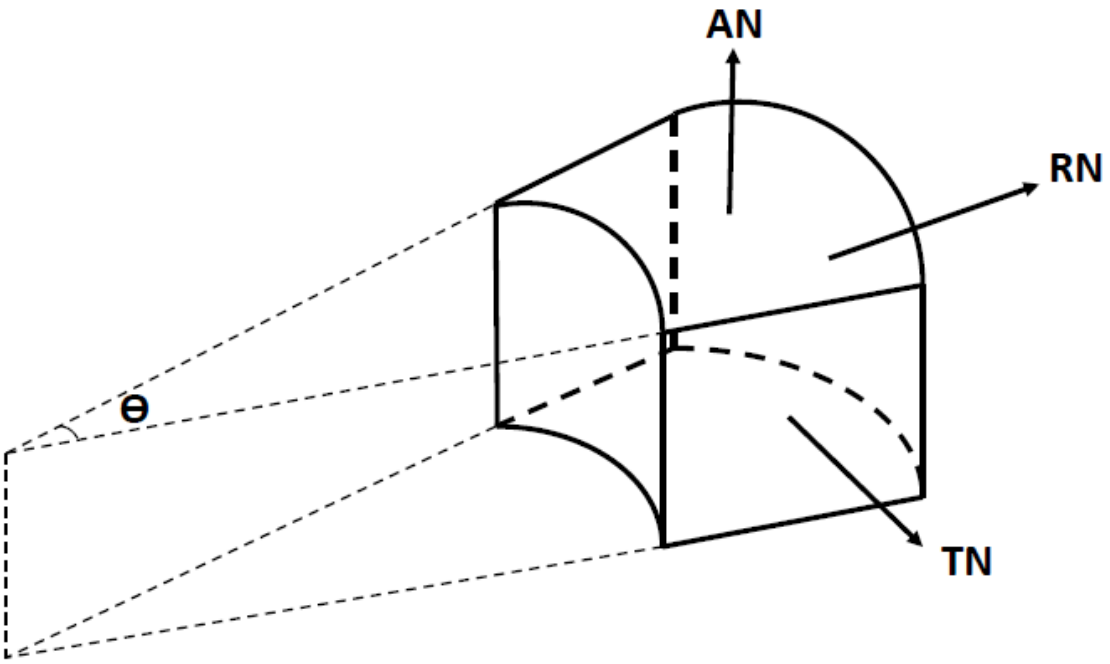

Figure 3.2. A schematic illustration showing a section of a Zr-2.5%Nb pressure tube indicating the orthogonal *TN*, *RN* and *AN* directions from which the cylindrical compression samples were cut.

Over ten cylindrical specimens were tested in each orientation at 25^{o}C while at least eight specimens were tested at each orientation and at each elevated temperature from 100 to 300^{o}C. During compression testing the cylindrical samples increased in diameter and, due to their mechanical anisotropy, developed an elliptical cross-section. The maximum and the minimum diameter of the elliptical cross-section of each specimen were measured after unloading.

Additional cylindrical samples from each orientation and each test temperature were loaded continuously to failure to assess the total ductility and the mode of failure.

3.3. Results and discussions

3.3.1. The engineering stress – strain response

Figure 3.3 shows the engineering stress versus strain curves from *AN*, *TN*, and *RN* oriented Zr-2.5%Nb specimens at 25^{o}C and 300^{o}C. The material displays a well defined yield stress that is considerably higher when the stress is applied along the *TN* compared to the *AN* or the *RN* directions [1-2, 9-13, 15]. Similar plots were obtained for all the orientations and temperatures tested.

The source of the anisotropic yield stress arises from the fact that, for the Zr-2.5%Nb alloy, plastic deformation occurs by dislocation glide on a pyramidal $\{10\bar{1}1\}<\bar{1}\,\bar{1}23>$ slip system when a uniaxial normal stress is applied along the $\langle 0001 \rangle$ while dislocation glide occurs, at a lower resolved shear stress, on the prismatic $\{10\bar{1}0\}<\bar{1}2\bar{1}0>$ slip system when the applied normal stress is acting in a direction other than $\langle 0001 \rangle$ [16-20]. This theory is further confirmed by the data obtained in this study. Figure 3.4(a) depicts the dependence of the 0.2% offset engineering yield stress upon the resolved orientation parameter *f*' which expresses the fraction of (0002) poles aligned parallel to the loading direction of the specimen. This plot indicates that the initial yield stress of this Zr-2.5%Nb alloy is increased when the normal stress is applied in the direction corresponding to a high fraction of (0002) basal pole normals.

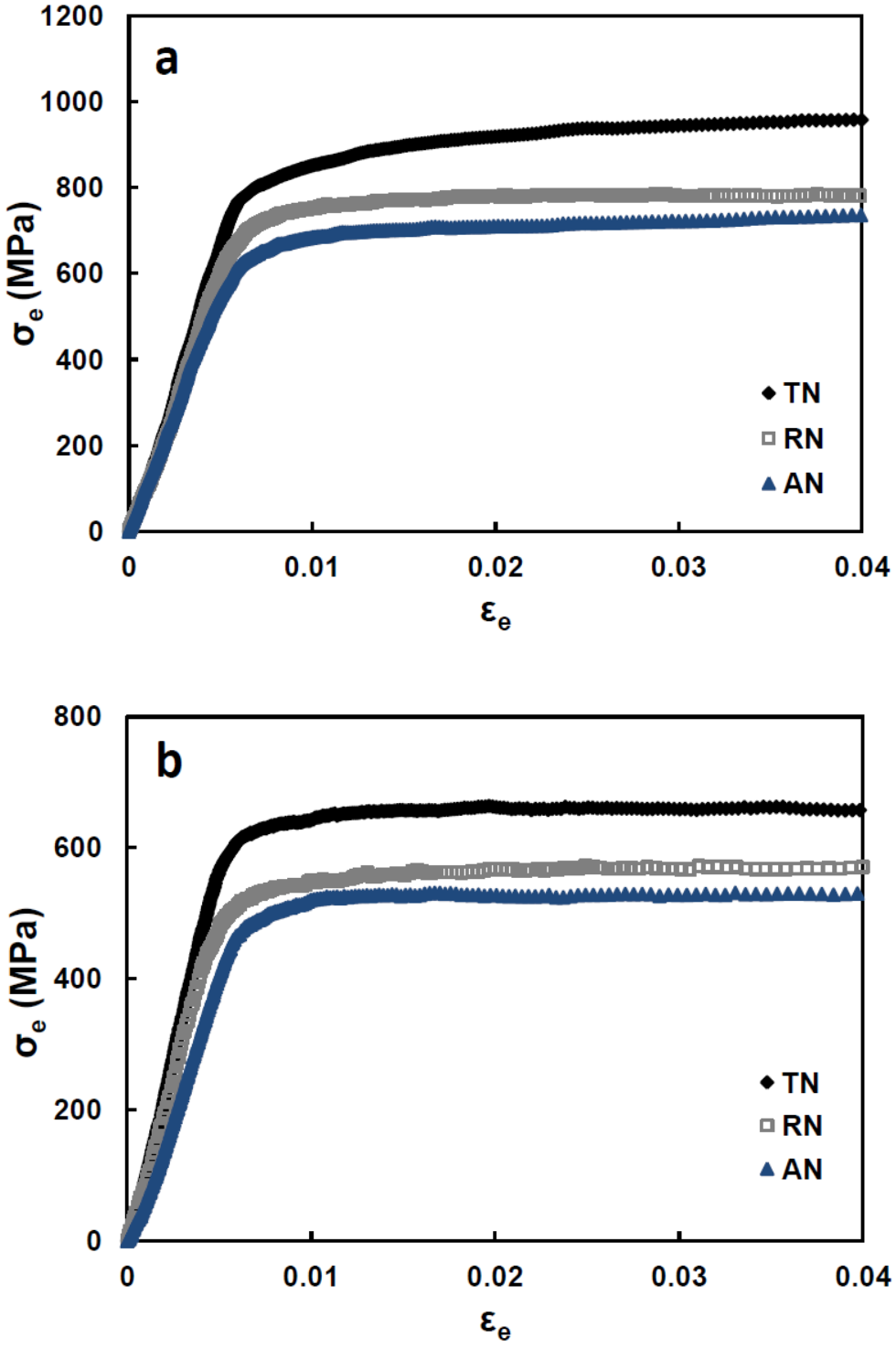

Figure 3.3. Engineering stress plotted against engineering strain for *AN*, *RN*, and *TN* compression tests performed at (a) 25 °C and (b) 300°C.

Figure 3.4(b) depicts the decrease in the 0.2% offset yield stress with increasing temperature. Included in this plot are data reported, for the same Zr-2.5%Nb pressure tube material, by Christodoulou et al [1]. The yield stress decreases continuously with increasing temperature. Since no sharp discontinuities exist in the temperature dependence of the yield stress one can deduce that the microstructure of the test material, and the mechanism of deformation, did not undergo sudden changes over the temperature range from 25^{o}C to 300^{o}C [12, 21-28].

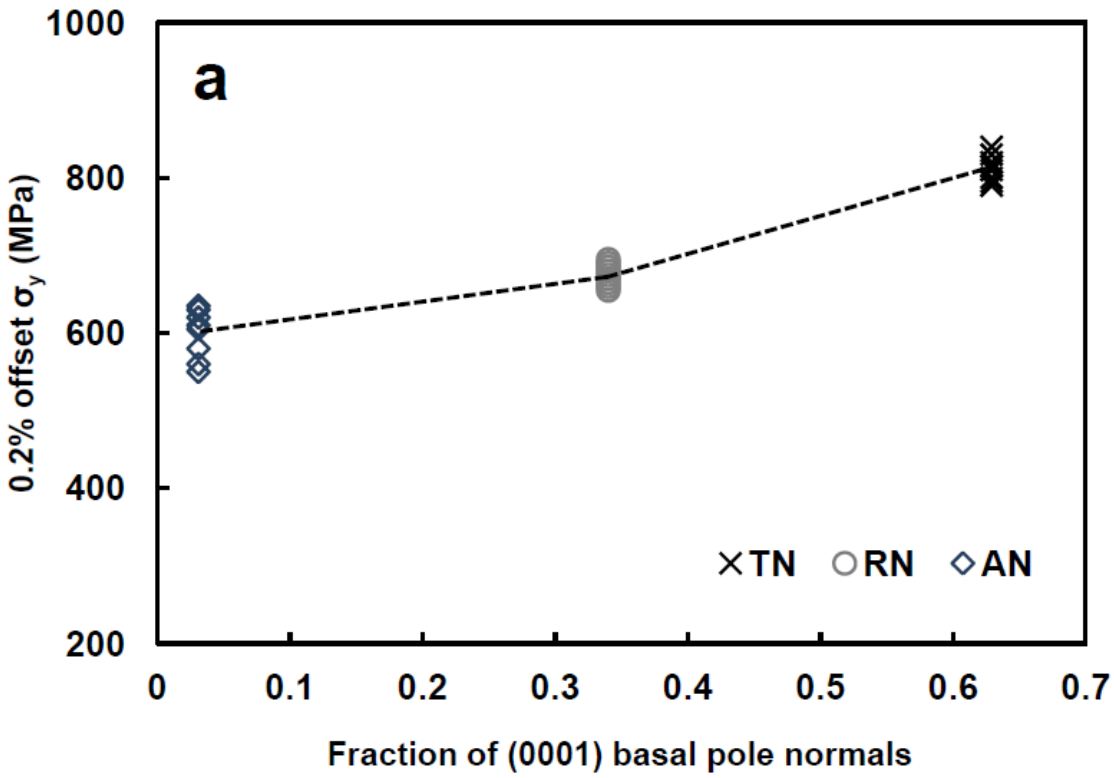

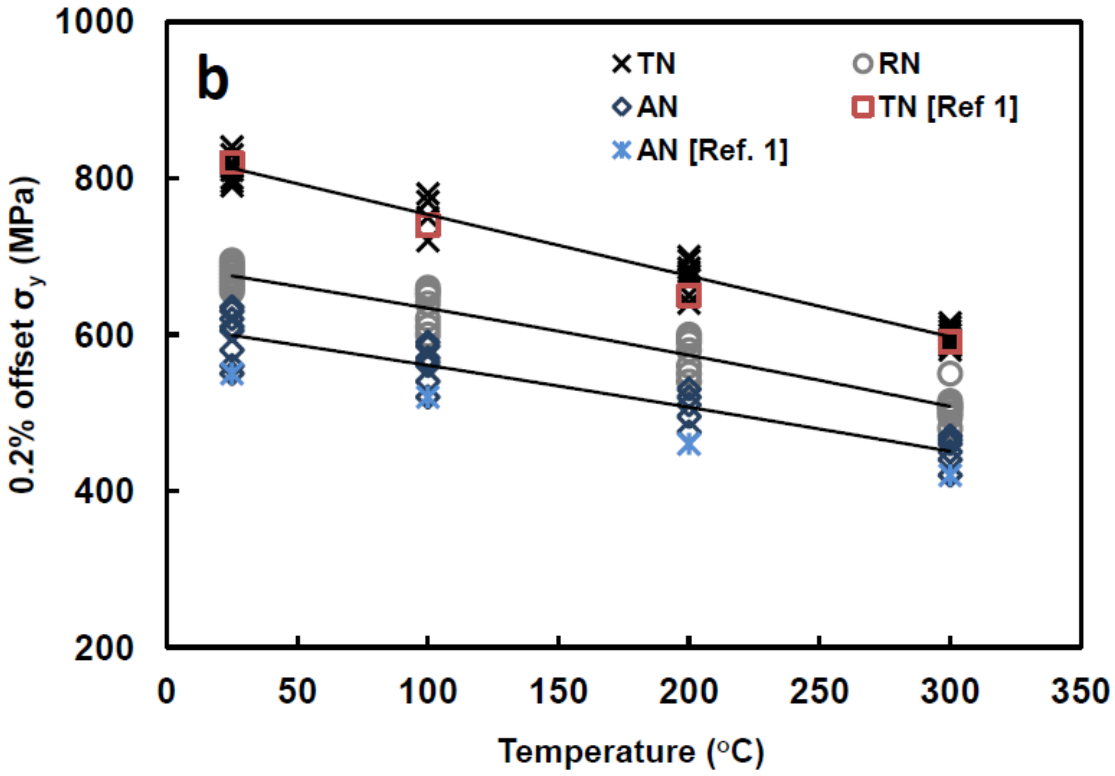

Figure 3.4. Plots of 0.2% offset engineering yield stress versus (a) fraction of (0002) basal pole normals aligned in the direction of compression at 25 °C and (b) test temperature. Figure (b) includes data from previously reported uniaxial tensile tests performed in the *AN* and *TN* directions [1].

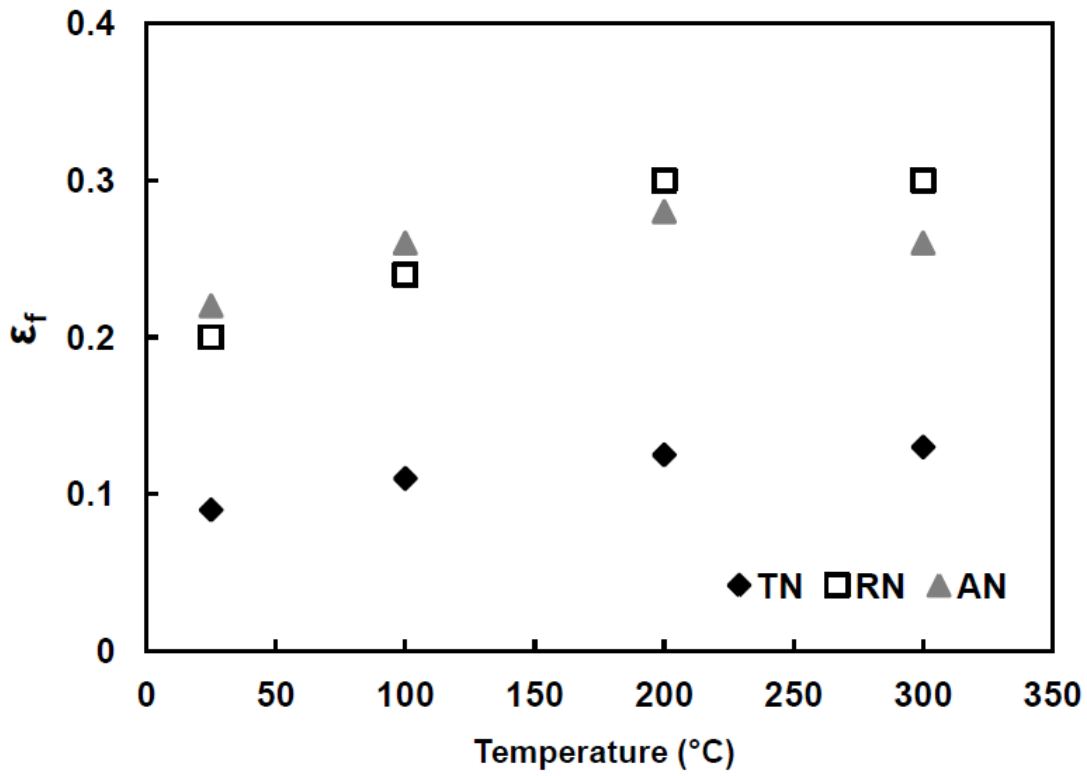

Figure 3.5. Plot of the average engineering fracture strain versus temperature for the *AN*, *RN*, and *TN* loading directions.

The average engineering fracture strain is plotted against temperature in Figure 3.5. The samples compressed in the *TN* direction were far less ductile than those compressed in the *RN* or *AN* directions. Samples failed by sudden shear instability when compressed in the *TN* direction (Figure 3.6(a)) while the samples compressed in the *AN* direction at 25 °C underwent considerably more uniform plastic strain prior to shear failure. This is indicated by the increased number of slip steps visible on the surface of the deformed *AN* sample (Figure 3.6(b)). Samples compressed in the *RN* direction showed a combination of both characteristics. None of the samples tested to failure displayed significant barrelling.

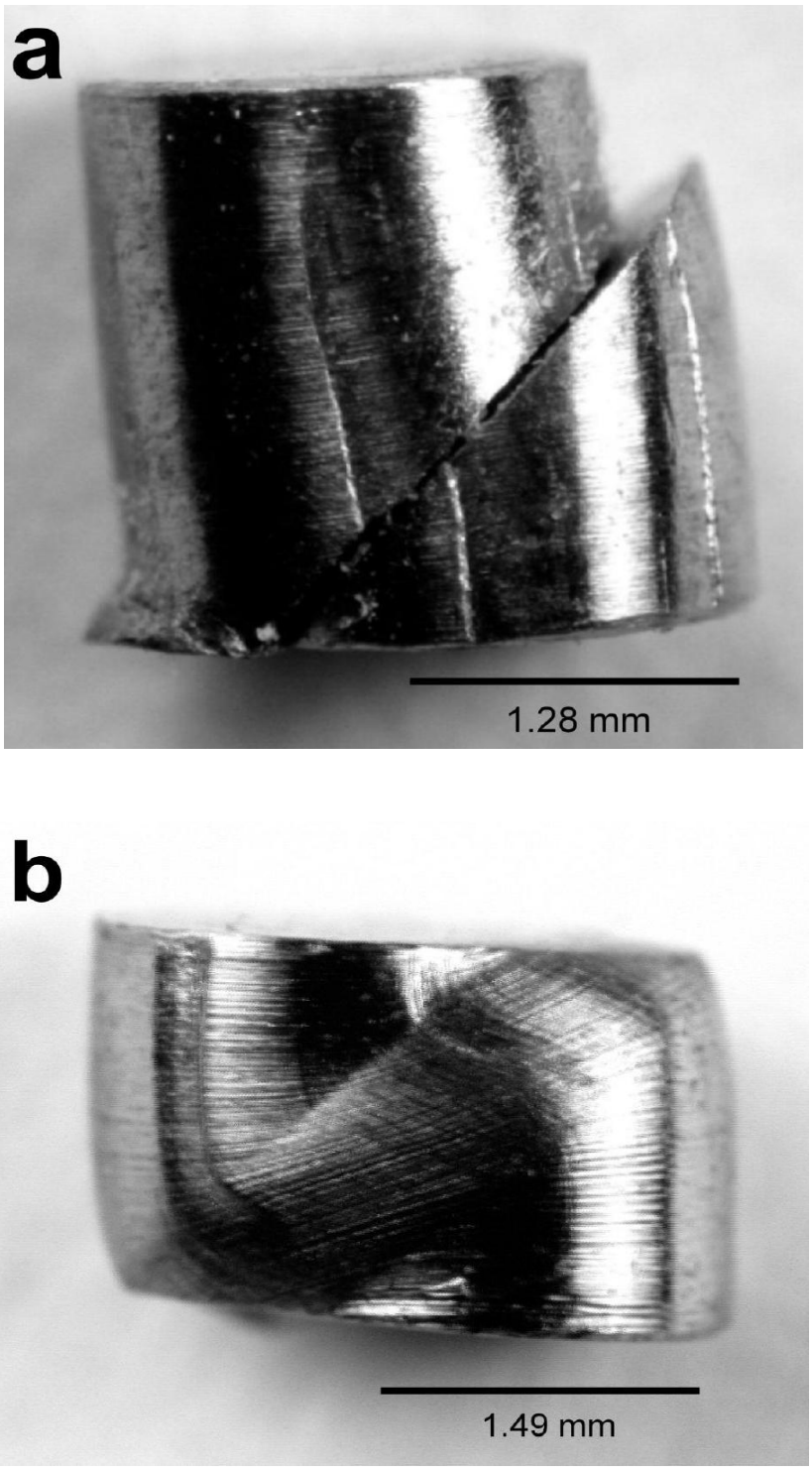

Figure 3.6. Images of cylindrical pillars from Zr-2.5%Nb pressure tube compressed in the (a) *TN* and (b) *AN* direction to failure at 25°C.

3.3.2. The true stress – strain response

Plots depicting the true stress σ versus true plastic strain $\varepsilon_{p,}$ in the loading direction, are shown in Figure 3.7(a-d) for compression tests performed at 25, 100, 200, and 300^{o}C on *AN*, *RN*, and *TN* specimens. Each σ - ε_p curve was obtained by loading multiple specimens to different levels of strain and then measuring their length and diameter after unloading. Each test therefore contributes only one point to the σ versus ε_p plots in Figure 3.7. The scatter in the data indicates the degree of sample-to-sample variability resulting from the test technique. The measured plastic strain data shown in Figures 3.7 corresponds to tests that were unloaded well before the onset of failure by shear instability.

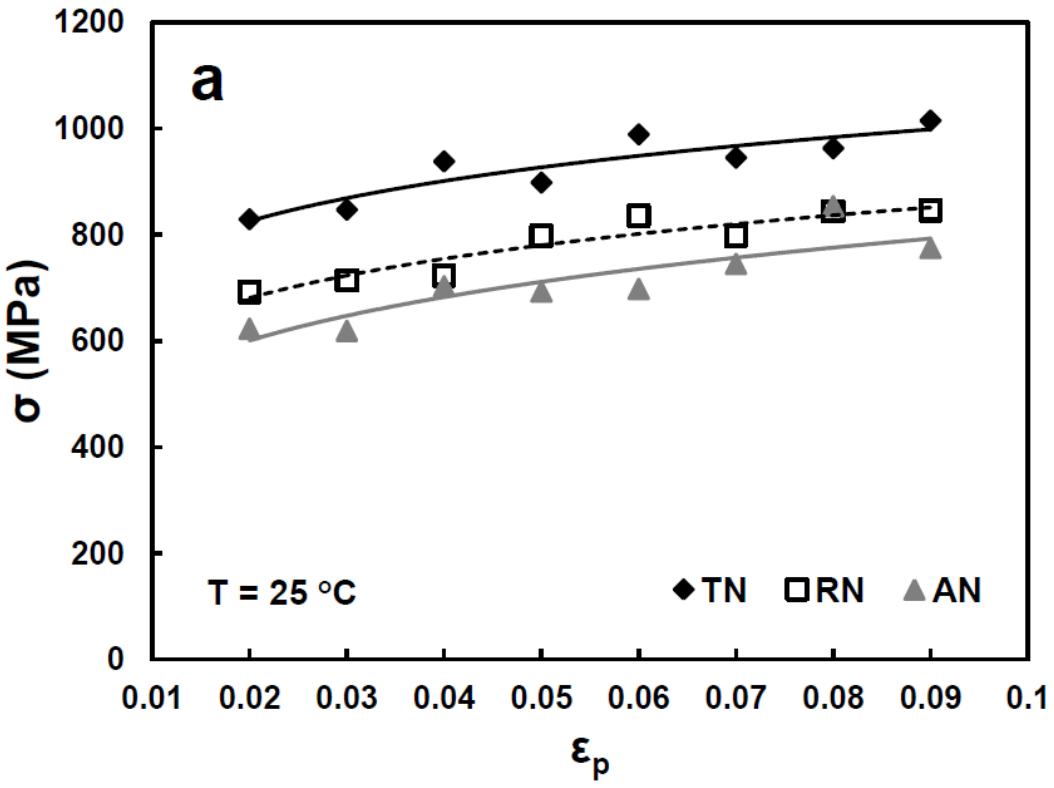

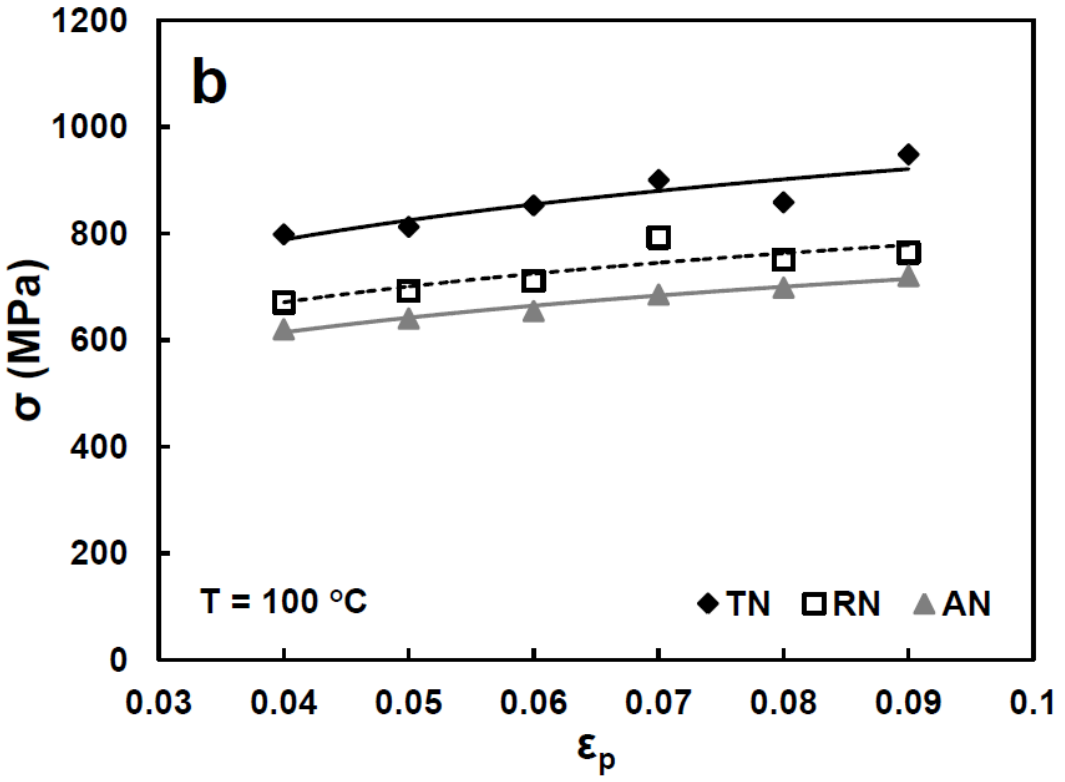
b
1200
1000
800
600
400
200
0
σ (MPa)
T = 100 °C
TN
RN
AN
0.03
0.04
0.05
0.06
0.07
0.08
0.09
0.1
εp

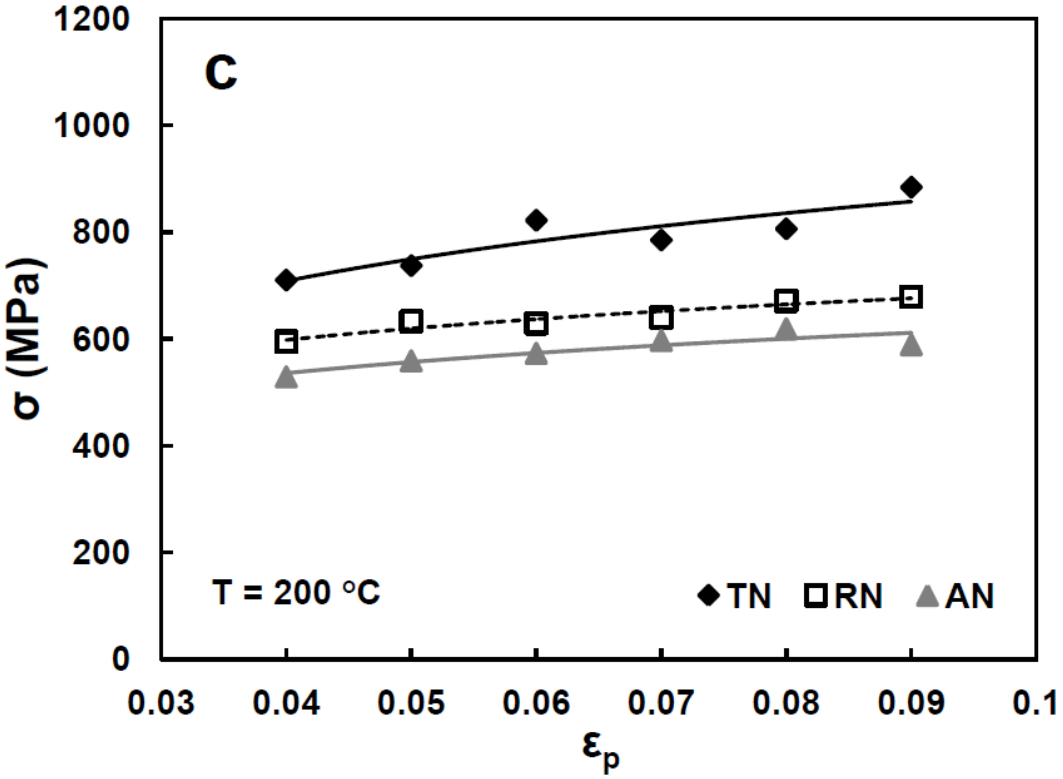
c
1200
1000
800
600
400
200
0
σ (MPa)
T = 200 °C
TN
RN
AN
0.03
0.04
0.05
0.06
0.07
0.08
0.09
0.1
εp

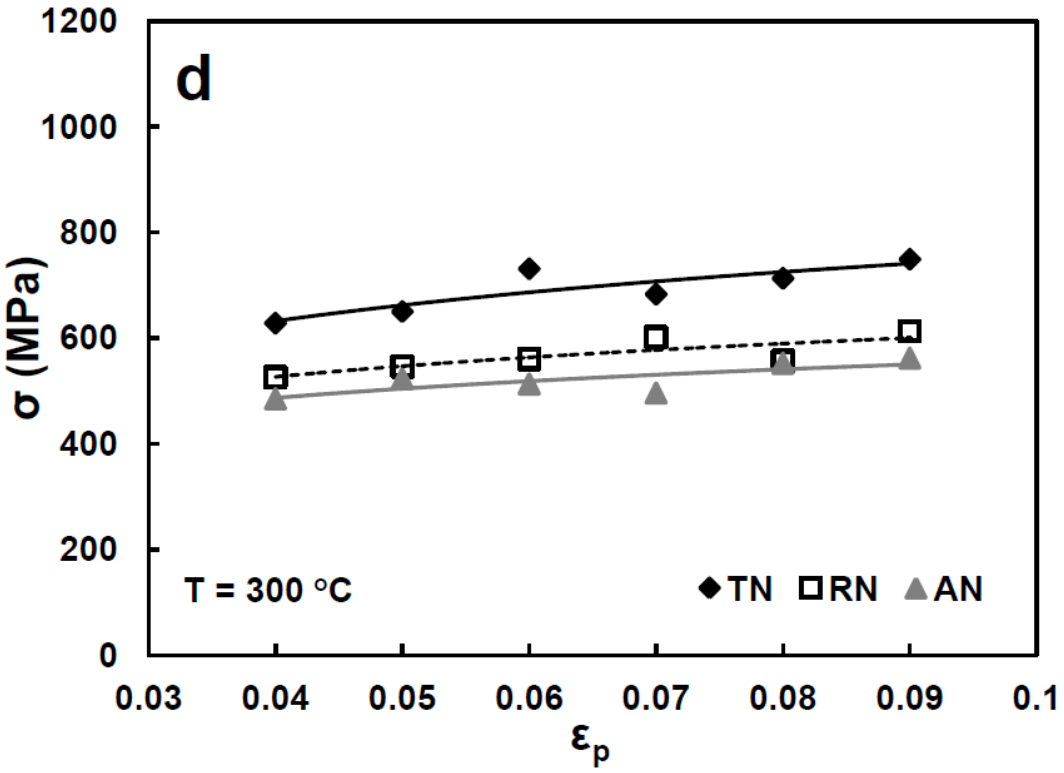

Figure 3.7. Graphs of true stress versus true plastic strain from compression tests performed on samples deformed to specified plastic strain values in the *TN*, *RN* and *AN* directions at; (a) at 25 °C, (b) at 100 °C, (c) at 200 °C and (d) at 300 °C.

Empirical power-law functions, of form shown below, were fitted to the σ - ε_p trends

$$\sigma(\varepsilon_p) = \sigma_0 + A\varepsilon_p^n \tag{3.2}$$

In this equation $\sigma(\varepsilon_p)$ is the true flow stress, ε_p is the true plastic strain, σ_0, A, and n are material constants. The solid lines shown in Figure 3.7(a-d) represent the fitted $\sigma(\varepsilon_p)$.

3.3.3. Determination of anisotropy coefficients *F*, *G* and *H*

We are ultimately interested in developing expressions for the equivalent flow stress $\bar{\sigma}$ and the equivalent plastic strain $\bar{\varepsilon}_p$ such that the σ - ε_p response obtained from uniaxial stress compression tests performed in the *AN*, *RN*, and *TN* directions of the pressure tube

(Figure 3.7) all fall upon a single $\bar{\sigma}$ versus $\bar{\varepsilon}_p$ curve. This will be undertaken by applying the Hill's anisotropic yield criteria (Equations 3.1(a,b)) and determining suitable values for the anisotropy coefficients *F*, *G*, and *H*. We use the same convention used previously [1] where $\bar{\sigma}$ is equated to the uniaxial yield stress in the *AN* direction of the Zr-2.5%Nb test material. In the case where only normal stress is applied, as is the case for the uniaxial tests performed in this study, Eq. 3.1(a) becomes

$$\sigma_{Ayield} = \bar{\sigma} = \sqrt{F(\sigma_{AN-}\sigma_{TN})^2 + G(\sigma_{TN} - \sigma_{RN})^2 + H(\sigma_{RN} - \sigma_{AN})^2} \tag{3.3}$$

where the directions *x*, *y*, and *z* are replaced with the orthogonal *AN*, *RN*, and *TN* directions of the pressure tube (Figure 3.2). The anisotropy coefficients *F*, *G*, and *H* can then be expressed in terms of the ratios of the uniaxial yield stress in the *RN*, *AN*, and *TN* directions as:

$$F + H = 1 \tag{3.4a}$$

$$F + G = \left(\frac{\sigma_{AN_{yield}}}{\sigma_{TN_{yield}}} \right)^2 \tag{3.4b}$$

$$G + H = \left(\frac{\sigma_{AN_{yield}}}{\sigma_{RN_{yield}}} \right)^2 \tag{3.4c}$$

For isotropic materials, $F = G = H = ½$ however for anisotropic materials the values of these constants will be distinctly different and may depend upon temperature and plastic strain.

Figures 3.8 shows the calculated *F*, *G*, and *H* values as a function of the test temperature. The calculated anisotropy factors remain essentially constant at *F=0.38 ± 0.01, G=0.202 ± 0.001,* and *H=0.62 ± 0.01* over the temperature range tested. The magnitude of these values are very similar to the values *F=0.378, G=0.100,* and *H=0.623* determined, by a combination of experimental measurement and application of a deformation model, by Christodoulou et al for similar Zr-2.5%Nb material [1].

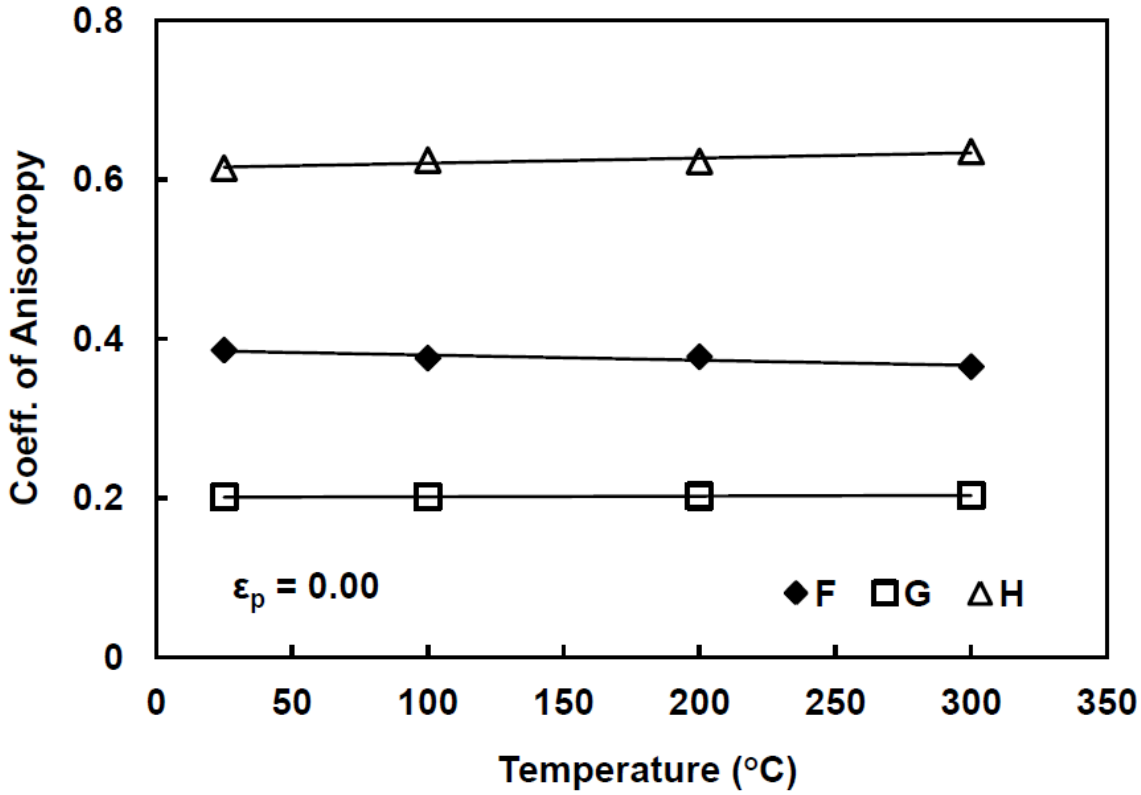

Figure 3.8. Plots of the Hill's anisotropy coefficients *F*, *G* and *H* of the 0.2% offset yield stress versus temperature from 25°C to 300°C.

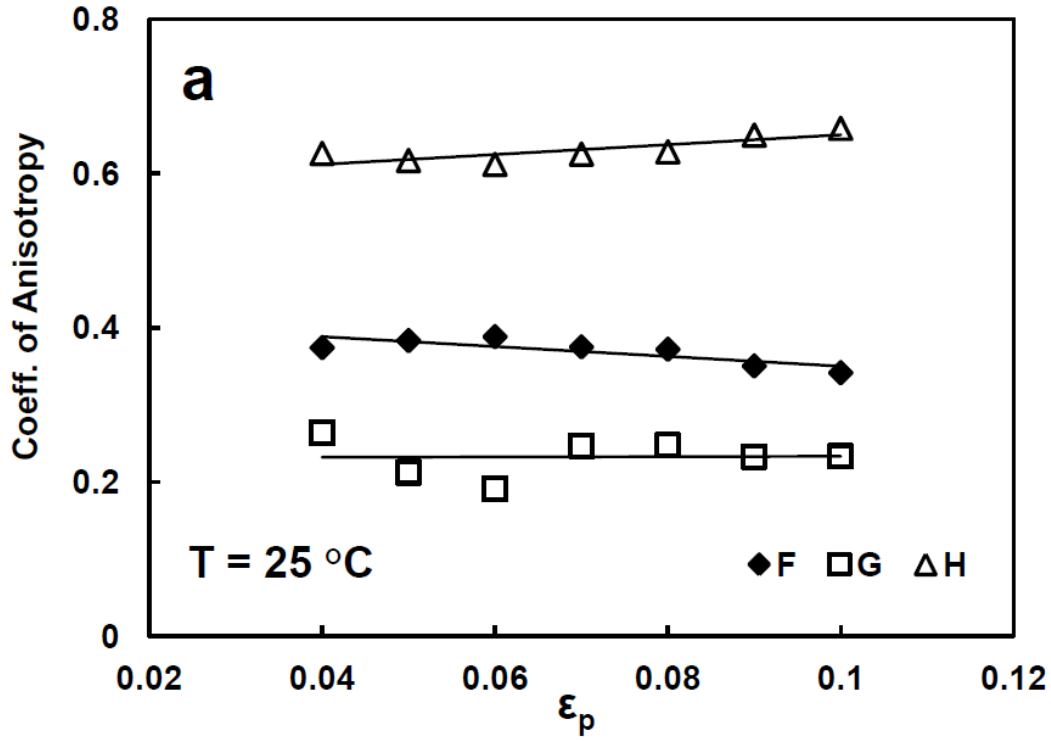
a
Coeff. of Anisotropy
0.8
0.6
0.4
0.2
0
0.02
0.04
0.06
0.08
0.1
0.12
ε_p
T = 25 °C
F G H

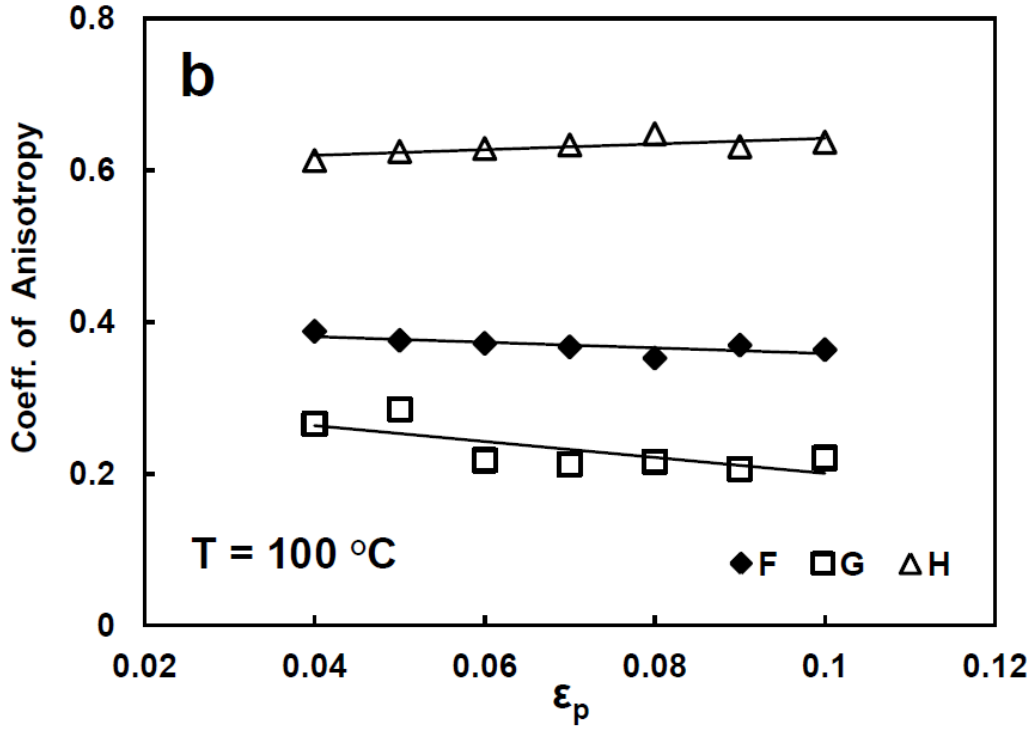
b
Coeff. of Anisotropy
0.8
0.6
0.4
0.2
0
0.02
0.04
0.06
0.08
0.1
0.12
ε_p
T = 100 °C
F G H

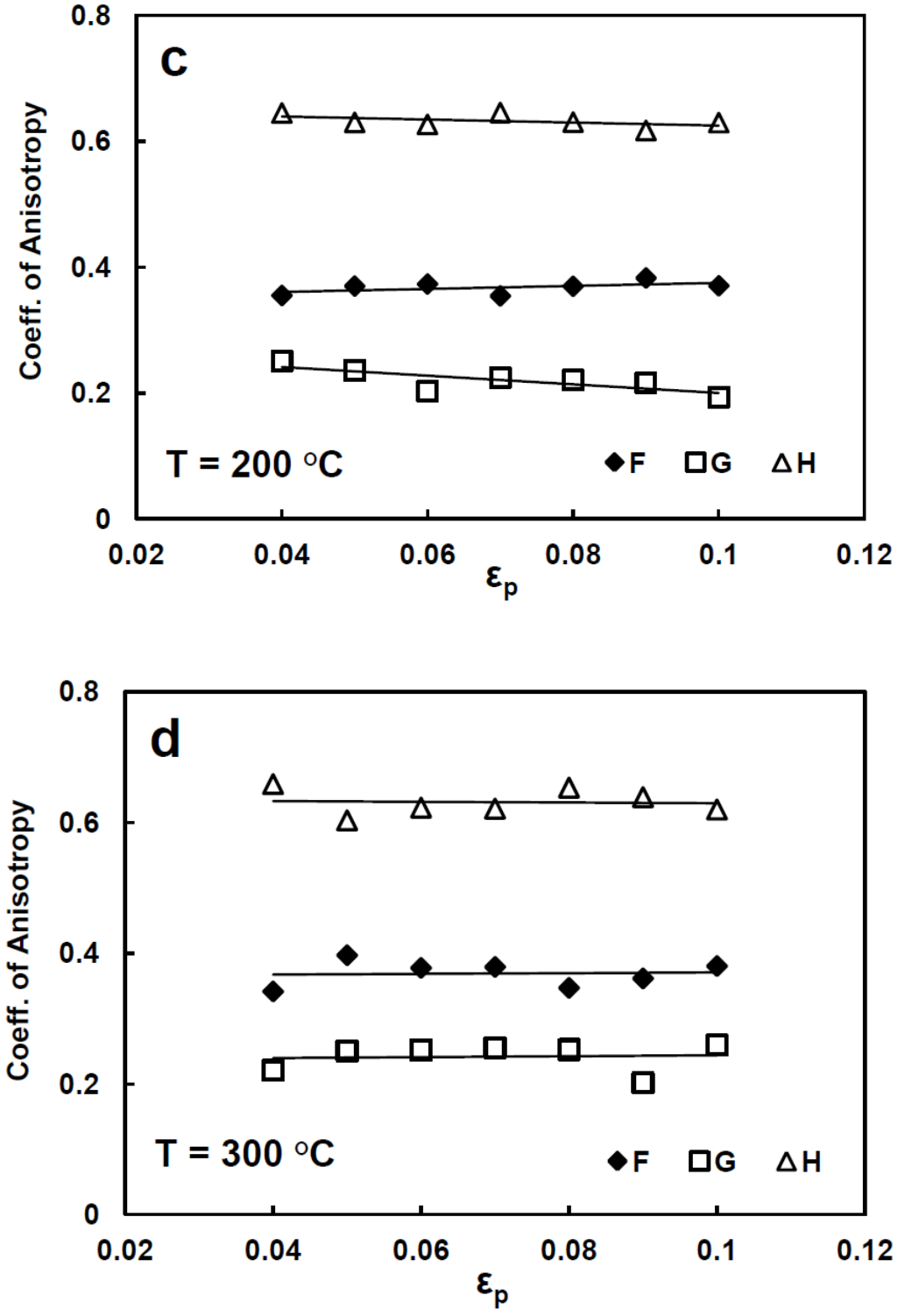

Figure 3.9. Plots of the Hill's anisotropy coefficients *F*, *G* and *H* versus plastic strain in the loading direction at temperatures of 25°C to 300°C.

The Hill's anisotropy coefficients may also be a function of the level of plastic strain if the strain hardening behaviour of the test material is anisotropic. Figure 3.9 shows the calculated Hill's anisotropy coefficients, determined from the measured flow stress data in Figures 3.7, as a function of the true plastic strain ε_p in the loading direction. The graphs indicate that, once again, the magnitude of *F*, *G*, and *H* is not significantly affected by the magnitude of axial plastic strain up to a plastic strain of about 10%.

3.3.4. Assessing the calculated *F*, *G* and *H* values

To assess the effectiveness of the calculated anisotropy coefficients for transforming the diverse σ - ε_p response displayed by the Zr-2.5%Nb pressure tube material, when stressed in different directions, onto a single $\bar{\sigma}$ versus $\bar{\varepsilon}_p$ curve we substitute the average values of the Hill's anisotropy coefficients, determined from the 0.2% offset yield stress data, and calculate the equivalent true stress $\bar{\sigma}$ and the equivalent true plastic strain $\bar{\varepsilon}_p$ for each set of σ and ε_p shown in Figure 3.7.

Although, the data in Figure 3.7 were obtained from the application of a uniaxial normal stress, the resulting plastic strain is multiaxial. The compressed specimen can be assumed to undergo only normal plastic strain. This is consistent with the fact that the data shown in Figure 3.7 were obtained from tests which displayed no barrelling and were stopped well before the onset of final shear failure. The plastic strain in the loading direction is plotted, as the abscissa coordinate in Figure 3.7. The two out-of-plane normal strains, ε_{max} and ε_{min}, were calculated by measuring the maximum and minimum diameters of the elliptical cross-section of the deformed test specimen. This was accomplished by assuming that the ratio $\varepsilon_{max}/\ \varepsilon_{min}$ was equal to the ratio of the measured maximum and minimum diameters such that

$$c = \frac{\varepsilon_{max}}{\varepsilon_{min}} = \frac{\ln\ (D_0/D_{max})}{\ln\ (D_0/D_{min}\ )} \tag{3.5}$$

where D_0 is the diameter of the cross-section of the pillar before deformation while D_{max} and D_{min} are the maximum and minimum diameters of the elliptical cross-section of the pillar respectively after deformation. Invoking the requirement that volume is conserved

during plastic deformation results in the following expressions for ε_{max} and ε_{min} in terms of the measured ε_{axial} and the ratio c

$$\varepsilon_{\max} = -\frac{c}{c+1}\varepsilon_{axial} \tag{3.6a}$$

$$\varepsilon_{\min} = -\frac{1}{c+1}\varepsilon_{axial} \tag{3.6b}$$

Equations 3.6(a,b) allows one then to calculate, for any experimentally obtained values of ε_{axial} and c , the three corresponding orthogonal normal plastic strains $\varepsilon_{p_{AN}}$, $\varepsilon_{p_{RN}}$ and $\varepsilon_{p_{TN}}$. The equivalent plastic strain can then be calculated from Eq. 3.1(b) as

$$\bar{\varepsilon}_p = \sqrt{F(\varepsilon_{p_{AN}} - \varepsilon_{p_{TN}})^2 + G(\varepsilon_{p_{TN}} - \varepsilon_{p_{RN}})^2 + H(\varepsilon_{p_{RN}} - \varepsilon_{p_{AN}})^2} \tag{3.7}$$

The resulting $\bar{\sigma}$ versus $\bar{\varepsilon}_p$ curves from all the uniaxial compression tests performed in the *AN*, *RN*, and *TN* orientations are shown in Figure 3.10. While the $\bar{\sigma}$ versus $\bar{\varepsilon}_p$ data for a given temperature follow the same trend regardless of loading direction, there exists considerable scatter in the experimental data. Since every data point in this figure is obtained from a separate compression test, the scatter shown can be attributed to the sensitivity limits of the test technique; particularly the limited sensitivity of our calculated ε_{max} and ε_{min} which were determined by measuring D_{max} and D_{min}.

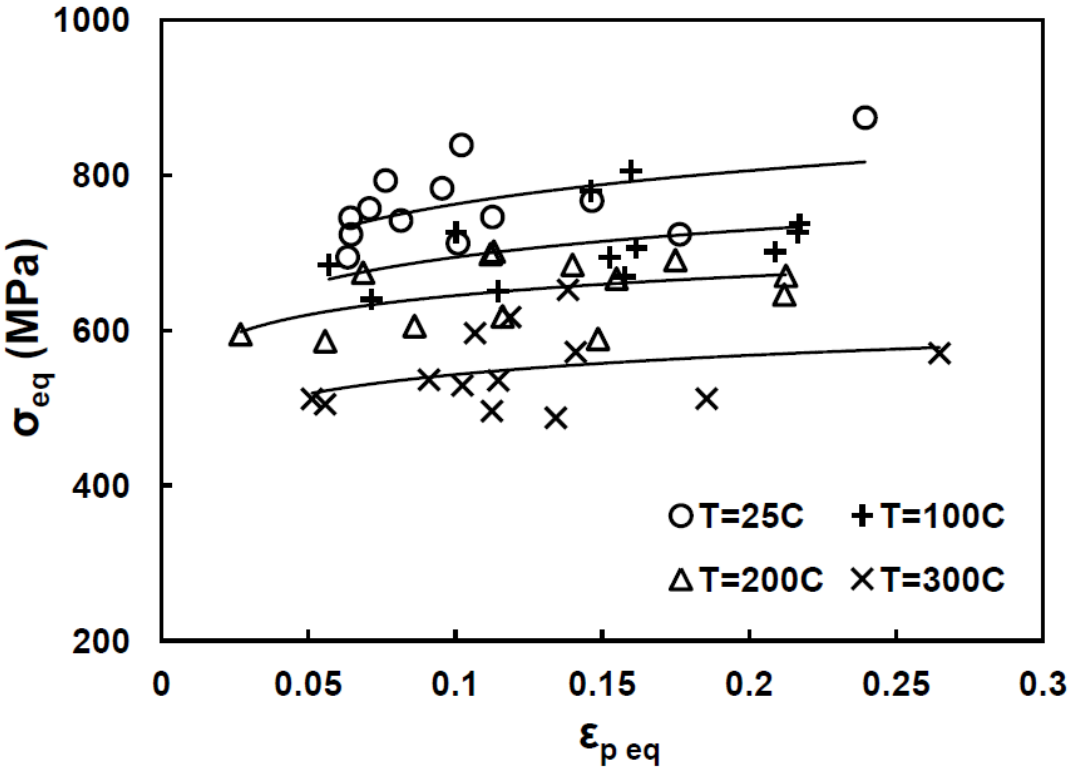

Figure 3.10. Plot of equivalent stress versus equivalent plastic strain in all directions for all samples compressed using stress data from figure 3.7(a-d).

To reduce the scatter shown in Figure 3.10 the data are re-plotted in Figure 11 using the average stress $\sigma(\varepsilon_p)$ (Eq. 3.2) substituted into Eq. 3.1(a) to calculate $\bar{\sigma}$. This effectively removes the sample-to-sample variability resulting from the sensitivity limits of the test technique. The resulting $\bar{\sigma}$ versus $\bar{\varepsilon}_p$ curves show excellent convergence of the σ - ε_p data obtained from uniaxial stress compression tests in all three pressure tube directions onto a single $\bar{\sigma}$ versus $\bar{\varepsilon}_p$ curve.

To further assess the accuracy of the calculated anisotropy coefficients (*F=0.38, G=0.202,* and *H=0.62)* previously reported σ - ε_p data from uniaxial tensile tests performed, at 300^{o}C in the *AN* and *TN* orientations, on similar extruded and cold-drawn Zr-2.5%Nb pressure tube material [1] were used to calculate their corresponding $\bar{\sigma}$ and $\bar{\varepsilon}_p$ data. The reported uniaxial stress data, along with the anisotropy coefficients

determined in this study, were used to calculate $\bar{\sigma}$ via Eq. 3.1(a). The reported ε_{axial} data were then used to calculate $\bar{\varepsilon}_p$ by determining the values of $\varepsilon_{p_{AN}}$, $\varepsilon_{p_{RN}}$ and $\varepsilon_{p_{TN}}$ using Eq.3.6(a,b) and the parameter *c* obtained from this study.

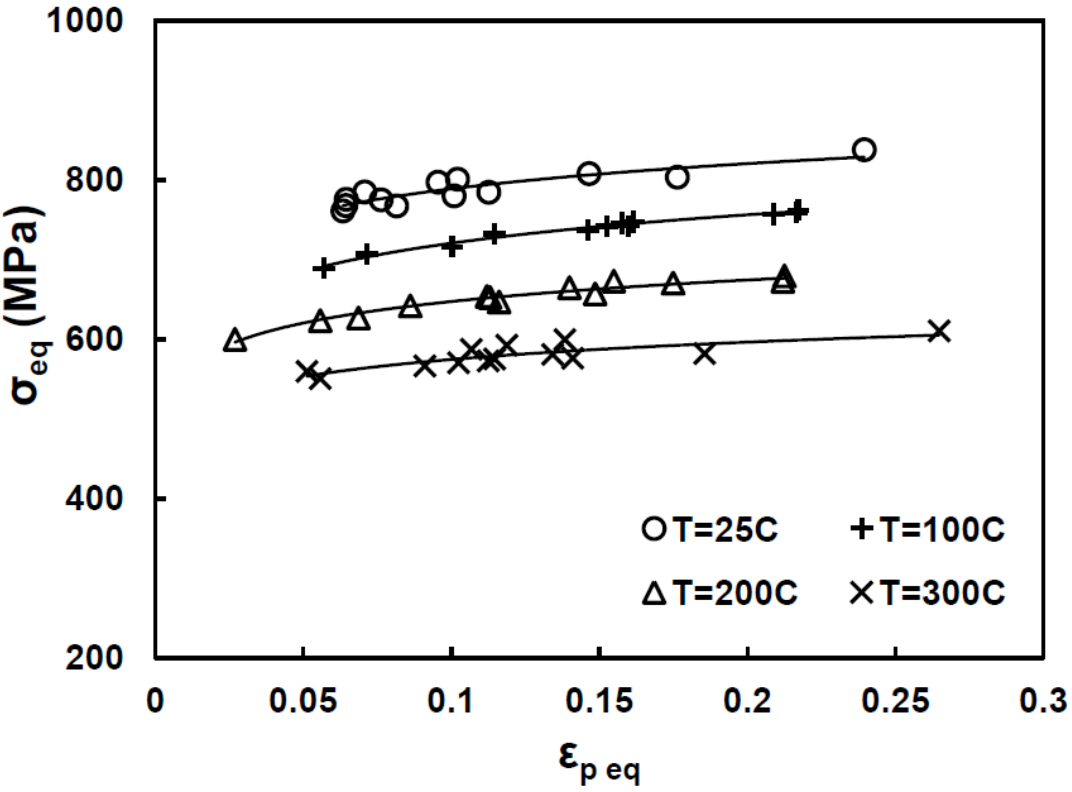

Figure 3.11. Plot of equivalent stress versus equivalent plastic strain in all directions for all samples compressed using average stress values obtained from Eq. 3.2.

Figure 3.12 shows the resulting $\bar{\sigma}$ versus $\bar{\varepsilon}_p$ curve. This plot contains data from previously reported uniaxial tension tests performed in the *AN* and *TN* directions in addition to data obtained from *AN*, *RN*, and *TN* tests performed in this study at 300^{o}C. The data from these diverse tests all fall on essentially a single $\bar{\sigma}$ versus $\bar{\varepsilon}_p$ curve. This demonstrates that the anisotropic coefficients, *F=0.38, G=0.202,* and *H=0.62*, represent

very accurately the anisotropic flow behaviour of extruded and cold-drawn Zr-2.5%Nb pressure tube material.

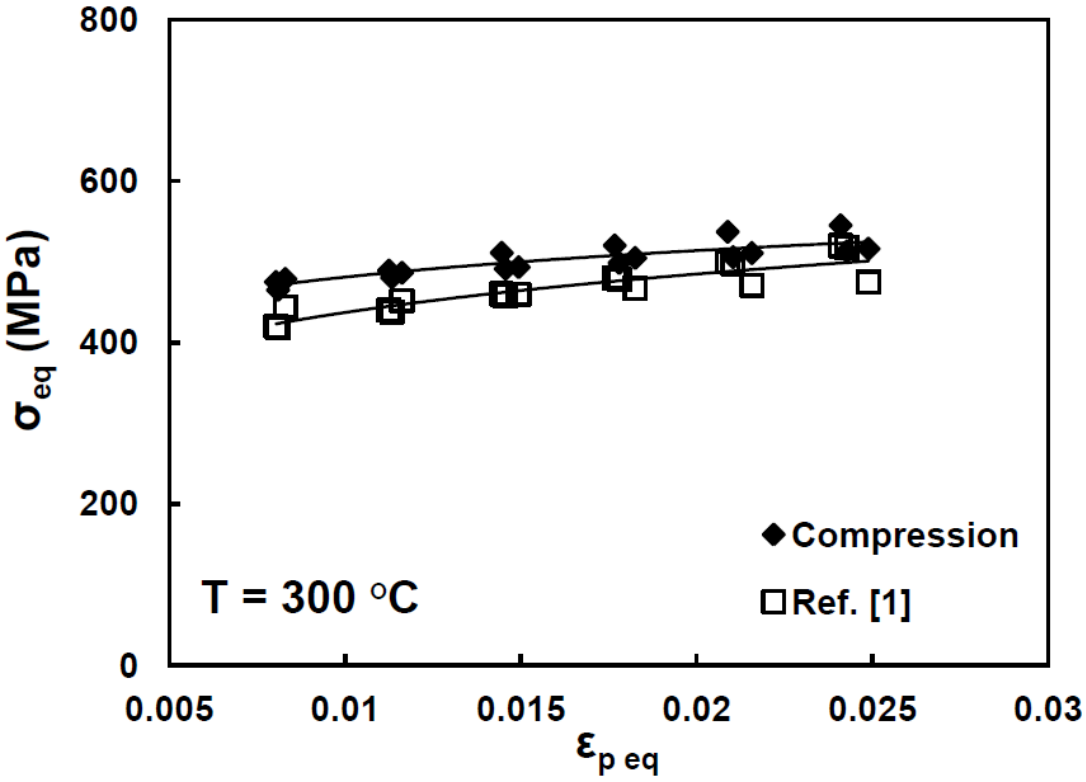

Figure 3.12. Plot of equivalent stress versus equivalent plastic strain for all samples compressed at 300°C along with calculated $\bar{\sigma}$ versus $\bar{\varepsilon}_p$ values obtained from previously reported σ - ε_p data [1] along with the values of *F=0.38*, *G=0.202*, and *H=0.62* from this study.

3.4. Conclusion

In this chapter uniaxial compression testing, involving multiple specimens deformed to various levels of plastic strain, were used to assess the true stress versus true plastic strain response in the *AN*, *RN*, and *TN* directions of the mechanically anisotropic Zr-2.5%Nb CANDU pressure tube material over the temperature range from 25 to 300°C. Analysis of

the data resulted in the determination of the Hill's anisotropy coefficients $F=0.38 \pm 0.01$, $G=0.202 \pm 0.001$, and $H=0.62 \pm 0.01$. These coefficients were found to be independent of temperature and plastic strain over the range of temperature from 25 to 300°C and plastic strain up to 10%.

Application of the experimentally determined *F*, *G*, and *H* values to calculate the equivalent stress $\bar{\sigma}$ and equivalent plastic strain $\bar{\varepsilon}_p$ demonstrated that stress – strain data obtained from uniaxial tests performed in the *AN*, *RN*, and *TN* directions all fell on a single $\bar{\sigma}$ versus $\bar{\varepsilon}_p$ curve. This was also demonstrated to be true when previously reported uniaxial stress – strain data, from tests performed in the *AN* and *TN* directions, was similarly analysed with the *F*, *G*, and *H* values obtained from this study.

The results of this study are scientifically significant since they are, to the best of the authors' knowledge, the first experimentation-based determination of the Hill's anisotropy coefficients *F*, *G*, and *H* of extruded and cold-drawn Zr-2.5%Nb CANDU pressure tube material over a wide temperature range extending up to the 300°C in-service temperature of this tubing. These anisotropy coefficients are directly useful in numerical models of Zr-2.5%Nb pressure tube components where calculating the onset of plastic deformation is of interest.

Acknowledgements

The authors wish to thank the Natural Science and Engineering Research Council of Canada (NSERC) and the University Network of Excellence in Nuclear Engineering (UNENE) who provided financial support for this research. Finally, we offer a special note of thanks to Drs. B. Leitch and S. St. Lawrence of the Atomic Energy of Canada Ltd (*Chalk River Laboratories)* for providing the Zr-2.5%Nb pressure tube material used in this study.

References

[1] N. Christodoulou, P.A. Turner, E.T.C. Ho, C.K. Chow, M.R, Levi, Metall. Mater. Trans. A. 31A (2000) 409.

[2] B. Bose, R.J. Klassen, J. Nucl. Mat. 419 (2011) 235.

[3] R. Hill, Proc. Royal Soc. Lond. series A 193 (1948) 1033.

[4] T. Kuwabara, S. Ikeda, K. Kuroda, J. Mater. Process. Tech. 80-81 (1998) 517.

[5] K.-H. Kim, J. Mech. Phys. Solids 40 (1992) 127.

[6] C. Vial, W.F. Hosford, R.M. Caddell, Int. J. Mech. Sci. 25 (1983) 899.

[7] A. Yonezu, K. Yoneda, H. Hirakata, M. Sakihara, K. Minoshima, Mater. Sc. & Eng. A 527 (2010) 7646.

[8] K.L. Murty, S. Hussein, Y.H. Jung, Scripta Metallurgica, 19 (1985) 1045.

[9] N. Christodoulou, P.A. Turner, C.N. Tomé, C.K. Chow, R.J. Klassen, Metall. Mater. Trans. A 33 (2002) 1103.

[10] V. Perovic, G.C. Weatherly, R.G. Fleck, Can. Metall. Quart. 24 (1985) 253.

[11] M. Griffiths, C.K. Chow, C.E. Coleman, R.A Holt, S. Sagat, V.F. Urbanic, Atomic Energy of Canada Ltd Research Report, AECL-10844, 1993, p. 1.

[12] R.O. Oviasuyi, R.J. Klassen, J. Nucl. Mat. 421 (2012) 54.

[13] P.A. Ross-Ross, W. Evans, W.J. Langford, Atomic Energy of Canada Ltd, Research Report, AECL-4262, 1972, p. 2.

[14] J.J. Kearns, Report No. WAPD-TM-472, Westinghouse Co., Pittsburgh PA, 1965.

[15] S.S. Kim, Y.S. Kim, S.C. Kwon, S.B. Ahn, K.N. Choo, Trans. 15th Int. Conf. Struc. Mech. In Reactor Tech. (SMiRT-15) 1999, p 263.

[16] R.A. Holt, M. Griffiths, R.W. Gilbert, J. of Nucl. Mat., v. 149 (1987), p. 51

[17] A. Akhtar, J. of Nucl. Mat., v. 47 (1973), p. 79

[18] E. Tenckhoff, J of ASTM Int., v. 2 (2005), p. 119

[19] A. Salinas-Rodriguez., M.G. Akben, J.J. Jonas, E.F. Ibrahim, Canadian Metallurgical Quarterly, v. 24 (1985), p. 259

[20] M. Griffiths, J. of Nucl. Mat., v. 205 (1993), p. 225

[21] Z.L. Pan, S. St Lawrence, P.H. Davies, M. Griffiths, S. Sagat, Zirconium in the Nuclear Industry: 14th International Symposium of ASTM, 2 (2005).

[22] B.S. Rodchenkov, A.N. Semenov, Nucl. Eng. Des. 235 (2005) 2009.

[23] E.F. Ibrahim, J. Nucl. Mat. 102 (1981) 214.

[24] W.J. Langford, L.E.J. Mooder, J. Nucl. Mat. 39 (1971) 292.

[25] C.R. Cupp, J. Nucl. Mat. 6 (1961) 241.

[26] X. Wei, J.R. Theaker, M. Griffiths, Zirconium in the Nuclear Industry: 15th International Symposium of ASTM, 5 (2007).

[27] Y.-M. Cheong, S.-C. Kwon, H.-K. Jung, J. Mat Sc. 35 (2000) 1195.

[28] B.A. Cheadle, C.E. Ells, W. Evans, J. Nucl. Mat. 23 (1967) 199.

Chapter 4

4. Deducing the stress-strain response of anisotropic Zr-2.5%Nb pressure tubing by spherical indentation testing[5]

In this chapter we developed a method of analysis by which the average stress – plastic strain flow curve of mechanically anisotropic materials can be deduced from spherical indentation test data. Our analysis is based upon spherical indentation tests performed on the extruded and cold-drawn Zr-2.5%Nb CANDU pressure tube material over the range of temperature from 25°C to 300°C. The indentation force and depth data were analysed and σ_{avg} and ε_{avg} were calculated using previously reported equations developed for spherical indentation of isotropic material which were then modified, by incorporating the appropriate Hill's anisotropy coefficients, to characterize the anisotropic yield stress of the indented material. The resulting flow curves were dependent on indentation direction and correspond closely with flow curves obtained from previously reported conventional uniaxial stress tests performed on the Zr-2.5%Nb material. Indentation tests performed with large, 200 μm, and small, 40 μm, diameter spheres indicate that for small diameter indentations, when the indentation depth is less than several micrometers, the calculated σ_{avg} is heavily influenced by the depth dependence of the yield strength of the indented material.

4.1. Introduction

Spherical indentation testing has been proposed as an alternative to conventional uniaxial stress testing for determining the stress - strain response of strain-hardening materials. The technique has the clear advantage that it can be performed on very small samples with minimal pre-test preparation. The key feature that enables spherical indentation to be used to determine the stress-strain response is the fact that the average representative

[5] The manuscript in this chapter is currently under review in the Journal of Nuclear Materials [R.O. Oviasuyi, R.J. Klassen, (Submitted (06-03-2012)]

strain ε_{avg} increases with spherical indentation depth. Tabor proposed early on that for spherical indentation with an indenter of diameter D, ε_{avg} can be expressed as [1]

$$\varepsilon_{avg} \approx 0.4\frac{r_c}{D} \tag{4.1}$$

where r_c is the indentation contact radius (Figure 4.1). This equation for ε_{avg} is still widely used [1-5] and allows for the possibility of obtaining the average stress - strain response of a material simply by measuring the indentation pressure P_m, which is related to the flow stress of the material, and the ε_{avg} over a sufficiently large range of indentation depth.

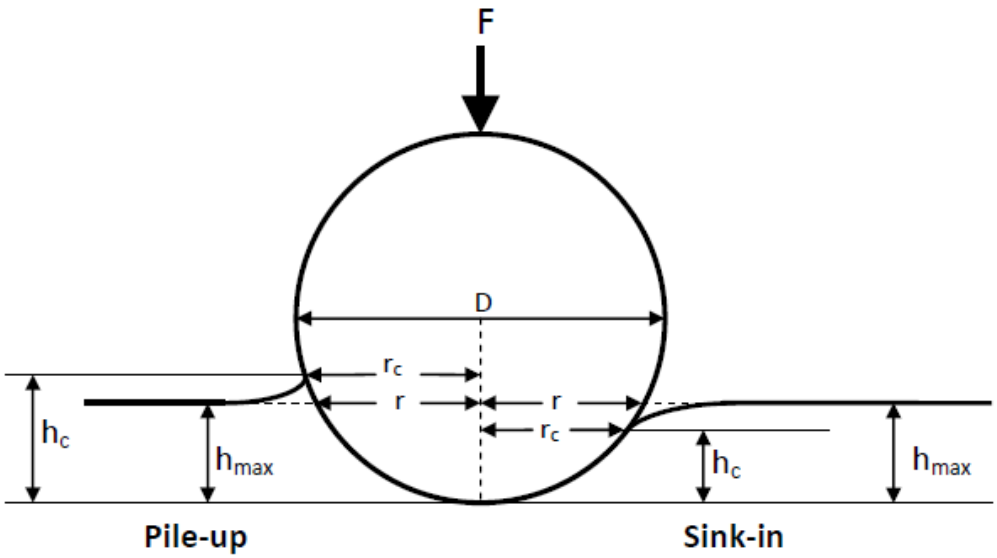

Figure 4.1. An idealized cross-sectional depiction of a spherical indentation illustrating the parameters used in the calculation of the average indentation stress and strain.

Several methods have been proposed to determine the average representative stress σ_{avg} from spherical indentation load - depth data. While these methods usually assume that the indentation is made in mechanically isotropic material [2-13], several researchers have considered, with the application of numerical simulation, the spherical indentation

of mechanically anisotropic material [14-16]. In this paper we present a technique for determining σ_{avg} for a mechanically anisotropic material, extruded and cold-drawn Zr-2.5%Nb CANDU pressure tubing, which is based upon the application of equations developed to express σ_{avg} of an isotropic material along with an expression to account for the mechanical anisotropy in terms of the Hill's anisotropy coefficients of the indented material.

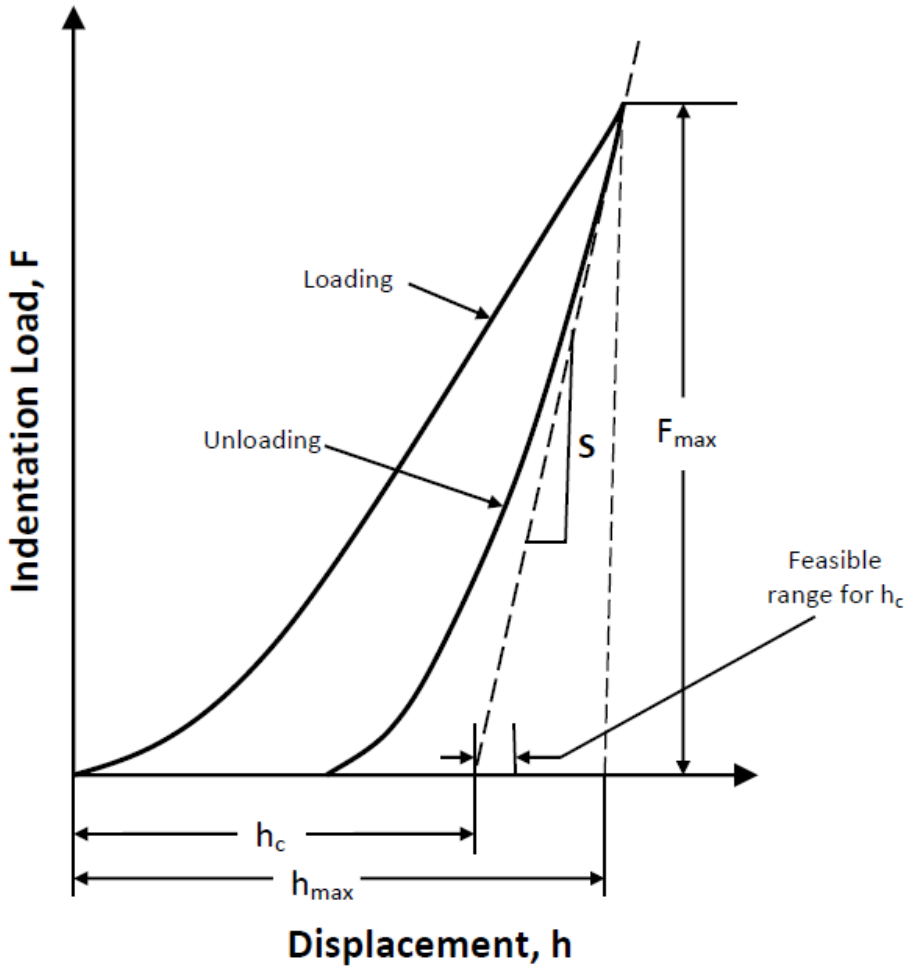

Figure 4.2. Idealized plot of indentation load versus displacement from a spherical indentation test. This plot illustrates parameters, obtained from such a test, that are used to calculate the average indentation stress.

Figure 4.2 shows the indentation force versus indentation depth resulting from a typical spherical indentation test. F_{max} is the applied indentation load required to indent the material to a specific depth of h_{max}. The actual contact radius r_c between the indenter and the indented sample depends greatly upon the amount of material pile-up, or sink-in, that occurs around the spherical indentation and can be wrongly estimated by as much as 60% when this pile-up / sink-in is neglected [9, 13]. The degree of pile-up or sink-in depends upon the work-hardening coefficient n of the indented material and the following equation for r_c has been developed for isotropic material [4]

$$r_c = \left(c\left(Dh_c - h_c^2\right)\right)^{1/2} \tag{4.2a}$$

where c is [13, 17]:

$$c = \frac{5}{2}\left(\frac{2-n}{4+n}\right) \tag{4.2b}$$

In these equations h_c is the indentation contact depth measured relative to the edge of the contact surface expressed as $h_c = h_{max} - 0.75F_{max}/S$ and S is the elastic unloading compliance determined from the indentation force - depth curve (Figs. 4.1, 4.2) [18].

While the average stress σ_{avg} resulting from spherical indentation must be proportional to the average indentation contact pressure P_m, the actual proportionality is complex and has been much studied [1-16, 19-20]. The following equation expresses σ_{avg} for the case of spherical indentation involving elastic-plastic deformation of an isotropic work-hardening material [19]

$$\sigma_{avg} = \frac{P_m}{\psi} = \frac{1}{\psi}\left(\frac{F_{\max}}{\pi r_c^2}\right) \tag{4.3a}$$

and

$$\psi = 1.1 + 0.017468\phi \tag{4.3b}$$

where

$$\phi = \frac{E}{\sigma_{yield}\left(1-\upsilon^2\right)}\left(\frac{h_c}{r_c}\right) \tag{4.3c}$$

The terms *E*, *ν*, and σ_{yield} refer to the Young's modulus, Poisson's ratio and the initial Von-Mises equivalent yield stress of the indented material respectively. Eq. (4.3b) was derived from a linear fit to the plot of P_m/σ_{yield} versus $\ln\phi$ where ϕ is a dimensionless parameter, of value between 2 and 100, in the elastic-plastic deformation regime (Fig. 4, Ref [19]).

In this chapter we will consider the spherical indentation of a mechanically anisotropic material, extruded and cold-drawn Zr-2.5%Nb pressure tube material used in CANDU nuclear reactors. We will perform spherical indentation tests on the Axial Normal (*AN*), Radial Normal (*RN*), and Transverse Normal (*TN*) planes of the tube (Figure 4.3) at temperature from 25^{o}C to 300^{o}C and apply Eqs. (4.1- 4.3) along with previously reported values for the Hill's anisotropy coefficients *F*, *G*, and *H* of this material to calculate the σ_{avg}-ε_{avg} response. The σ_{avg}-ε_{avg} curves obtained from these tests will then be compared with those obtained from uniaxial compression and tension tests performed on the same material to illustrate that the spherical indentation data provide an accurate indication of the σ_{avg}-ε_{avg} response of this anisotropic material. The spherical micro-indentation tests are performed with large, 200 μm diameter, and small, 40 μm diameter, spheres to assess the indentation depth limitations of this spherical micro-indentation technique. The ultimate goal of this study is to develop a testing technique that can accurately measure the σ_{avg}-ε_{avg} response of an anisotropic material of minimal sample size and, thus, offer a potentially useful method for performing in-cell mechanical testing of radioactive nuclear materials.

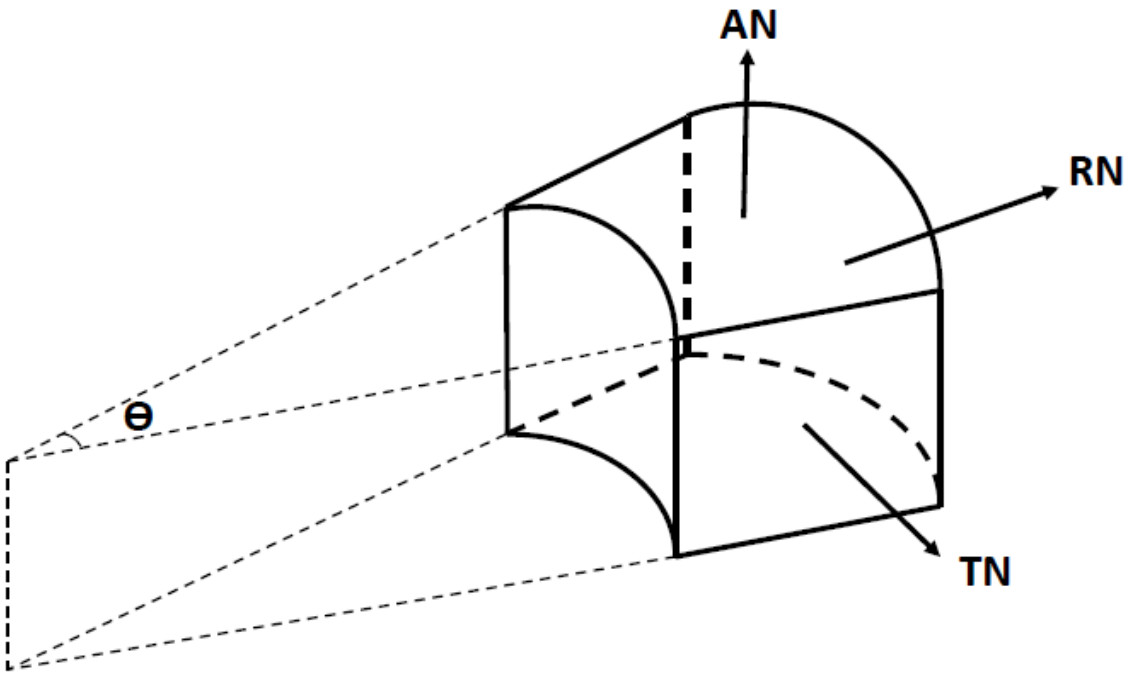

Figure 4.3. Schematic illustration of a section of the pressure tube showing the three orthogonal planes on which the spherical indentation tests were performed.

4.2. Experimental Procedure

The material used in this study was an as-fabricated Zr-2.5%Nb CANDU reactor pressure tube supplied by the Chalk River Laboratories (Chalk River, Ontario, Canada). The tube was fabricated by 11:1 extrusion of an annular billet at 720^{o}C followed by 27% cold-drawing at room temperature and a 24 hours stress relief autoclave treatment at 400^{o}C [21-25]. The mechanical properties of this pressure tube have been studied extensively with uniaxial compression tests and with micro-indentation testing [21-22, 25-32]. Table 4.1 lists the previously reported uniaxial yield stress σ_{yield} of this material [26, 28]. The strain hardening exponent n, used for the analysis in this study, with respect to direction are n_{TN} = 0.153, n_{RN} = 0.165 and n_{AN} = 0.168 [27].

Cube-shaped samples, with sides of about 4 mm length, were cut from the pressure tube. One side, with the surface normal aligned with either the Transverse, Radial, or Axial

directions of the tube, we refer to these surfaces as *TN*, *RN*, and *AN* planes respectively (Figure 4.3), was then mechanically ground with successively finer grit abrasive paper and finally chemically attack polishing to an average surface roughness of about ± 0.01 μm.

Initial yield stress, σ_{yield} (MPa)	**T= 25°C**	**T= 100°C**	**T= 200°C**	**T= 300°C**
$\sigma_{yield\ A}$	610	580	521	465
$\sigma_{yield\ R}$	675	641	573	507
$\sigma_{yield\ T}$	798	767	684	617

Table 4.1. List of yield stress values obtained from previously reported uniaxial compression tests on cylinders aligned along the axial (AN), radial (RN), and transverse (TN) directions of the extruded and cold-drawn Zr-2.5Nb pressure tube [28].

Spherical micro-indentation tests were performed on the polished surfaces using a NanoTest indentation testing platform (Micro Materials Ltd (Wrexham, UK)). Multiple indentation tests were performed with small, 40 μm diameter, and large, 200 μm diameter, spheres in order to study the effect of indentation depth, and indenter diameter, on the resulting σ_{avg} - ε_{avg} curve of the Zr-2.5% Nb material.

The large diameter spherical indentation tests were performed with a 200 μm diameter spherical sapphire indenter on the *TN*, *RN*, and *AN* planes of the pressure tube at temperature of 25, 100, 200, and 300°C. The elevated temperature indentation tests were performed with the indenter and the test sample heated by independently controlled heating stages to ensure that both were at the same temperature. The indentation tests were performed by applying increasing indentation force *F* at a constant rate of 20

mN/sec while simultaneously recording the indentation depth *h*. Indentations were made to depths of h_{max} = 4, 8, 12, 16, 20 and 24 μm after which *F* was reduced such that the initial slope *S* of the unloading curve could be determined (Figure 4.1). Eight indentations were performed at each value of h_{max} for each sample**.** The indentations were spaced a distance of 500 μm apart. After indentation testing, several of the indentations were observed with scanning electron microscopy to assess the extent of material pile-up at the edge of the indentation.

Spherical micro-indentation tests were also performed on the *TN*, *RN*, and *AN* planes of the pressure tube at 25^{o}C with a small, 40 μm diameter, diamond sphere at a constant loading rate of 5 mN/sec. These tests were performed to depths of h_{max} = 4.0 μm. Partial unloading were performed, at depths of *h* = 0.5, 1.0, 1.5, 2.0, 2.5, 3.0, and 3.5 μm during each indentation test to allow measurement of the unloading compliance *S* from which the indentation contact radius r_c , and hence σ_{avg} and ε_{avg}, could be calculated.

4.3. Results

Figure 4.4 depicts typical indentation force *F* versus depth *h* curves from spherical indentation tests performed, on the *AN*, *RN*, and *TN* planes of the pressure tube, with the small and the large diameter spherical indenters. For indentations performed with the large 200 μm diameter sphere (Figure 4.4(a)) a higher indentation force occurs, for a given value of *h*, when the indentation is made on the *TN* plane compared to the *RN* or *AN* planes of the pressure tube. This is consistent with the known mechanical anisotropy of the extruded and cold-drawn Zr-2.5%Nb pressure tube material which dictates that the yield stress in the transverse (circumferential) direction is significantly larger than in the axial or the radial directions of the tube [21-22, 25-32].

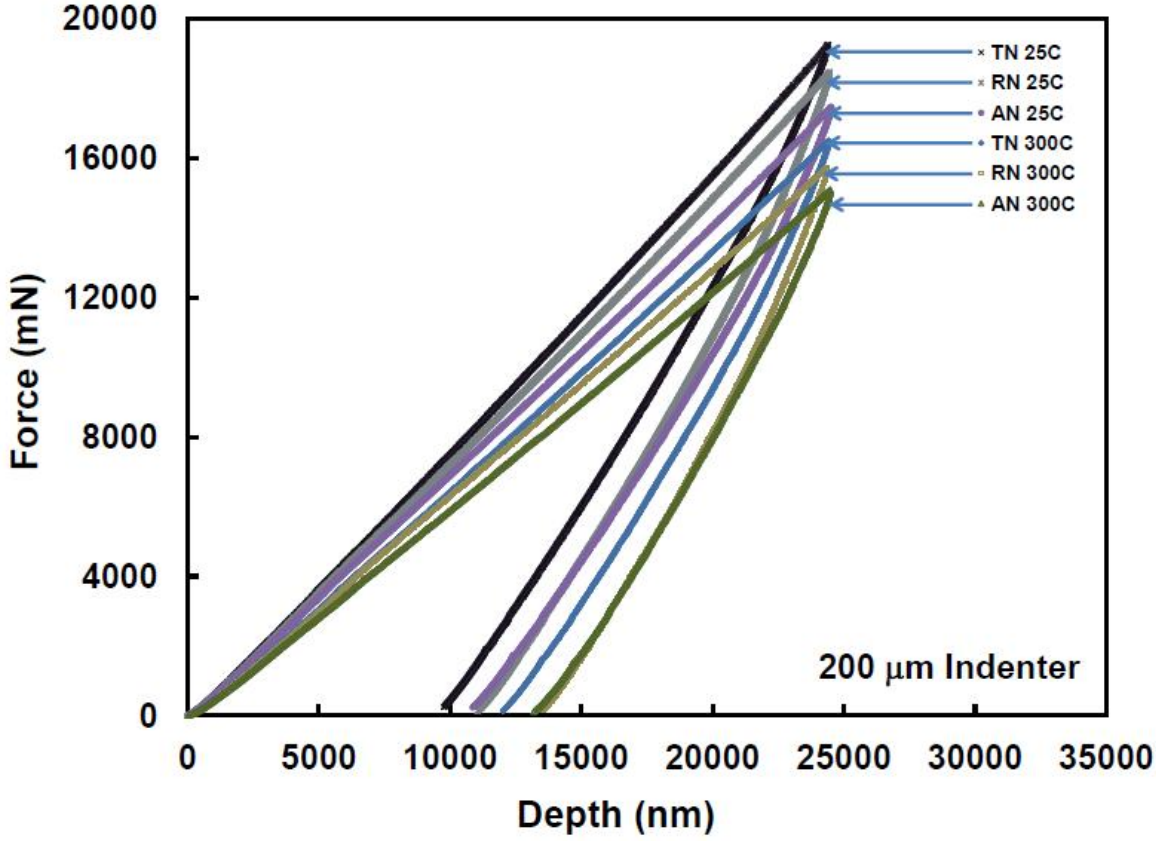
20000
16000
12000
8000
4000
0
Force (mN)
0
5000
10000
15000
20000
25000
30000
35000
Depth (nm)
TN 25C
RN 25C
AN 25C
TN 300C
RN 300C
AN 300C
200 μm Indenter

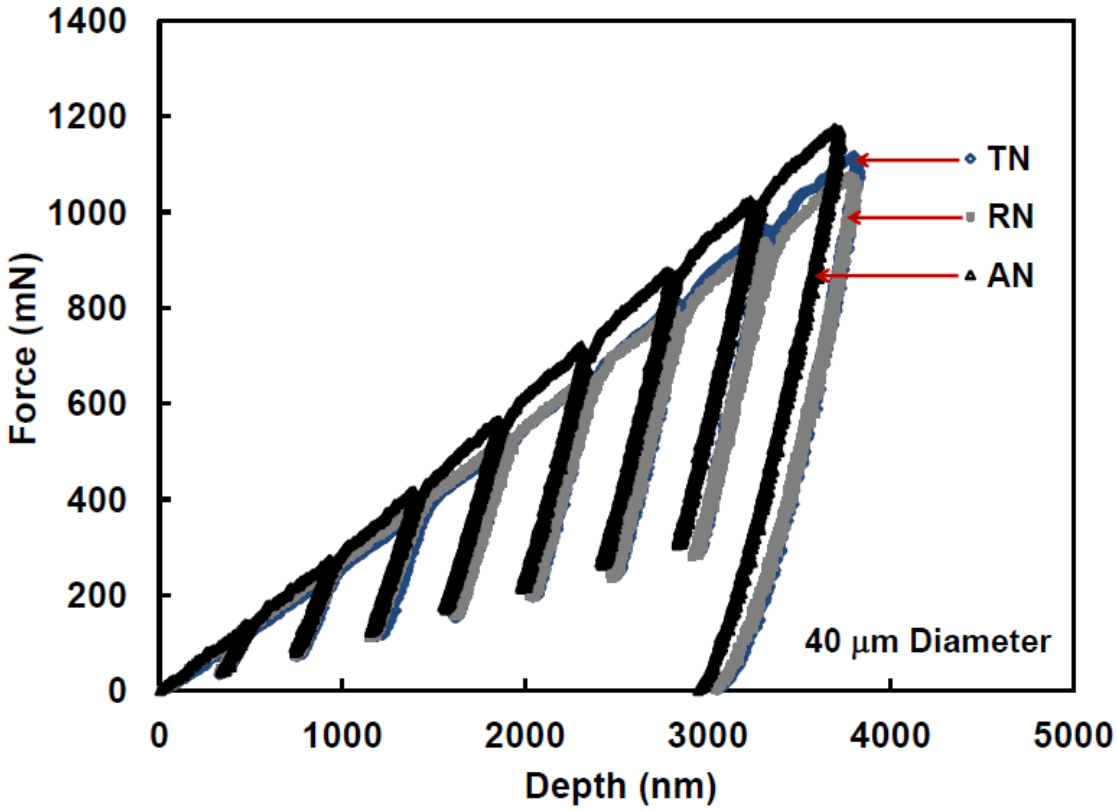

Figure 4.4. The indentation Force – Depth curve obtained from our spherical indentation experiments showing (a) single loading and unloading curve using the 200 μm diameter indenter at 25 °C and 300 °C on the orthogonal *AN*, *RN*, and *TN* planes and (b) a multiple loading and unloading curve using the 40 μm diameter indenter at 25 °C.

The indentation tests performed with the small 40 μm diameter sphere (Figure 4.4(b)) on the *AN* plane require more force, for a given value of *h*, compared to those made on the *RN* or *TN* planes of the pressure tube. This is inconsistent with both the data from the deeper indentations, performed with the larger diameter sphere and with the known mechanical anisotropy of the test material and will be discussed in Section 4.4.2.

Figure 4.5 shows SEM images of deep indentations made, with the 200 μm sphere, on the *AN*, *RN*, and *TN* planes of the Zr-2.5%Nb pressure tube material at 25^{o}C. While spherical indentation of a mechanically isotropic material will result in a circular residual

indentation, the indentations shown in this figure are slightly elongated in the planar direction of lowest σ_{yield}. This direction undergoes more material pile-up which causes the indentation to appear slightly elongated.

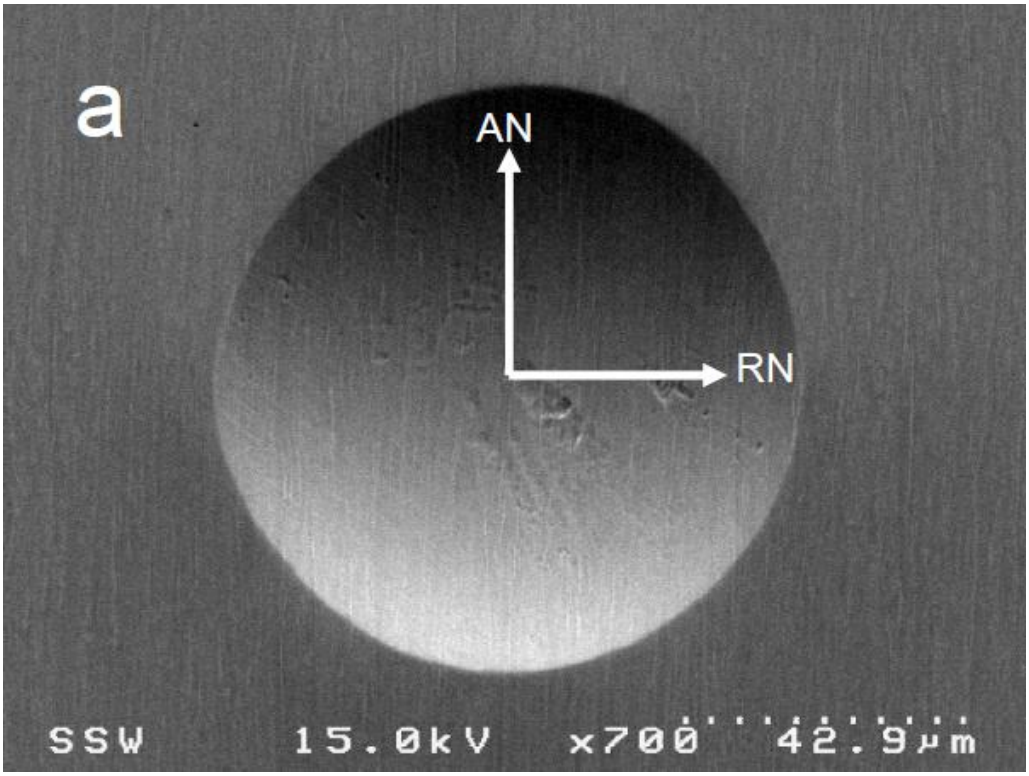

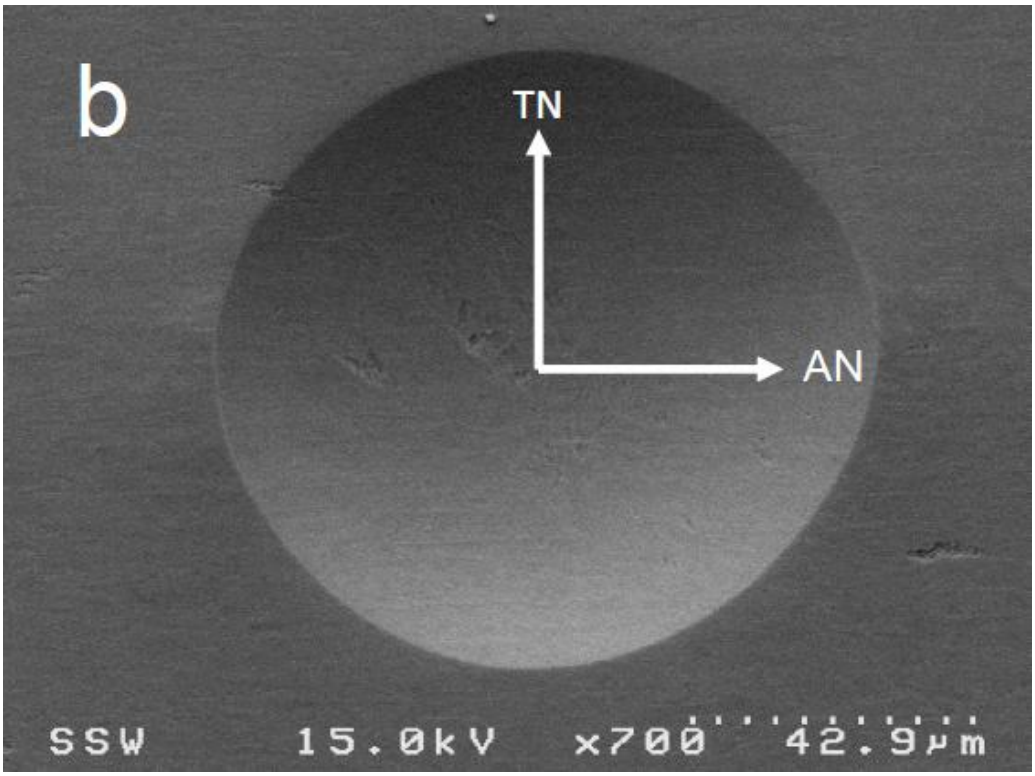
b
TN
AN
SSW
15.0kV
x700
42.9µm

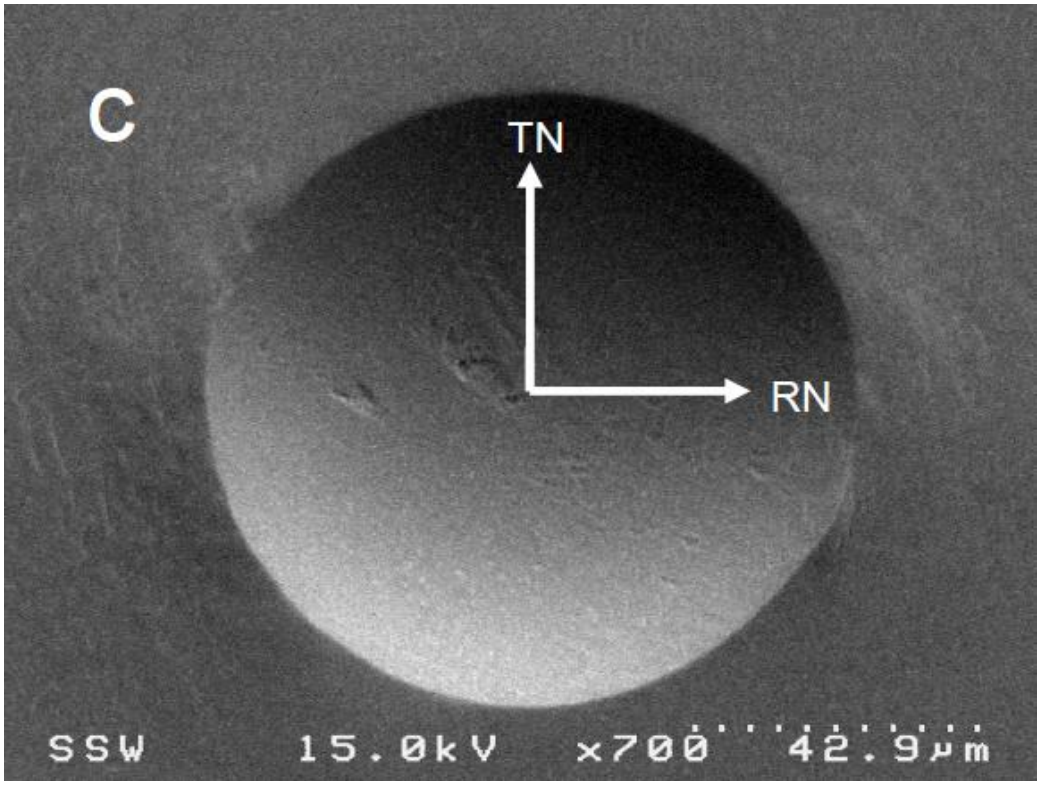
c
TN
RN
SSW
15.0kV
x700
42.9µm

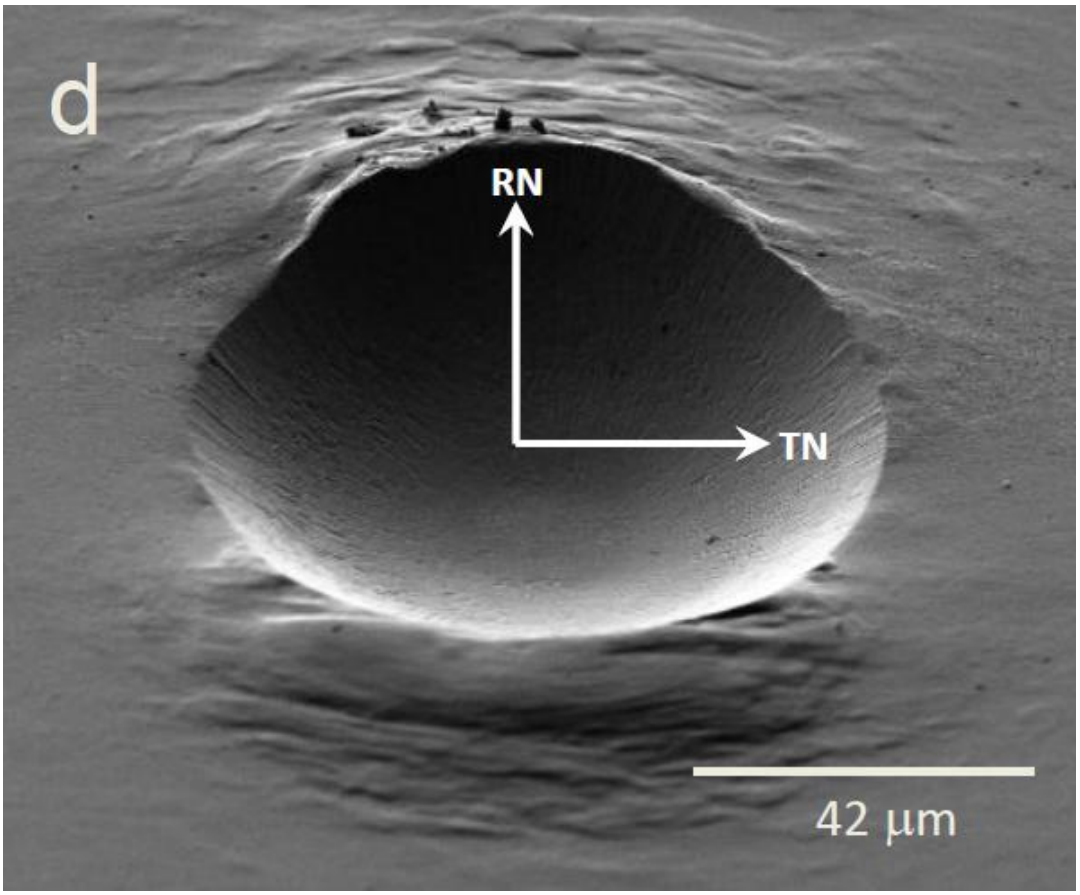

Figure 4.5. Scanning Electron Micrographs of spherical indentations made with the 200 μm diameter sphere at 25 °C to depths of 24 μm on the (a) *TN*, (b) *RN*, (c) *AN*, planes and (d) *AN* plane with the sample tilted at an angle of 54° to illustrate the extent of the anisotropic material pile up.

4.4. Discussion

The two primary objective of this research are: i) to develop a method of analysis by which the average flow stress σ_{avg} and the average plastic strain ε_{avg} can be obtained from the F versus h data obtained from spherical indentation of a mechanically anisotropic material and second, to determine if a significant indentation depth dependence is present in this method of analysis. We address these objectives in sequence.

4.4.1. Determining the average stress-strain curve:

For the large diameter spherical indentations P_m corresponding to the maximum indentation force (Fig. 4.4(a)) was determined using the value of r_c calculated with Eqs. 4.2(a,b), while for the small diameter indentations (Fig. 4.4(b)) r_c was calculated, using the same equation, at each partial unloading on the *F* versus *h* curves. The P_m data from the indentation tests performed with the large, 200 μm diameter, sphere on the *AN*, *RN*, and *TN* planes at temperature from 25°C to 300°C were used to determine the σ_{avg} of the Zr-2.5%Nb pressure tube material. During spherical indentation, plastic deformation must occur in the three orthogonal directions of the sample. If the material is mechanically anisotropic, as is the Zr-2.5%Nb material studied here, the lateral resistance to the indentation force exerted in each direction will vary in proportion to the yield stress in that direction. For this reason σ_{avg} given by Eqs. 4.3(a,b), which were derived to express the σ_{avg} for the elastic-plastic spherical indentation of an isotropic material, must be modified. We have done this by applying the Hill's anisotropy criterion [33] to determine the fractional constraint to the plastic deformation occurring from equal indentation stress in each of the orthogonal directions of the sample. For the case of Zr-2.5%Nb pressure tube material, with the three perpendicular planes of anisotropy corresponding to the axial, radial and transverse directions of the tube, subjected to a triaxial state of normal stress, the Hill's anisotropy criterion expresses the onset of plastic deformation to occur when [26]

$$\sigma_{AN_{yield}} = \sqrt{F\left(\sigma_{AN}-\sigma_{TN}\right)^2 + G\left(\sigma_{TN}-\sigma_{RN}\right)^2 + H\left(\sigma_{RN}-\sigma_{AN}\right)^2} \qquad (4.4)$$

By rearranging terms in Eq. (4.4), the ratios of the uniaxial yield stress in the *AN*, *RN*, and *TN* directions can be expressed in terms of anisotropy coefficients *F*, *G*, and *H* as:

$$\frac{\sigma_{RN_{yield}}}{\sigma_{AN_{yield}}} = \sqrt{\frac{1}{G+H}} \tag{4.5a}$$

$$\frac{\sigma_{TN_{yield}}}{\sigma_{AN_{yield}}} = \sqrt{\frac{1}{F+G}} \tag{4.5b}$$

In a recent study we performed uniaxial compression tests to measure $\sigma_{AN_{yield}}$, $\sigma_{RN\ yield}$, and $\sigma_{TN\ yield}$ of Zr-2.5%Nb pressure tube material at temperature from 25°C to 300°C and found that F = 0.38, G = 0.202 and H = 0.62 [28]. We observed that these coefficients were not strongly dependent upon temperature, over the range from 25°C to 300°C, or upon plastic strain. Substituting these values of *F, G*, and *H* into Eq. 4.5 gives the following ratios of the uniaxial yield stress of this pressure tube material:

$$\frac{\sigma_{RN_{yield}}}{\sigma_{AN_{yield}}} = 1.10 \tag{4.6a}$$

$$\frac{\sigma_{TN_{yield}}}{\sigma_{AN_{yield}}} = 1.31 \tag{4.6b}$$

These stress ratios can be used to adjust σ_{yield} in Eq. (4.3c) to approximately account for the fact that the indentation is being performed on a mechanically anisotropic material. Consider, for example, an indentation made on the *AN* plane of the pressure tube. The indented material deforms plastically in the axial direction of indentation but must also deform laterally in plane that includes the radial and the transverse directions of the tube. We can estimate that the fractional constraint to the axial deformation from deformation in the radial and transverse directions is proportional to the uniaxial yield stress ratios in each of these directions; thus, for this indentation, the resistance to the axial deformation will be proportional to $\sigma_{AN_{yield}}$ while, according to Eqs. (4.6(a, b)), the lateral resistance from the radial direction will be proportional to $\sigma_{RN_{yield}} = 1.10\sigma_{AN\ yield}$ while that in the

transverse direction will be proportional to $\sigma_{TN_{yield}} = 1.31\sigma_{AN_{yield}}$. The total fractional resistance from each direction in constraining the indentation deformation can then be determined by dividing the stress ratio in each direction by the sum of the stress ratios in all three directions. Referring to the resulting yield stress as the equivalent yield stress $\bar{\sigma}_{yield}$, we can define the fractional contribution to $\bar{\sigma}_{yield}$ resulting from deformation in the axial direction as:

$$\bar{\sigma}_{AN_{yield}} = \frac{1.0}{1.31+1.10+1.0}\sigma_{AN_{yield}} = 0.293\sigma_{AN_{yield}} \tag{4.7a}$$

similarly, the contribution from lateral deformation in the radial direction would be

$$\bar{\sigma}_{RN_{yield}} = \frac{1.10}{1.31+1.10+1.0}\sigma_{RN_{yield}} = 0.323\sigma_{RN_{yield}} \tag{4.7b}$$

while the contribution from lateral deformation in the transverse direction would be

$$\bar{\sigma}_{TN_{yield}} = \frac{1.31}{1.31+1.10+1.0}\sigma_{TN_{yield}} = 0.384\sigma_{TN_{yield}} \tag{4.7c}$$

The total equivalent yield stress $\bar{\sigma}_{yield}$ can then be calculated by combining these fractional contributions as

$$\bar{\sigma}_{yield} = 0.293\sigma_{AN_{yield}} + 0.323\sigma_{RN_{yield}} + 0.384\sigma_{TN_{yield}} \tag{4.7d}$$

Once $\bar{\sigma}_{yield}$ has been determined it can be substituted in Eq. (4.3(c)) to determine the dimensionless material parameter ϕ, the geometrical constraint factor ψ, and then the average indentation stress σ_{avg}.

Figures 4.6(a-d) shows the resulting σ_{avg} - ε_{avg} plots for indentation tests performed, with a 200 μm diameter sphere, on the Zr-2.5%Nb material at temperature from 25^{o}C to

300°C. The resulting flow curves are very similar to those obtained from conventional uniaxial compression and tension tests performed, on the same material, in the same direction and temperature.

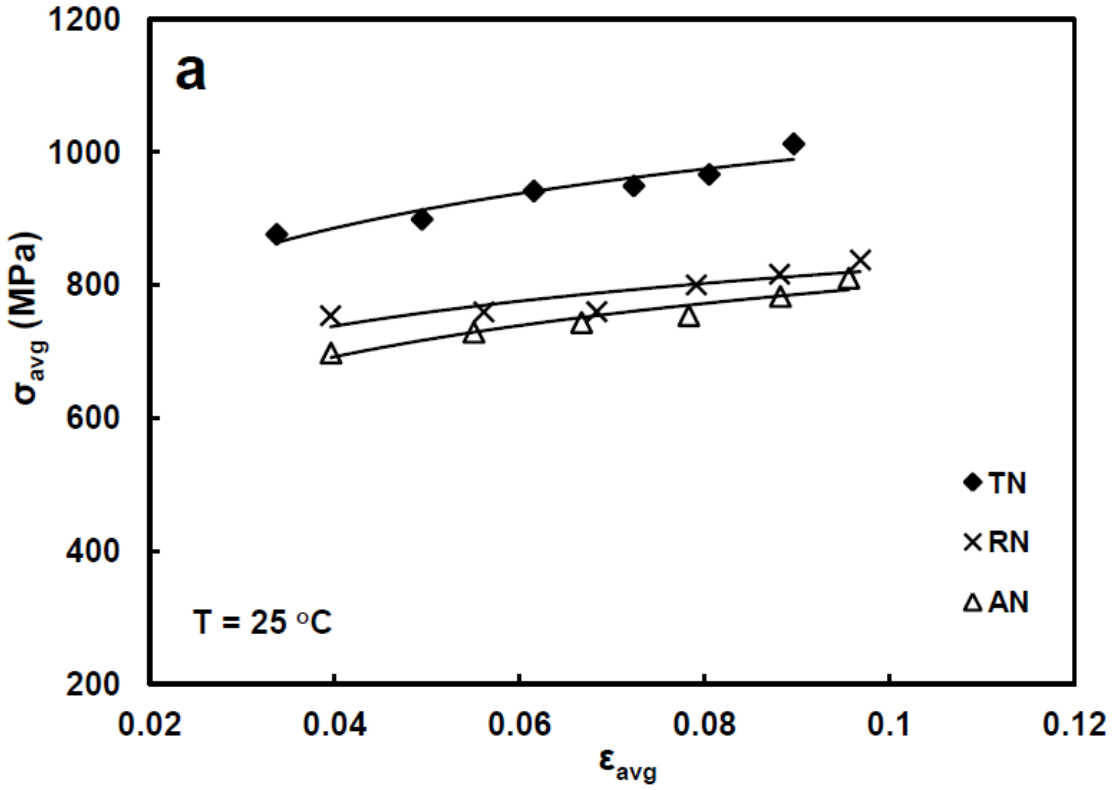

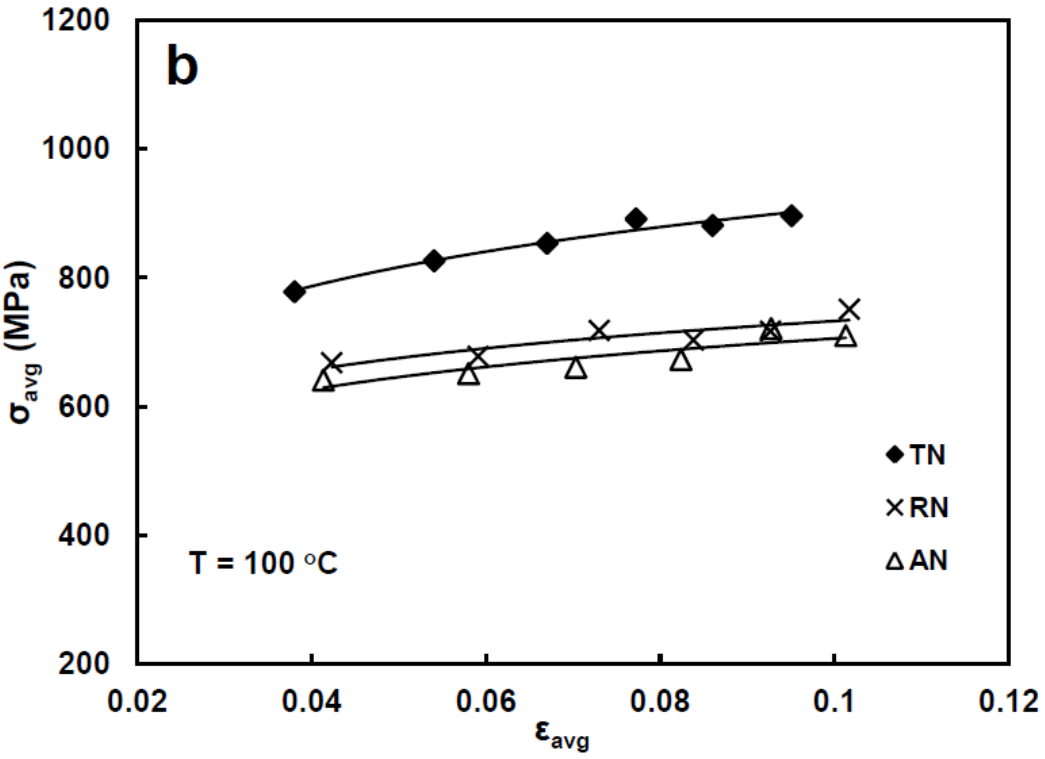
b
1200
1000
800
600
400
200
σavg (MPa)
0.02
0.04
0.06
0.08
0.1
0.12
εavg
T = 100 °C
TN
RN
AN

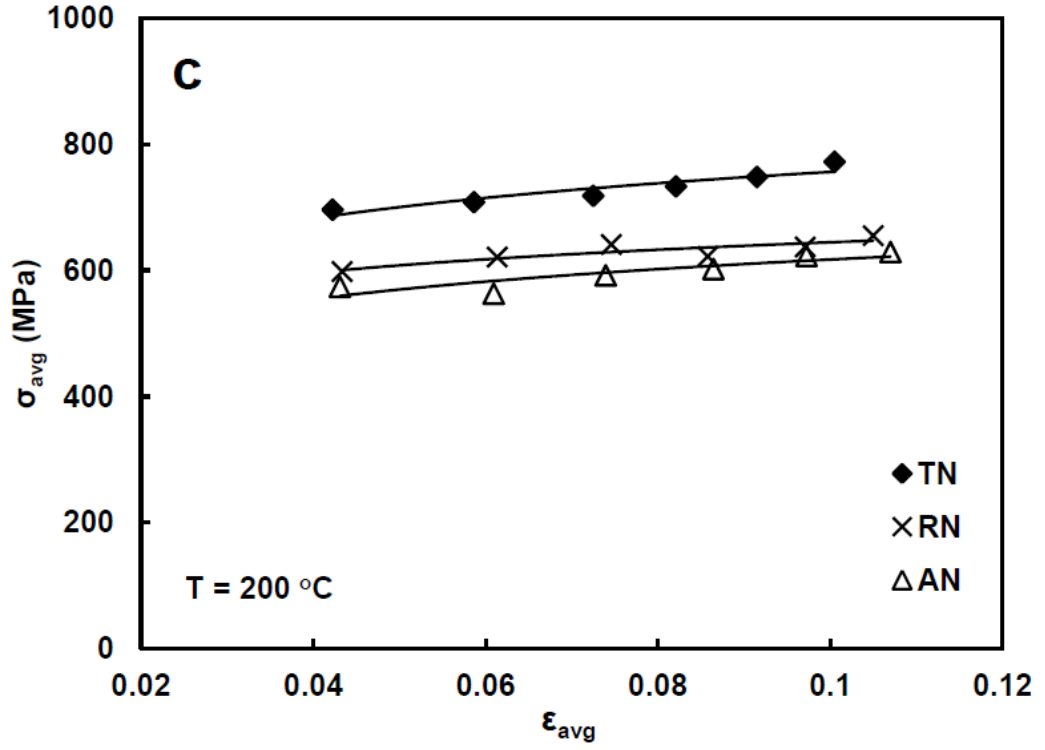
c
1000
800
600
400
200
0
σavg (MPa)
0.02
0.04
0.06
0.08
0.1
0.12
εavg
T = 200 °C
TN
RN
AN

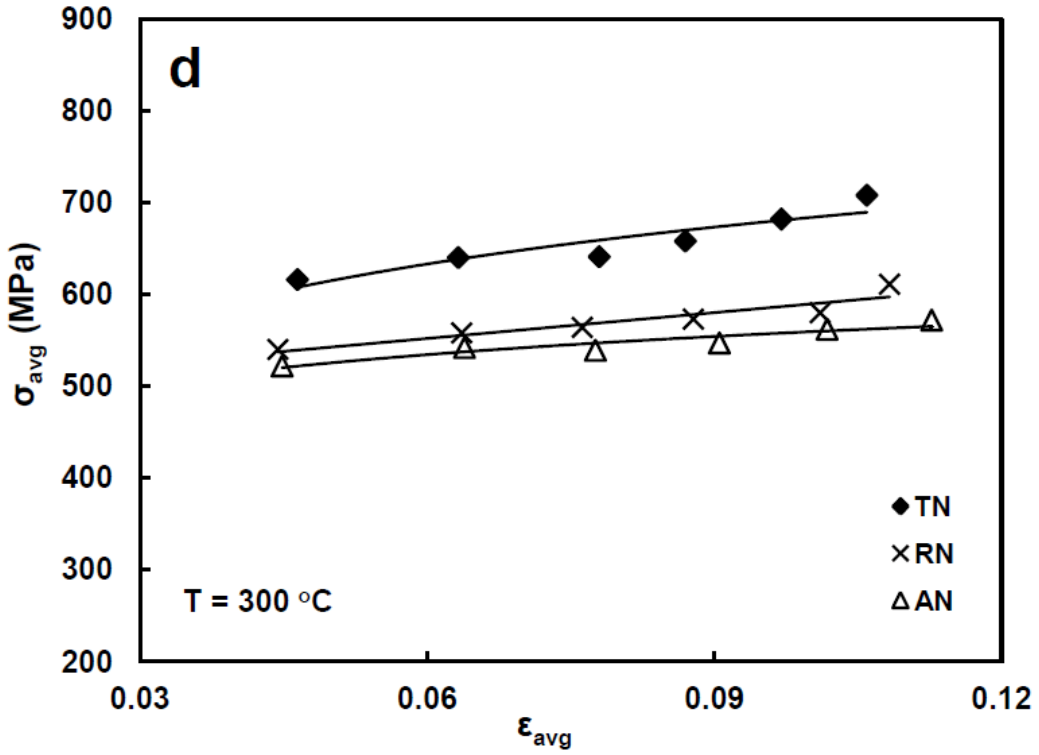

Figure 4.6. Plots of σ_{avg} versus ε_{avg} from spherical indentations performed on the *TN*, *RN*, and *AN* planes of the Zr-2.5%Nb pressure tube at (a) 25^{o}C, (b) 100^{o}C, (c) 200^{o}C, and (d) 300^{o}C.

Figures 4.7(a-c) shows the σ_{avg} - ε_{avg} curves from our spherical indentation tests performed at 300^{o}C in the *TN*, *RN* and *AN* directions. These figures include additional σ_{avg} - ε_{avg} data from previously reported uniaxial tension and compression tests performed on the Zr-2.5%Nb material [28]. The close correspondence in the σ_{avg} - ε_{avg} curves with those obtained from conventional uniaxial stress tests validates the method adopted here to determine σ_{avg} - ε_{avg} from the spherical indentation force – depth data.

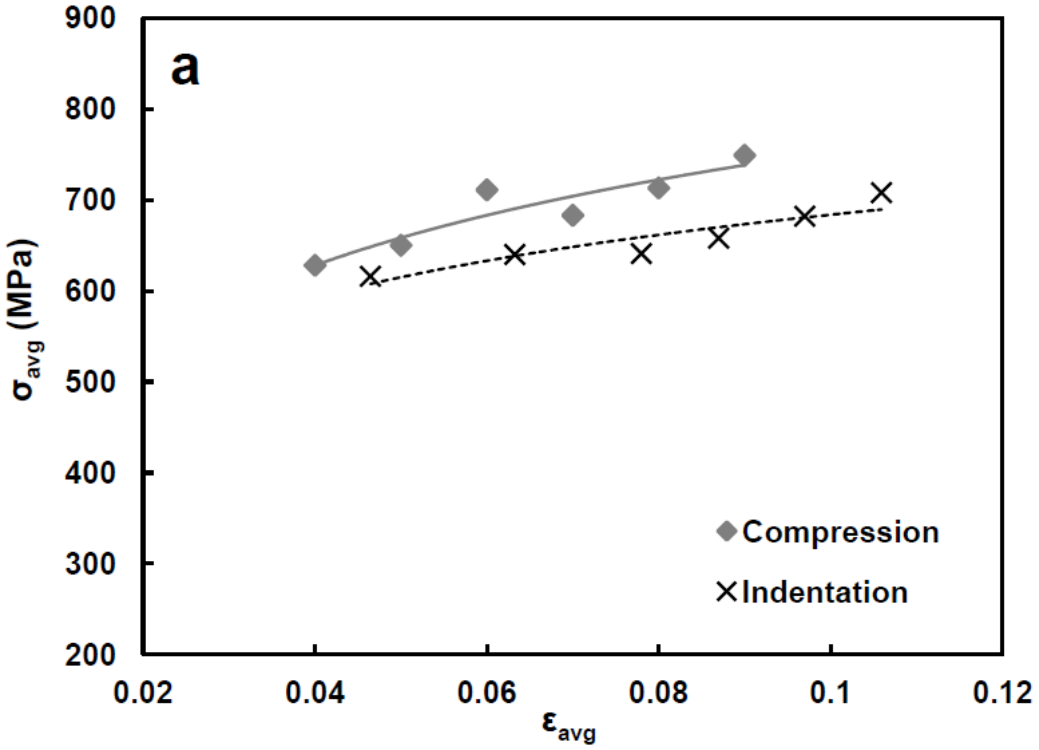
a
900
800
700
600
500
400
300
200
0.02
0.04
0.06
0.08
0.1
0.12
σavg (MPa)
εavg
Compression
Indentation

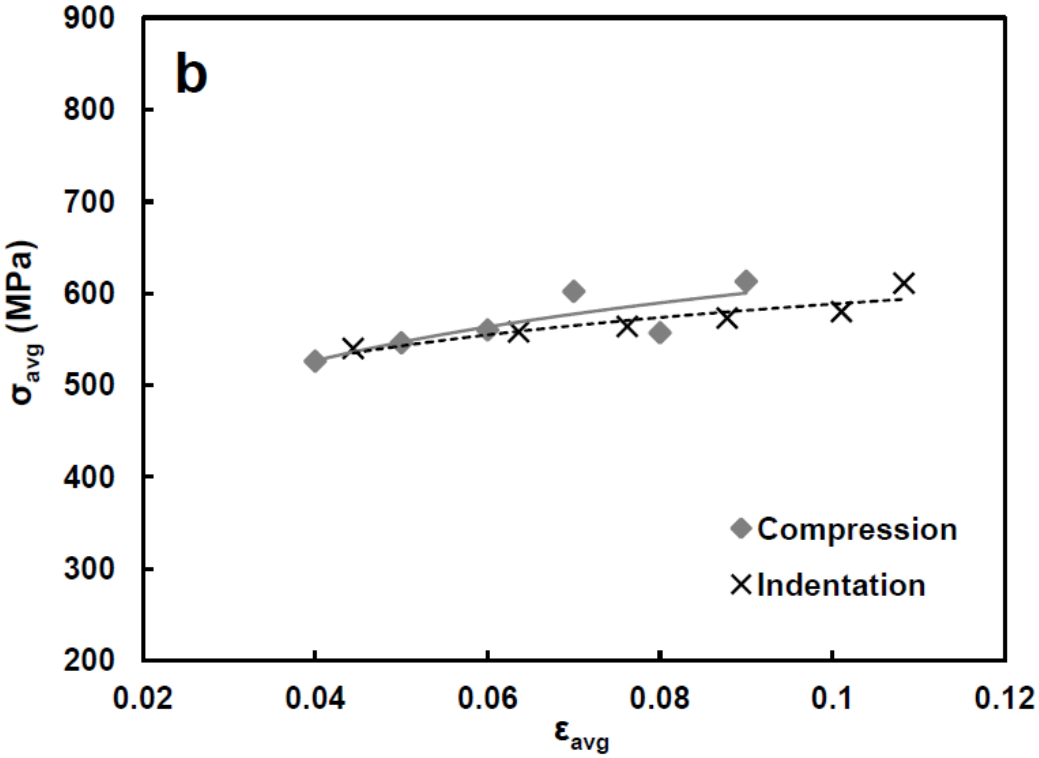
b
900
800
700
600
500
400
300
200
0.02
0.04
0.06
0.08
0.1
0.12
σavg (MPa)
εavg
Compression
Indentation

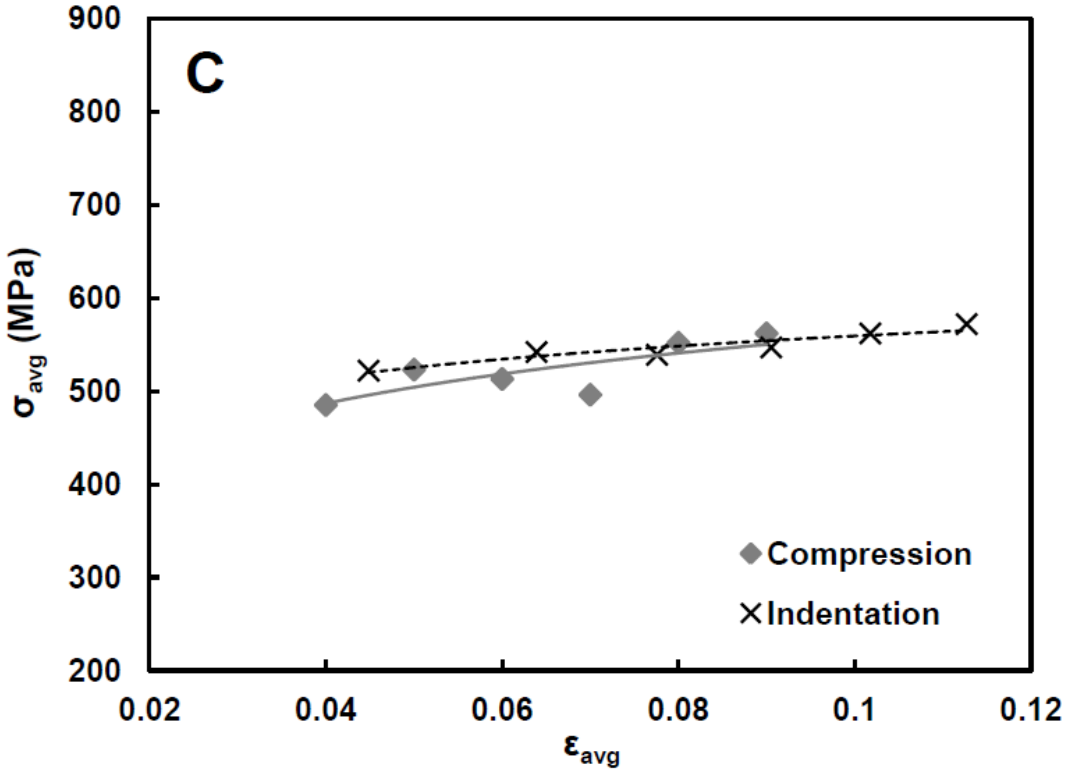

Figure 4.7. Plots of σ_{avg} versus ε_{avg} from spherical indentation tests and uniaxial compression test data [28] performed on the (a) *TN*, (b) *RN*, and (c) *AN* planes of the Zr-2.5%Nb pressure tube at 300^{o}C.

4.4.2. The indentation depth dependence of the average stress-strain flow curve

It has been observed in most metals that the mechanical strength, either the uniaxial flow stress or the indentation hardness, increases with decreasing sample size less than about several micrometers [22, 25, 34-37]. This type of length-scale dependence was reported for Zr-2.5%Nb material by Bose et al [25] who observed that the indentation stress increased significantly for indentation depths less than about 1 μm. Comparison of the σ_{avg}-ε_{avg} plots from the deep, large diameter, spherical indentations (Fig. 4.6(a-d)) with those from the shallow, small diameter, spherical indentations (Fig. 4.8) indicates that there is a significantly different stress-strain response when the indentation depth is less than 4 μm despite the fact that, because the diameter of the indenting sphere was different

in both cases, the magnitude of ε_{avg} is the same for both the deep and the shallow indentations.

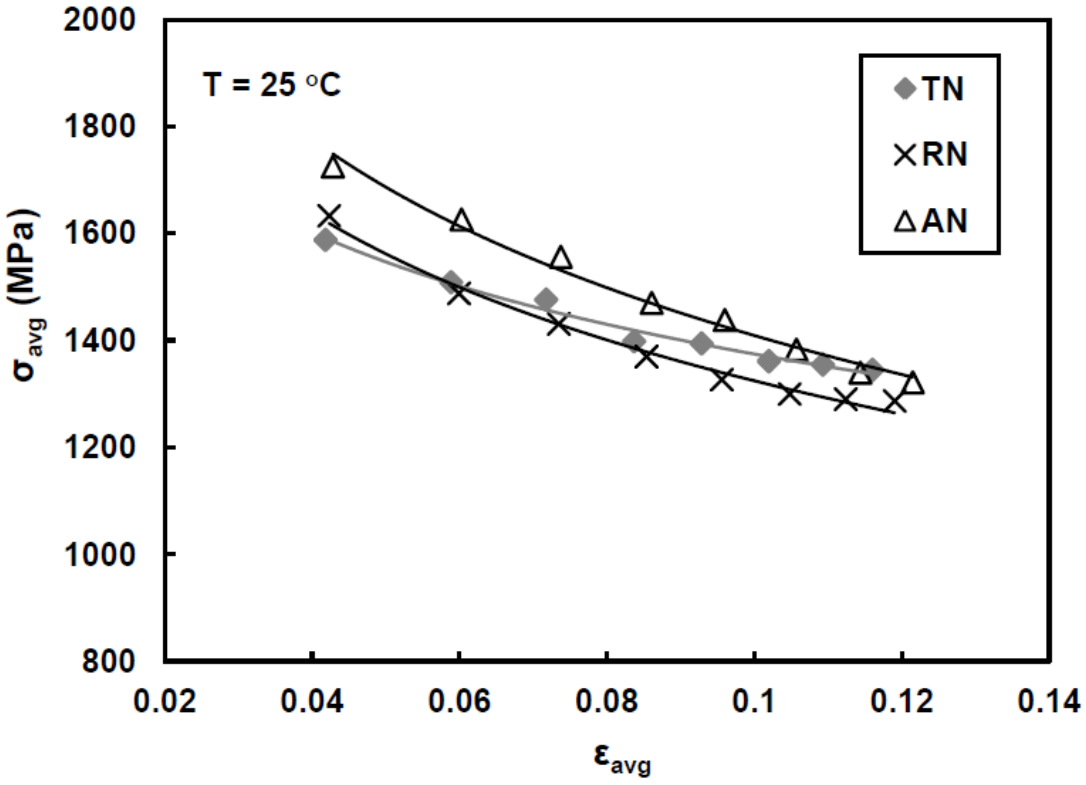

Figure 4.8. Plots of σ_{avg} versus ε_{avg} from spherical indentation tests performed on the *TN*, *RN*, and *AN* planes of the Zr-2.5%Nb pressure tube at 25^{o}C using the 40 μm diameter indenter.

One clear difference is that, for the small diameter spherical indentations σ_{avg} is largest, for a given ε_{avg}, for indentations made on the *AN* plane. In the case of the large diameter indentations σ_{avg} is largest, for indentations made on the *TN* direction. This suggests that the local plastic strain distribution around the spherical indentation is dependent upon indentation depth and possibly on an increase in the diameter of the indenter. Since the

yield stress is greatest in the transverse followed by the radial direction of the pressure tube (Eqs. 4.6(a,b)), it would suggest that the proportion of lateral-to-axial plastic strain during spherical indentation changes with indentation depth and/or with an increase in the diameter of the indenter. When an indentation is made on the *AN* plane, the lateral strain must occur by deformation in the transverse and radial directions: the two directions with the highest yield stress. If the lateral plastic strain is quite large relative to the axial plastic strain and is in fact larger than that during the deeper, large diameter, indentations (Fig. 4.6(a)), then the increased yield stress in the transverse and radial directions would result in σ_{avg} being largest for indentations made on the *AN* plane.

To assess the effect of increased σ_{yield} of the indented material when $h < 4.0$ μm we use the indentation stress σ_{ind} versus depth plots reported by Bose et al, using a Berkovich pyramidal indenter [25], to estimate, as $\sigma_{yield} \approx \sigma_{ind}/3$ [1], the uniaxial yield stress of the Zr-2.5%Nb pressure tube material corresponding to depths less than 4.0 μm. Figure 4.9 indicates that when the indentation depths are less than several micrometers both σ_{ind} obtained from pyramidal indentation tests and σ_{avg} obtained from spherical indentation are heavily influenced by the length-scale dependence of the yield strength of the material and this dependence may overshadow its dependence upon ε_{avg}. This may explain the unusual profile of the σ_{avg} versus ε_{avg} curves shown, for the shallow, small diameter, spherical indentations in Fig. 4.8.

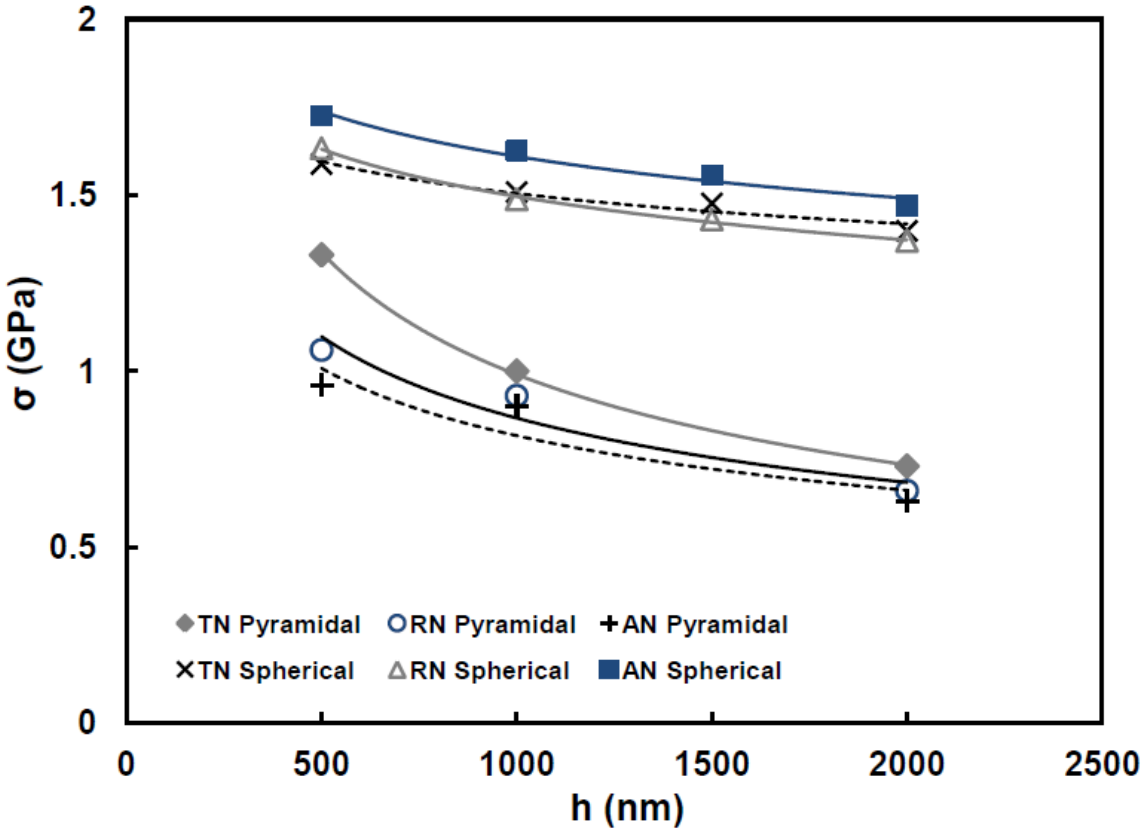

Figure 4.9. Plot of σ_{yield} versus indentation depth. σ_{yield} was calculated from σ_{ind} data obtained from previously reported nano-indentation tests performed on Zr-2.5%Nb using a Berkovic pyramidal indenter [25]. Superimposed upon these data are σ_{avg} versus indentation depth data from the spherical indentations performed with the small 40 μm diameter sphere. Both σ_{yield} and σ_{avg} show similar indentation depth dependence.

4.5. Conclusions

In this paper we developed a method of analysis by which the average flow stress σ_{avg} and the average plastic strain ε_{avg} are obtained from the F - h data from spherical indentation tests performed on a mechanically anisotropic material. Our analysis is based upon spherical indentation tests performed on the mechanically anisotropic Zr-2.5%Nb CANDU pressure tube material over the range of temperature from 25°C to 300°C. We

performed spherical indentation tests, at each temperature, on the Axial Normal (*AN*), Radial Normal (*RN*), and Transverse Normal (*TN*) planes of the tube. The *F* - *h* data were used, along with known values of the Hill's anisotropy coefficients and the strain hardening coefficients for the test material, to calculate σ_{avg} and ε_{avg} using the equations developed to describe the spherical indentation of an isotropic material and a modified, equivalent σ_{yield}.

The resulting σ_{avg} - ε_{avg} plots for indentation tests performed, with a 200 μm diameter sphere, at temperature from 25°C to 300°C indicate that this method of analysis results in the data from spherical indentations performed on the *AN*, *RN*, and *TN* planes bearing a close correspondence to the flow curves obtained from uniaxial stress tests. This confirms that this analysis can serve as a reliable alternative to conventional tensile tests to obtain flow stress – plastic strain curves from small samples of mechanically anisotropic material with minimal sample preparation. This is a potentially very useful test method for a variety of applications, such as in-cell mechanical testing of radioactive nuclear materials.

Spherical micro-indentation tests were performed with large, 200 μm diameter, and with small, 40 μm diameter, spheres to assess the indentation depth limitations of the proposed data analysis technique. Comparison of the σ_{avg} - ε_{avg} plots from the deep, large diameter, spherical indentations with those from the shallow, small diameter, indentations indicates that there is a significantly different stress-strain response when the indentation depth is less than 4 μm. One clear difference is that, for the small diameter spherical indentations, σ_{avg} is largest, for a given ε_{avg}, for indentations made on the *AN* plane while σ_{avg} is largest, for indentations made on the *TN* plane when deep indentations are made with the large diameter sphere. This suggests that the local plastic strain distribution around the spherical indentation is dependent upon indentation depth and possibly also with increasing indenter diameter.

Plots of σ_{avg} - ε_{avg} curve obtained from the shallow, small diameter, indentations indicate that when the indentation depths is less than several micrometers the calculated σ_{avg} is heavily influenced by the depth dependence of the yield strength of the material and this may overshadow its dependence upon ε_{avg}.

Acknowledgements

The authors wish to thank the Natural Science and Engineering Research Council of Canada (NSERC) and the University Network of Excellence in Nuclear Engineering (UNENE) who provided financial support for this research. Finally, we offer a special note of thanks to Drs. B. Leitch and S. St. Lawrence of the Atomic Energy of Canada Ltd (*Chalk River Laboratories)* for providing the Zr-2.5%Nb pressure tube material used in this study.

References

[1] D. Tabor, “The Hardness of Metals” (Clarendon Press, Oxford, UK, 1951) p. 44-83.

[2] J.P. Weiler, J.T. Wood, R.J. Klassen, R. Berkmortel, G. Wang, J. Mater. Sc. 40 (2005) 5999.

[3] S.-H. Kim, M.-K, Baik, D. Kwon, J. Eng. Mater. 127 (2005) 265.

[4] J. –H. Ahn, D. Kwon, J. Mater. Res. 16 (2001) 3170.

[5] M. Beghini, L. Bertini, V. Fontanari, Intern. J. Comp. Appl. Tech. 15 (2002) 168.

[6] H.A. Francis, J. Eng. Mater. and Tech. 76 (1976) 272.

[7] S.-H. Kim, B.W. Lee, Y. Choi, D. Kwon, J. Mater. Sc. & Eng. A 415 (2006) 59.

[8] F. M. Haggag, R. K. Nanstad, R.K. Hutton, J.T. Thomas, R.L. Swain, ASTM 1092 (1990) 188.

[9] A. Bolshakov, G.M. Pharr, J. Mater. Res. 13 (1998) 1049.

[10] J. Acala, A.E. Giannakopoulos, S. Suresh, J. Mater. Res. 13 (1998) 1390.

[11] Y. J. Park, G.M. Pharr, Thin Solid Films 447 (2004) 246.

[12] N. Ogasawara, N. Chiba, X. Chen, Mech. Mater. 41 (2009) 1025.

[13] B. Taljat, G.M. Pharr, Int. J. Sol. & Struc. 41 (2004) 3891.

[14] M. Bocciarelli, G. Bolzon, G. Maier, Mech. Mater. 37 (2005) 855.

[15] T. Nakamura, Y. Gu, Mech Mater. 39 (2007) 340.

[16] A. Yonezu, K. Yoneda, H. Hirakata, M. Sakihara, K. Minoshima, Mater. Sc. & Eng. A 527 (2010) 7646.

[17] R. Hill, B. Storakers, A.B. Zdunek, Proc. R. Soc. London A, 423 (1989) 301.

[18] W.C. Oliver, G.M. Pharr, J. Mater. Res. 7 (1992) 1564.

[19] K.L. Johnson, J. Mech. Phys. Sol. 18 (1970) 115.

[20] S.D. Mesarovic, N.A. Fleck, Proc. Royal Soc. Lond., series A 455 (1999) 2707.

[21] N. Christodoulou, P.A. Turner, C.N. Tomé, C.K. Chow, R.J. Klassen, Metall. Mater. Trans. A 33 (2002) 1103.

[22] B. Bose, R.J. Klassen, J. Nucl. Mater. 399 (2010) 32.

[23] V. Perovic, G.C. Weatherly, R.G. Fleck, Can. Metall. Quart. 24 (1985) 253.

[24] V. Perovic, G.C. Weatherly, L.M. Brown, G. R. Purdy, R. G. Fleck, R.A. Holt, J. Nucl. Mater. 205 (1993) 251.

[25] B. Bose, R.J. Klassen, J. Nucl. Mater. 405 (2010) 138.

[26] N. Christodoulou, P.A.Turner, E.T.C. Ho, C.K. Chow, M.R. Levi, Metall. Mater. Trans. A 31A (2000) 409.

[27] R.O. Oviasuyi, R.J. Klassen, J. Nucl. Mater. 421 (2012) 54.

[28] R.O. Oviasuyi, R.J. Klassen, Manuscript submitted for publication at J. Nucl. Mater. 2012.

[29] X. Wei, J.R. Theaker, M. Griffiths, Zirconium in the Nuclear industry, in: 15th International Symposium of ASTM, STP 1505, 2009, p. 583.

[30] B.S. Rodchenkov, A.N. Semenov, Nucl. Eng. Des. 235 (2005) 2009.

[31] W.J. Langford, L.E.J. Mooder, J. Nucl. Mater. 39 (1971) 292.

[32] S.S. Kim, Y.S. Kim, S.C. Kwon, S.B. Ahn, K. N. Choo, Transactions of the 15th International Conference on: Struc. Mech. React. Technol. (SMiRT-15) 1999, p. X-263.

[33] R. Hill, Proc. Royal Soc. Lond., series A 193 (1948) 1033.

[34] V. Bhakhri, R.J. Klassen, J. Mater. Sci. 41 (2006) 2249.

[35] V. Bhakhri, R.J. Klassen, J. Mater. Sci. 41 (2006) 2259.

[36] V. Bhakhri, R.J. Klassen. Scr. Mater. 55 (2006) 395.

[37] B.J. Diak, S. Saimoto, Mater. Sci. Eng. A 234-236 (1997) 1015.

Chapter 5

5. Anisotropic deformation of Zr ion irradiated Zr-2.5%Nb micro-pillars[6]

In this chapter micro-pillars of 5 μm diameter and 5 μm height were made from textured Zr-2.5%Nb pressure tube material and were irradiated with 8.5 MeV Zr^+ to simulate neutron irradiation. The yield stress, strain hardening exponent, and degree of strain localization of the micro-pillars when tested at 25°C increased with ion irradiation and the extent of increase was largest in directions containing low (0001) basal pole fraction. This suggests that Zr^+ irradiation inhibits prismatic dislocation slip more than pyramidal slip in this material.

5.1. Introduction

Extruded and cold-drawn Zr–2.5%Nb pressure tubes, used in CANDU nuclear reactors, are mechanically anisotropic due to their strongly textured hcp crystal structure. While the anisotropic yield stress of these tubes in the non-irradiated condition is relatively well characterized, the mechanical anisotropy in the neutron irradiated condition is much less understood [1-5]. Neutron irradiation induces the nucleation of point defects and small dislocation loops, which is known to raise the yield stress by impeding dislocation glide. The limited data from mechanical tests, mostly of the micro-indentation type, performed upon neutron- and ion- irradiated zirconium alloys has demonstrated that the anisotropy of the yield stress is reduced by neutron and ion irradiation [6-10]. It has been proposed that this is the result of irradiation damage having a larger effect on impeding prismatic $\{10\bar{1}0\}\langle\bar{1}2\bar{1}0\rangle$ dislocation glide, which is the primary mode of axial and radial deformation, than on impeding pyramidal $\{10\bar{1}1\}\langle\bar{1}\,\bar{1}23\rangle$ dislocation glide, the primary mode of circumferential deformation of these textured tubes [10-13]. In view of the uncertainty of the actual applied stress and strain state during micro-indentation we have, in this study, used uniaxial compression of cylindrical micro-pillars to assess the effect of

[6] The manuscript in this chapter is an expanded version of the one published in the Journal of Nuclear Materials [R.O. Oviasuyi, R.J. Klassen, J. Jucl. Mater. 421 (2012) 54].

irradiation on the anisotropic stress-strain response of extruded and cold-drawn Zr–2.5%Nb pressure tubes.

Micro-pillar compression testing is commonly used to study the mechanical properties of small volumes of material [14-20]. The use of micro-pillars with diameters less than several micrometers allows one to study the effect of high levels of self-similar ion irradiation damage on the mechanical response of a material. Monte-Carlo simulations (performed with SRIM free-access software) indicate that the penetration depth of 8.5 MeV Zr^{+} ions is sufficient to invoke a significant degree of irradiation hardening through the entire volume of a 5 μm diameter cylindrical pillar of Zr-2.5%Nb.

5.2. Experimental procedure

The extruded and 22% cold-drawn Zr–2.5%Nb CANDU pressure tube material used in this study was supplied by the Atomic Energy of Canada Ltd. The material is strongly textured with the majority of the hcp α-phase grains aligned with their (0001) basal plane normal in the transverse (circumferential) direction of the tube [2].

Cubic samples, each side several millimeters in length, were cut from the as-received pressure tube. The samples were arranged into three groups; each group having one polished side normal to either the axial, radial, or transverse directions of the pressure tube. The polished side was prepared by first mechanical grinding then mechanical/chemical polishing. The final polishing stage consisted of chemical attack polishing in a slurry of 91% H_2O, 8% HNO_3, 1% HF followed by mechanical polishing with a 0.05 μm Al_2O_3 abrasive compound.

Micro-pillars of 5 μm diameter and height were fabricated from the polished surfaces by Focused Ion Beam (FIB) milling with a LEO (Zeiss) 1540XB FIB/SEM located at the Western Nanofabrication facility of the University of Western Ontario (London, Ontario Canada). For each micro-pillar, a 10 nA Ga^{+} beam was used to create a 5 μm deep concentric circle of 60 μm diameter with an 8 μm diameter, 5 μm high, pillar remaining at the center. The large diameter circle was necessary to ensure that the flat punch indenter, used to perform the subsequent mechanical testing, did not contact the

surrounding material while compressing the micro-pillar. A 200 pA Ga^+ beam was then used to finely polish the micro-pillar thereby reducing its diameter to approximately 5 μm (Figure 5.1). Four micro-pillars, each in their own 60 μm diameter circle and separated by a distance between 200 and 300 μm, were made on each group of three polished sample surfaces aligned normal to the radial, axial, and transverse directions of the pressure tube.

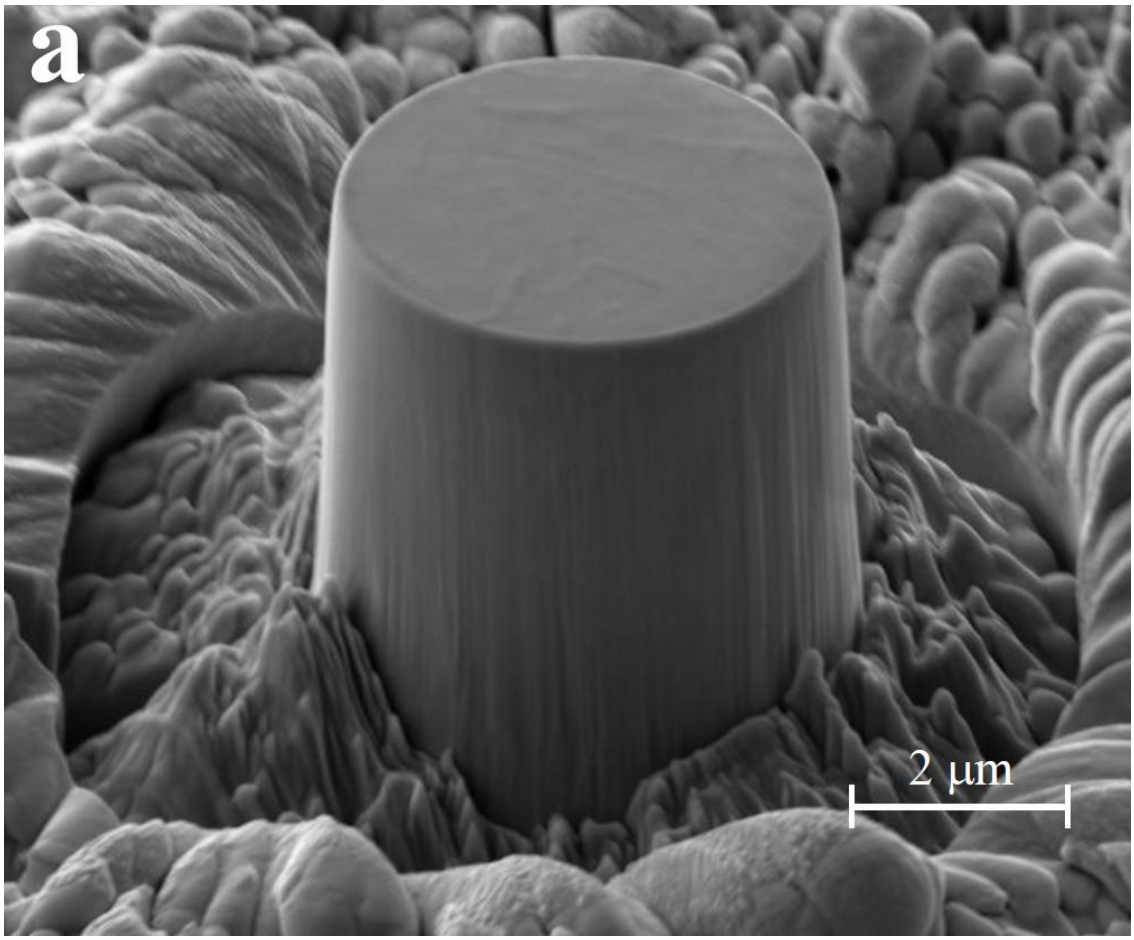

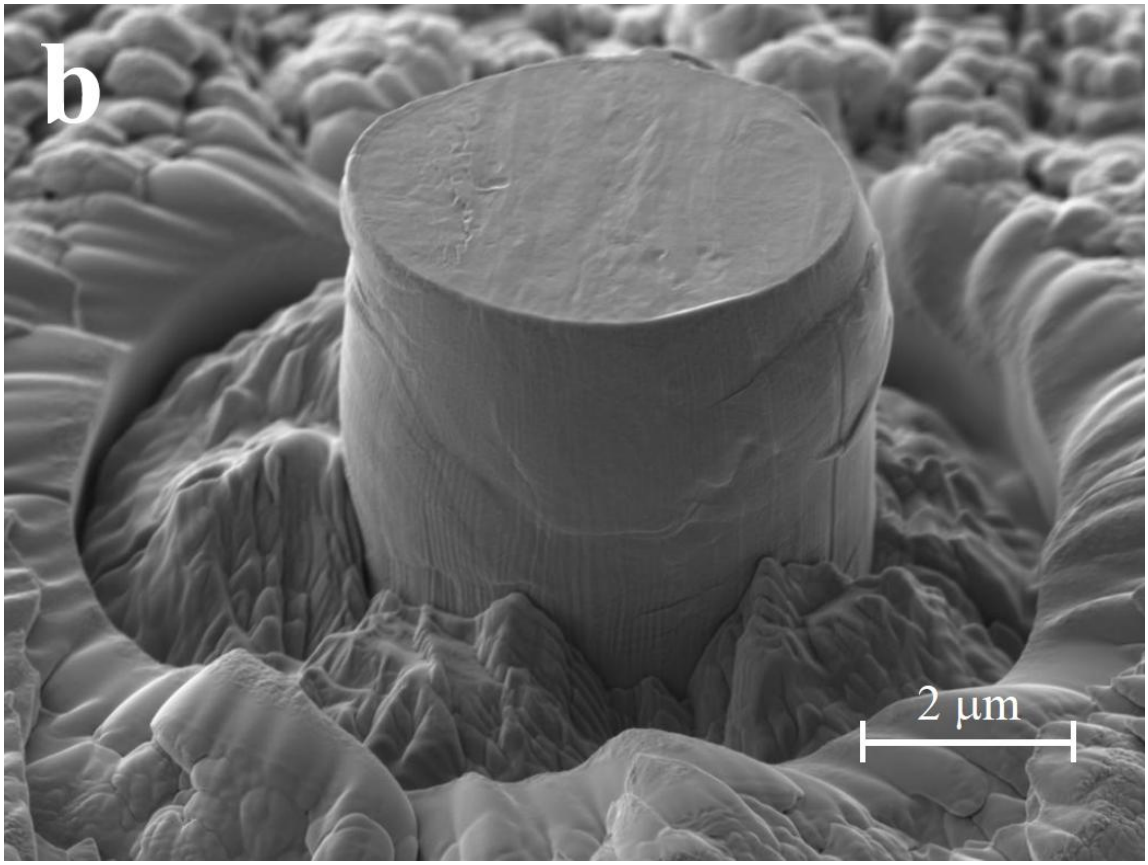
b
2 μm

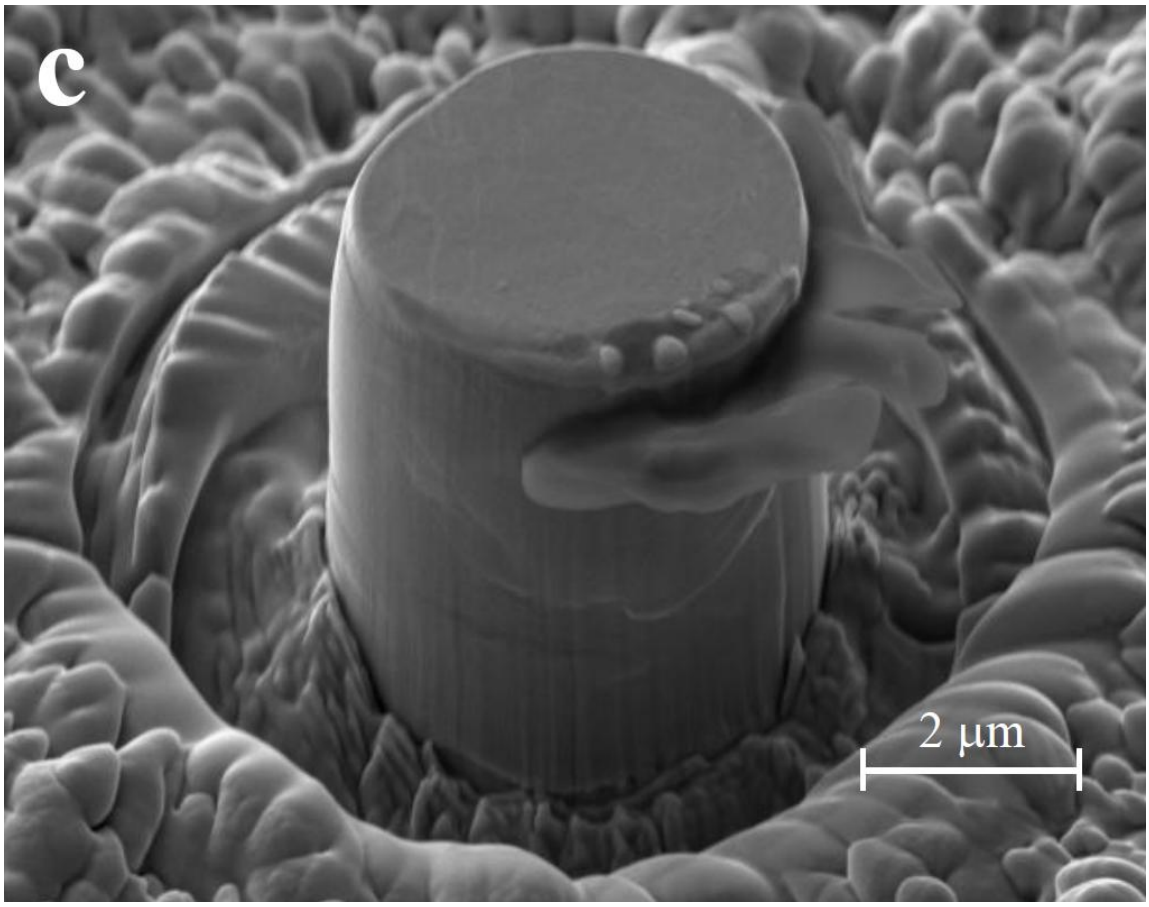

Figure 5.1. SEM images of FIB machined 5 μm diameter Zr 2.5%Nb (transverse-normal) micro-pillars (a) before compression, (b) after compression testing (non-irradiated condition), and (c) after compression testing (Zr^+ irradiated condition). The increased strain localization leading to splitting of the micro-pillar at the final stages of the compression test performed on the Zr^+ irradiated sample is clearly shown in (c).

One sample from each of the three planes was then mounted in a 1.7 MV tandem ion accelerator located at the University of Western Ontario and irradiated with 8.5 MeV Zr^+ ions to a fluence of 7.07×10^{19} ions/m^2 . The irradiations were performed in a vacuum (10^{-11} Pa) with the sample attached to a water-cooled holder in order to minimize the extent of irradiation-induced heating. While the effect of ion beam heating on the local

temperature of the surface region, containing the micro-pillars, of the sample cannot be accurately measured, the direct contact of the small sample with the water-cooled sample-holding stage minimizes the effect of extraneous beam heating.

One set of non irradiated micro-pillars, with the ion-irradiated micro-pillars made in all three directions, were compressed at 25 °C while the second set of non-irradiated micro-pillars were compressed at 300 °C. All micro-pillars were tested in compression with a 10 μm diameter flat diamond punch attached to a nano-indentation testing platform (Micro Materials Ltd., Wrexham, U.K). The flat punch was made from a three-sided pyramidal Berkovich diamond indenter by flattening the indenter tip with FIB-milling. The test sample was attached to a moveable stage located on the nano-indentation testing instrument such that the micro-pillars, each located at the centre of a 60 μm milled circle, could be located with an optical microscope and precisely positioned in front of the indenter. The micro-pillars were then compressed with the flat punch to a pre-specified load at a loading rate of 1 mN/s. For the high temperature tests, a hot stage power supply and hot stage desktop controller was attached to an electric resistance heater located within the sample stage. The sample was mounted on the stage by high temperature cement to ensure that the sample was firmly held intact at the maximum testing temperature of 300 °C. The transfer of heat from the ceramic sample stage to the sample surface was therefore by conduction and heat loss was minimized by surrounding the sample stage and the indenter with insulating material. The heat distribution on the sample surface was allowed to attain equilibrium by allowing it to stay heated for about 6 hours before performing the micro-pillar compression tests. During loading, the applied load and the displacement of the punch were continuously recorded.

5.3. Results and discussions

The true stress versus true strain response of the micro-pillars is shown in Figure 5.2. The 0.2% yield stress values obtained in this study for the non-irradiated samples are very close in magnitude to previously reported data from uniaxial tensile tests performed, at room temperature, in the axial and transverse directions of non-irradiated Zr-2.5%Nb pressure tubes [3]. It should be noted that conventional uniaxial tensile tests cannot be performed in the radial direction of the pressure tubes because of its small thickness;

therefore, the data from our uniaxial micro-pillar compression tests, aligned in the radial direction represent new, and significantly improved, assessment of the overall mechanical anisotropy of this pressure tube material in both the non-irradiated and the irradiated conditions.

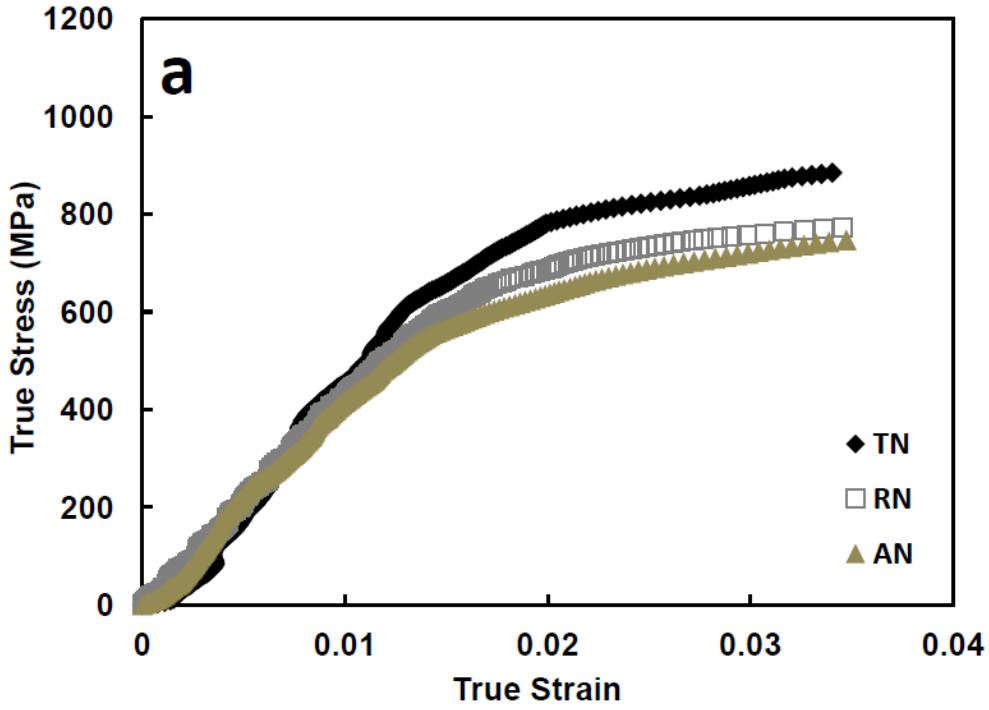

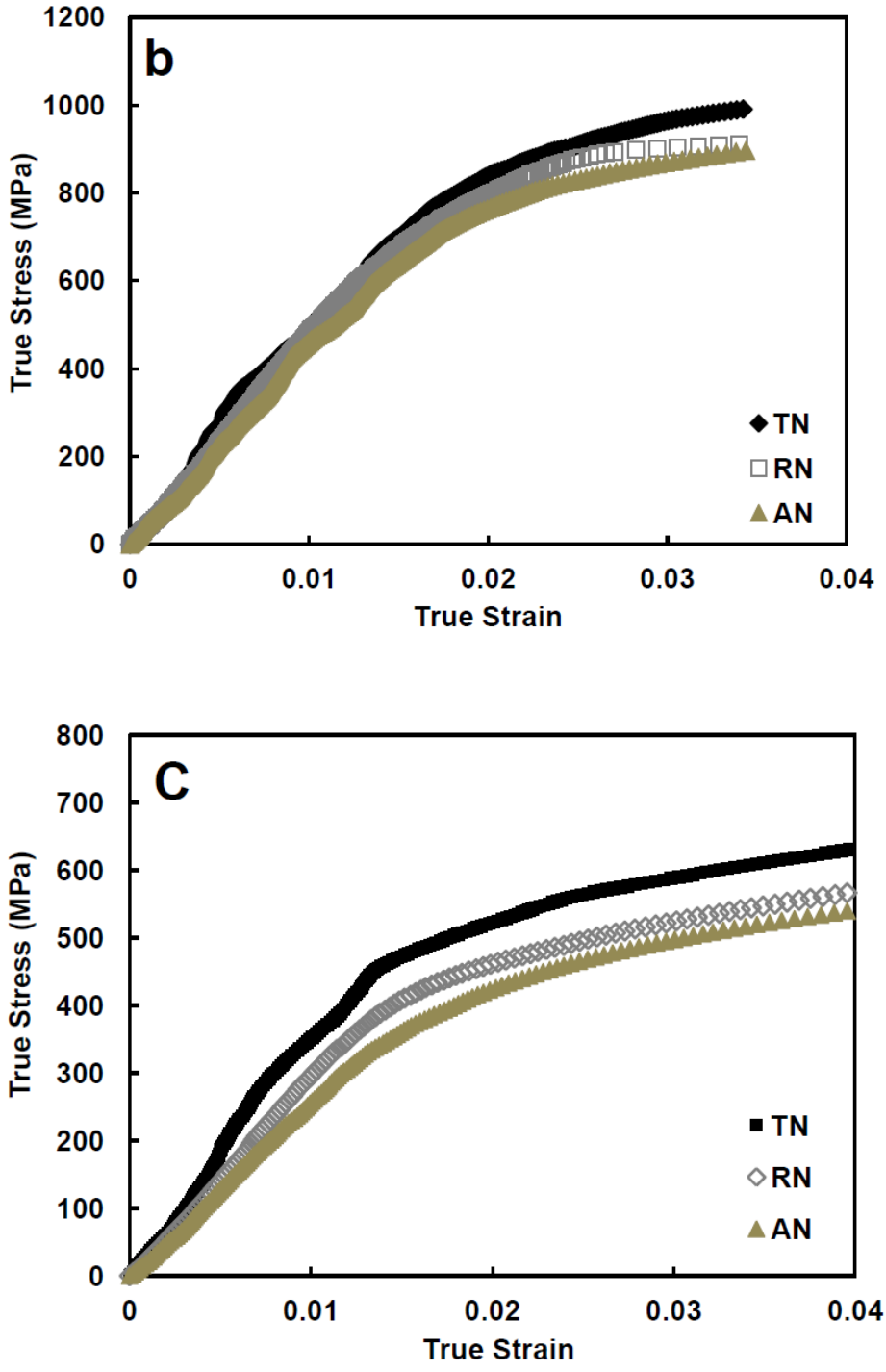

Figure 5.2. Typical true stress versus true strain curves obtained from uniaxial compression of 5 μm diameter Zr-2.5%Nb micro-pillars in: (a) the non-irradiated condition at 25 °C; (b) after Zr^{+} ion irradiation at 25 °C and (c) non-irradiated condition at 300 °C.

Zr^+ irradiation increased both the initial yield stress and the strain hardening rate of the Zr-2.5%Nb test material however the degree of increase differed in the three loading directions that were studied. Zr^+ ion irradiation also promoted localized plastic deformation leading to pillar cracking during the final stages of compression. This was particularly evident in Zr^+ irradiated micro-pillars compressed in the transverse direction of the pressure tube (Figure 5.1c).

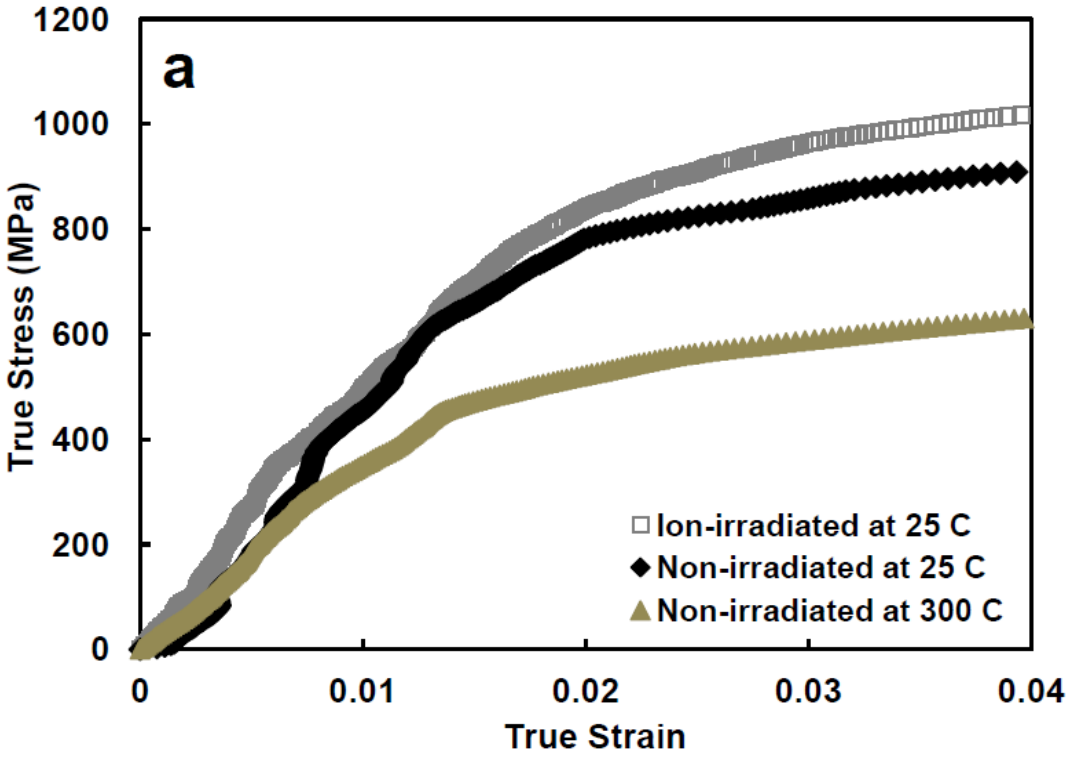

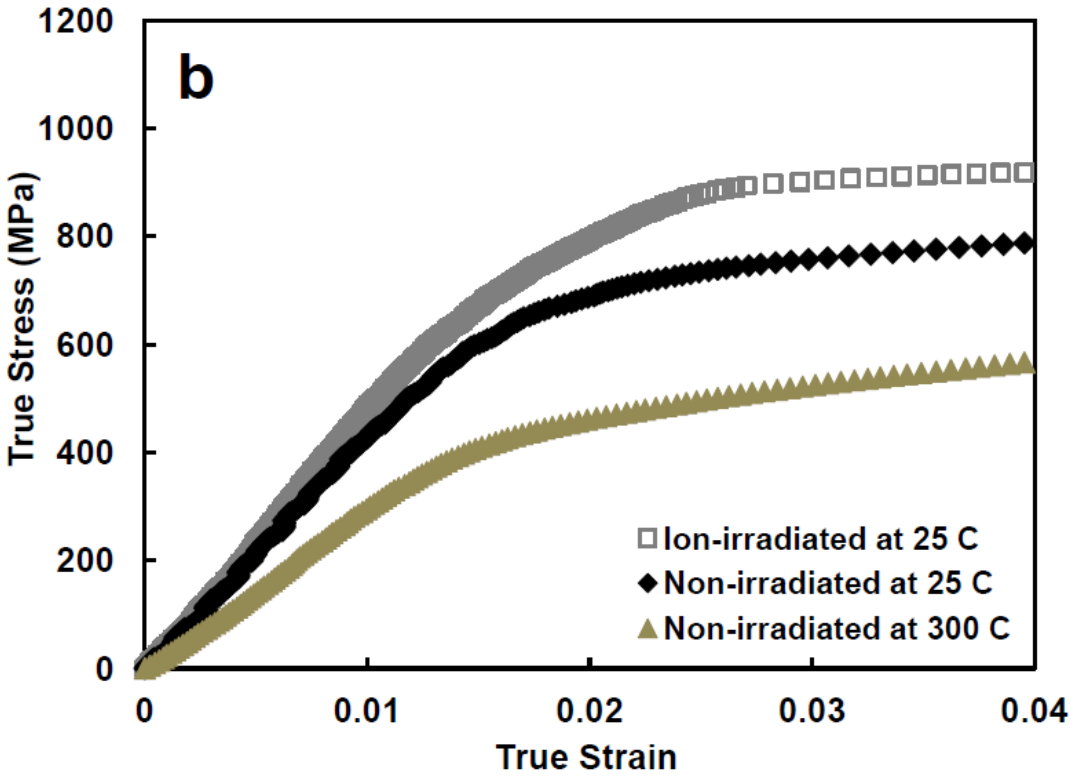
b
1200
1000
800
600
400
200
0
True Stress (MPa)
0
0.01
0.02
0.03
0.04
True Strain
Ion-irradiated at 25 C
Non-irradiated at 25 C
Non-irradiated at 300 C

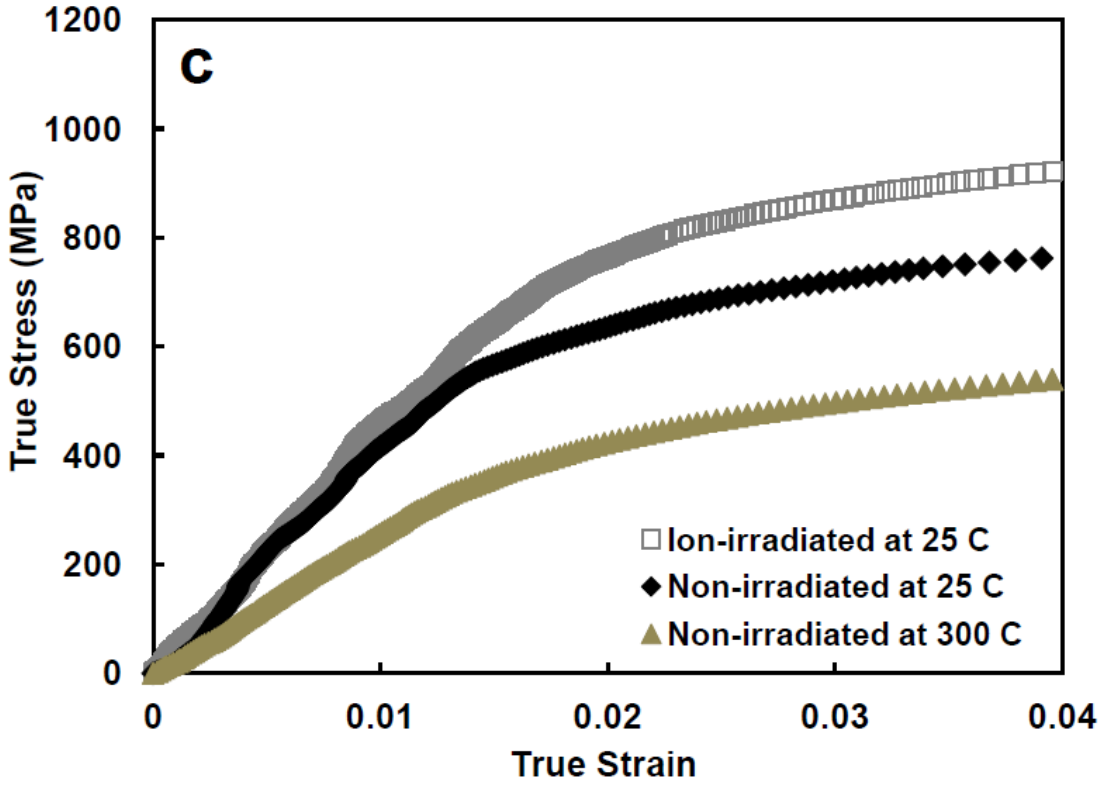

Figure 5.3. The true stress versus true strain curves obtained from uniaxial compression of 5 μm diameter Zr-2.5%Nb micro-pillars in: (a) the transverse normal direction for ion irradiated at 25 °C; non-irradiated at 25 °C and non-irradiated at 300 °C; (b) the radial normal direction under the same conditions as in (a); and (c) the axial normal direction under the same conditions as in (a).

One primary difference between the micro-pillar compression tests performed in each of the three directions is the fraction of basal pole normals aligned parallel to the direction of loading. The flow stress of the Zr-2.5%Nb alloy is considerably higher in a direction in which many (0001) basal pole normals are aligned parallel. Quantification of the degree of crystallographic alignment is commonly performed with x-ray diffraction studies where the x-ray diffraction intensity corresponding to a certain set of crystal planes is measured as a function of angular orientation within the test material. Following the method proposed by Kearns [21] one can determine, from such an

assessment, the "resolved orientation parameter *f*" which essentially expresses the effective fraction of poles aligned parallel to the principal directions of the sample. The orientation distribution of the (0001) basal pole normals within the Zr-2.5%Nb pressure tube material used in this study was assessed with extensive x-ray diffraction measurements and the following resolved basal pole parameters, $f_A = 0.03$, $f_R = 0.34$, and $f_T = 0.62$ were determined.

Figure 5.2c shows that the magnitude of the flow stress decreases significantly with an increase in temperature as should be expected. This is clearly shown in Figures 5.3(a-c) where the ion-irradiated and non-irradiated micro-pillars, compressed at 25 °C, are plotted on the same graph as the non-irradiated micro-pillars compressed at 300 °C. This decrease in flow stress can be attributed to an increase in temperature.

Figure 5.4 shows the dependence of the 0.2% offset yield stress and the strain hardening exponent ($n = d(\log\sigma)/d(\log\varepsilon)$) upon the resolved basal pole parameter in the direction parallel to the loading direction for each of the micro-pillars tested. The trends displayed by the non-irradiated test samples indicate that the yield stress was highest, and the strain hardening exponent was lowest, when the material is loaded in a direction parallel to a large number of basal pole normals.

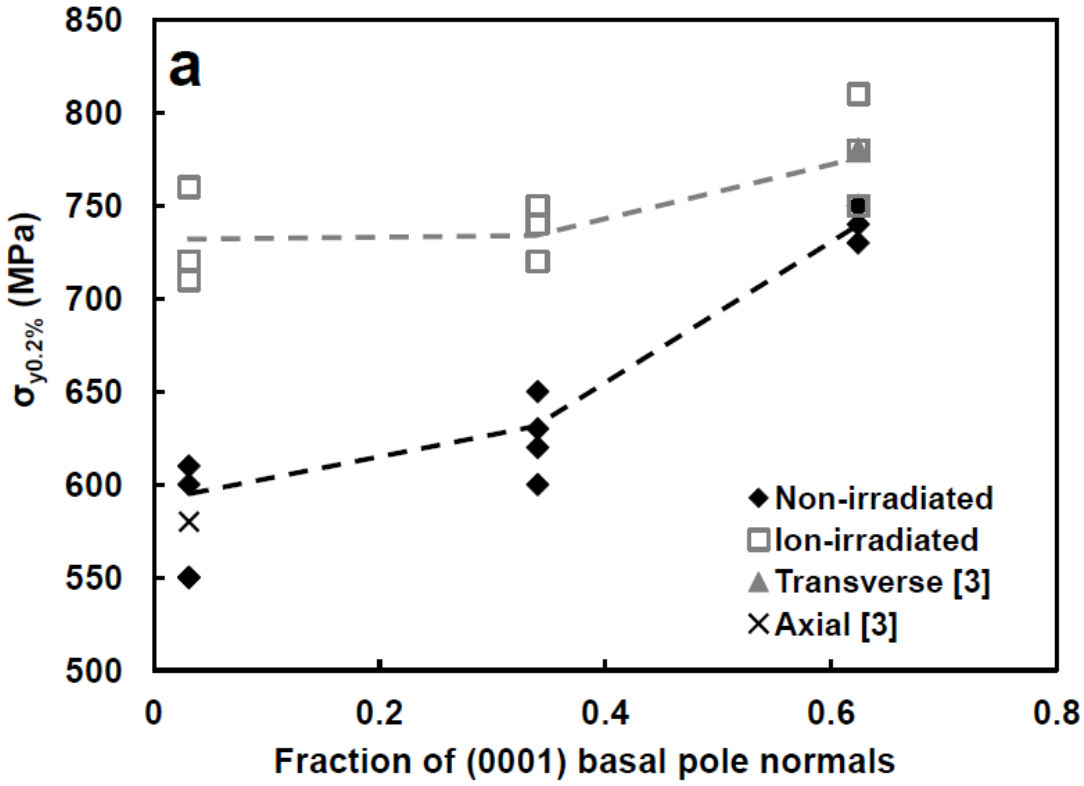
a
850
800
750
700
650
600
550
500
$\sigma_{y0.2\%}$ (MPa)
0
0.2
0.4
0.6
0.8
Fraction of (0001) basal pole normals
Non-irradiated
Ion-irradiated
Transverse [3]
Axial [3]

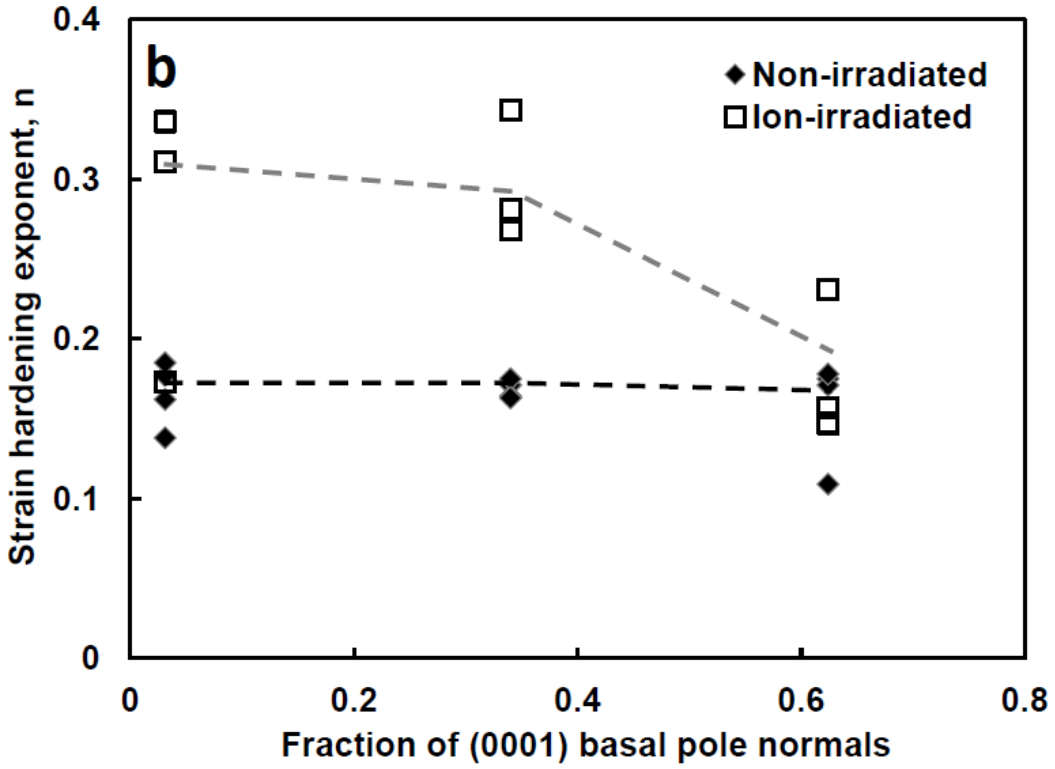

Figure 5.4. Plots of: (a) 0.2% offset yield stress and (b) strain hardening exponent, $n = d\log\sigma / d\log\varepsilon$, versus resolved fraction of (0001) basal poles parallel to the direction of compression for the non-irradiated and the Zr^{+} irradiated micro-pillars. The degree of irradiation hardening and the change in the rate of strain hardening resulting from the irradiation are greatest when deformation occurs in a direction along which few basal poles are parallel. The data from Ref. [3] in (a) are from previously published uniaxial tensile tests performed on non-irradiated Zr-2.5%Nb material and fall on the same trends described by the micro-pillar compression data presented here.

Comparing the data from the non-irradiated samples with those from the Zr^{+} irradiated samples indicates that the increase in both the yield stress and the work hardening rate as a result of Zr^{+} irradiation is considerably larger when the stress is applied in a direction containing a low value of basal pole normals aligned parallel to the loading direction. Since plastic deformation of Zr-2.5%Nb pressure tube material on a direction, such as the

transverse direction, parallel to a high fraction of (0001) basal pole normals is known to occur by a combined process of pyramidal and prismatic dislocation glide while deformation along the axial and radial directions, which are parallel to a much smaller fraction of (0001) basal pole normals, occurs primarily by prismatic dislocation glide, our findings support the observations of others that the effect of ion irradiation on increasing the yield stress and the work hardening rate of this material is reduced when the deformation is forced to occur primarily by pyramidal dislocation slip rather than by prismatic dislocation slip [7- 9].

When we apply the Hill's anisotropy criterion to express the onset of plastic deformation in the form [3]

$$\sigma_{Ayield} = \bar{\sigma} = \sqrt{F(\sigma_{AN-}\sigma_{TN})^2 + G(\sigma_{TN} - \sigma_{RN})^2 + H(\sigma_{RN} - \sigma_{AN})^2} \qquad (5.1)$$

where *AN*, *TN*, and *RN* are the orthogonal directions of the pressure tube. The anisotropy coefficients *F, G,* and *H* can then be expressed in terms of the ratios of the uniaxial yield stress in the *AN*, *TN* and *RN* directions as:

$$F + H = 1 \qquad (5.2a)$$

$$F + G = \left(\frac{\sigma_{AN_{yield}}}{\sigma_{TN_{yield}}} \right)^2 \qquad (5.2b)$$

$$G + H = \left(\frac{\sigma_{AN_{yield}}}{\sigma_{RN_{yield}}} \right)^2 \qquad (5.2c)$$

Using the σ_{yield} values in figure 5.4(a), the values of the anisotropy coefficients before irradiation were: *F = 0.375, G = 0.223, H = 0.625* and after irradiation became *F = 0.445, G = 0.431, H = 0.555.*

Further analysis of the data in Figure 5.4 indicate that the overall scatter in the 0.2% offset yield stress and the strain hardening exponent is relatively small for multiple micro-pillar tests performed under the same conditions. This is despite the fact that the samples were made from relatively widely-spaced regions of the pressure tube and indicates that the effect of i) local microstructural/chemical changes within the test pressure tube material and ii) inherent variability associated with the sensitivity limits of the testing equipment on the measured mechanical properties is small, certainly less than the measured differences resulting from Zr^{+} irradiation. The correspondence of the measured 0.2% offset yield stress of the axial- and transverse-aligned micro-pillars with previously reported values from large sample uniaxial tensile tests, from Ref [3], indicate that the size of the micro-pillars used in this study was sufficiently large that the measured mechanical properties of the micro-pillars did not display significant length-scale effects [20].

5.4. Conclusion

Previous micro-indentation based studies, where the applied stress and strain states are less controlled, have suggested that irradiation damage has a greater effect on deformation by prismatic slip than on deformation by pyramidal slip [6-9]. The data presented in Figures 5.4 support this suggestion by indicating that the change in both the 0.2% offset yield stress and the strain hardening exponent after Zr^{+} irradiation, to a level of 7.07×10^{19} ions/m^2 E = 8.5 MeV, is significantly reduced when increasing basal pole fractions are aligned parallel to the direction of compression. This can also be confirmed by the change in the values of the anisotropy coefficients.

When the group of non-irradiated micro-pillars were compressed at an elevated temperature of 300 °C, which is within the typical working temperature range of a Zr-2.5%Nb CANDU pressure tube, the magnitude of the flow stress decreased significantly in all three directions but the degree of anisotropy in flow stress was retained. The decrease in flow stress has been attributed to the increased thermal energy of the dislocations within the crystal structure which makes dislocation glide more permissible. This temperature (300 °C) falls within the range that has been referred to in previous

studies as the “athermal flow” regime because, over this temperature range, the degree of anisotropy remains constant [3].

The key finding of this study is that the mechanical anisotropy of the highly textured Zr-2.5%Nb alloy is considerably reduced when the alloy is in the irradiation hardened state. These results were obtained by irradiation with self-similar Zr^{+} ions and illustrate that this type of irradiation, along with subsequent testing using uniaxial micro-pillar compression, provides an accurate simulation of neutron irradiation without causing the test material to become radioactive.

It should be noted that the results reported here were obtained from samples that were Zr^{+} irradiated and then mechanically tested at room temperature, 25^{o}C. The effect of irradiation and mechanical testing at elevated temperatures, for example temperature typical of the interior of a nuclear reactor core, may be quite different than at 25^{o}C due to concurrent thermal annealing of the irradiation damage. The effect of temperature on the Zr^{+} irradiation hardening of Zr-2.5%Nb micro-pillars is the subject of our ongoing research.

Acknowledgements

The authors wish to thank the Natural Science and Engineering Research Council of Canada (NSERC) and the University Network of Excellence in Nuclear Engineering (UNENE) who provided financial support for this research. The assistance of Dr. T. Simpson of the University of Western Ontario Nanofabrication Laboratory in preparing the micro-pillars and Dr. S. St Lawrence (AECL) for reviewing this manuscript and providing helpful suggestions is also gratefully acknowledged.

References

[1] P.A. Ross-Ross, W. Evans, W.J. Langford, Atomic Energy of Canada Ltd. Research Report, AECL-4262 (1972) 1.

[2] N. Christodoulou, P.A. Turner, C.N. Tomé, C.K. Chow, R.J. Klassen, Metall. Mater. Trans. A 33 (2002) 1103.

[3] N. Christodoulou, P.A. Turner, E.T.C. Ho, C.K. Chow, M.R. Levi, Metall. Mater. Trans. A 31A (2000) 409.

[4] B.S. Rodchenkov, A.N. Semenov, Nucl. Eng. Des. 235 (2005) 2009.

[5] D.D. Himbeault, C.K. Chow, M.P. Plus, Metall. Mater. Trans. A 25 (1994) 135.

[6] M. Nakatsuka, M. Nagai, J. Nucl. Sci. Technol. 24 (1987) 832.

[7] M. Nakatsuka, M. Nagai, J. Nucl. Sci. Technol. 24 (1987) 906.

[8] S.T. Mahmood, S.A. Hussien, P.S. Godavarti, K.L. Murty, Effects of Radiation on Materials, in: 15th Int. Symp., ASTM, STP 1125 (1992) 337.

[9] X. Wei, J.R. Theaker, M. Griffiths, Zirconium in the Nuclear Industry, 15th Int. Symp., ASTM, STP 1505 (2009) 583.

[10] B. Bose, R.J. Klassen, J. of Nucl. Mat. 405 (2010) 138.

[11] R.A. Holt, M. Griffiths, R.W. Gilbert, J. of Nucl. Mat. 149(1987) 51.

[12] A. Akhtar, J. of Nucl. Mat. 47(1973) 79.

[13] M. Griffiths, J. of Nucl. Mat. 205(1993) 225.

[14] M.D. Uchic, D.M. Dimiduk, J.N. Florando, W.D. Nix, Science 305 (2004) 986.

[15] J.R. Greer, W.C. Oliver, W.D. Nix, Acta Mater. 53 (2005) 1821.

[16] J. Michler, K. Wasmer, S. Meier, F. Ostlund, K. Leifer, Appl. Phys. Lett. 90 (2007) 043123.

[17] S. Korte, W.J. Clegg, Scripta Mater. 60 (2009) 807.

[18] A. Rinaldi, P. Peralta, C. Friesen, K. Sieradzki, Acta Mater. 56 (2008) 511.

[19] J.R. Greer and W.D. Nix, Appl. Phys. A 80 (2005) 1625.

[20] J.R. Greer and W.D. Nix, Phys. Rev. B 73 (2006) 245410.

[21] J.J. Kearns, Report No. WAPD-TM-472, Westinghouse Co., Pittsburgh PA, 1965.

Chapter 6

Discussions and future work

6.1 Discussions

This chapter discusses observations and provides further interpretation to the results obtained from the analysis of data from experiments performed on the Zr-2.5%Nb CANDU pressure tube during the course of this study. As has been stated previously in this thesis, the primary aims of carrying out this research were to:

- Explore the possibility of developing new and effective small-specimen testing techniques to facilitate the in-cell mechanical characterization of highly radioactive Zr-2.5%Nb pressure tube material from a CANDU nuclear reactor.
- Characterize the mechanical properties in the *RN* direction of the pressure tube over the temperature range from 25^{o}C to 300^{o}C since the mechanical properties in this direction have not been thoroughly studied.
- Assess the mechanical anisotropy of the CANDU pressure tube with the intention of applying the results in characterizing irradiated metallic components from the core of the nuclear reactor.
- Applying Zr^{+} irradiation to simulate the effect of neutron irradiation on the mechanical strength and anisotropy of the pressure tube.
- Examining the effect of temperature, up to 300^{o}C, on the strength and anisotropy of the pressure tube especially at the reactor core operating temperature.

It was stated during this study that the mechanical anisotropy of this pressure tube was a result of the combination of the inherent mechanical anisotropy of the base hcp Zirconium metal and the large amount of crystallographic texture invoked during the hot extrusion and cold drawing steps of the pressure tube fabrication. While it may be difficult to determine from our present analysis, what percentage of the anisotropy results from its hcp crystal structure, there is enough evidence to show that the extrusion at a ratio of 10:1 and the subsequent 27% cold-drawing induces a strong texture with a high

fraction of the <0001> basal pole normals aligned along the transverse (circumferential) direction of the tube [1-4].

Results presented in chapter 3 from experiments performed in this study showed that the magnitude of the flow stress of a non-irradiated Zr-2.5%Nb CANDU pressure tube was highest in the *TN* direction than in the *RN* and *AN* directions. This is expected as the mechanical yield stress of this pressure tube should be highest in the direction containing the highest proportion of <0001> basal plane normals and can be attributed to the fact that the hcp α-phase Zirconium has a higher yield stress when compressed along the <0001> direction than along any other direction.

The Zr-2.5%Nb CANDU pressure tube has been designed on purpose to have this kind of texture, thus providing greater resistance to applied transverse "hoop" stress, induced by internal pressurization, during reactor operation. This anisotropic mechanical behavior though, results in substantially increased difficulty in predicting the yield behavior of the pressure tube material when subjected to more complex multi-axial applied stress states. In this study, I have used the 1948 Hill's yield criterion (Eq. 3.1a) to describe the equivalent flow stress $\bar{\sigma}$ for the mechanically anisotropic Zr-2.5%Nb tube. The data from uniaxial compression tests performed on the pressure tube over a temperature from 25^{o}C to 300 °C were used to determine the anisotropy coefficients *F*, *G*, and *H*. This method of determining anisotropy is well suited for rolled sheets, pipes and extruded bars and is therefore well suited for the pressure tube material used for this investigation.

An important subject of discussion is the competing mechanisms of dislocation motion in Zirconium's hcp crystal structure during plastic deformation. When deformation occurs by a twinning mechanism, a region of the lattice undergoes a bulk misorientation and the resulting lattice is a mirror image of the surrounding untwined lattice. While twinning and the more common dislocation slip deformation mechanisms can both occur in a crystal, there are differences between both mechanisms. Under the application of a shear stress, the orientation of the crystal around the slip plane does not change during slip, but for twinning, there will be an abrupt change in the lattice orientation. Also, in slip, atom movements are usually in multiple atomic distances and occur on relatively widely

separated planes while twinning results in displacements that are a fraction of an atomic distance and involves every atomic plane within the twinned region [5-6].

Studies on the plastic deformation behavior of pure Zirconium and the Zr-2.5%Nb pressure tube alloy have suggested that there is the occurrence of twinning during the uniaxial plastic deformation in some directions especially at high levels of plastic strain [7-9]. The analysis carried out in this study was limited to deformation of the Zr-2.5%Nb pressure tube at plastic strain level less than 10%. No attempts was therefore made to measure the texture of the deformed samples or to prepare transmission electron microscope (TEM) foils from sections of the plastically deformed material to determine the frequency of twinning during the plastic deformation of our samples. These are therefore important suggested areas for future studies.

The results from the uniaxial compression tests on the cylindrical macro-pillars presented in Chapter 3 of this study and results from the spherical micro-indentation tests presented in Chapter 4 clearly display a close agreement with each other and with those found in the published literature. It was important to first perform the uniaxial compression tests to obtain stress strain curves under a simple uniaxial stress state and these results served as a basis for comparing stress values obtained from subsequent multi-axial loadings invoked during the spherical micro-indentation tests.

The results from the micro-pillar compression testing provided a basis for using Zr^{+} irradiation to simulate the effect of neutron irradiation on the anisotropy of the yield stress of the Zr-2.5%Nb CANDU pressure tube material. The results from these tests were important as they clearly show that this method of micro-mechanical testing using micrometer-sized pillars can be used to characterize the mechanical properties of materials. Again, stress–strain curves from our macro-pillar compression tests were important as they served as a basis for comparison with those from non-irradiated micro-pillars compression tests.

It can be concluded that this thesis has successfully explored new methods for testing the mechanical properties of the anisotropic extruded and cold-drawn Zr-2.5%Nb CANDU pressure tube material both in the non-irradiated and the Zr^{+} irradiated conditions. Three

different experimental procedures were used to carry out these investigations: Two of the experiments were based upon the use of uniaxial compression of macro- and micro-sized cylindrical pillars while the third was based on a novel technique that uses spherical indentation to deduce the stress-strain behavior. These techniques were applied in this research to assess the effect of temperature and irradiation hardening on the mechanical anisotropy of an as-received Zr-2.5%Nb CANDU pressure tube material supplied by Atomic Energy of Canada Ltd.

The first experimental analysis of this thesis (Chapter 3) was based on uniaxial compression tests performed on multiple cylindrical specimens of, 2mm diameter and 3mm length that were deformed to various levels of plastic strain. The results were used to assess the true stress versus true plastic strain response in the Axial (*AN*), Radial (*RN*), and Transverse (*TN*) directions of the Zr-2.5%Nb pressure tube over the temperature range from 25 to 300^{o}C. Analysis of the data resulted in the determination of the Hill's anisotropy coefficients $F=0.38 \pm 0.01$, $G=0.202 \pm 0.001$, and $H=0.62 \pm 0.01$. These coefficients were found to be independent of temperature and plastic strain over the range of temperature from 25 to 300^{o}C and plastic strain up to 10%.

Application of the experimentally determined *F*, *G*, and *H* values to calculate the equivalent stress $\bar{\sigma}$ and equivalent plastic strain $\bar{\varepsilon}_p$ demonstrated that stress – strain data obtained from uniaxial tests performed in the *AN*, *RN*, and *TN* directions all fell on a single $\bar{\sigma}$ versus $\bar{\varepsilon}_p$ curve. This was also demonstrated to be true when previously reported uniaxial stress – strain data, from tests performed in the *AN* and *TN* directions, was similarly analysed with the *F*, *G*, and *H* values obtained from this study.

The results from this study are scientifically significant since they are, to the best of my knowledge, the first experimentation-based determination of the Hill's anisotropy coefficients *F*, *G*, and *H* of extruded and cold-drawn Zr-2.5%Nb CANDU pressure tube material over a wide temperature range extending up to the 300^{o}C in-service temperature of this tubing. These anisotropy coefficients can be directly useful in numerical models of Zr-2.5%Nb pressure tube components where calculating the onset of plastic deformation is of interest.

The second experiments (Chapter 4), developed a method of analysis by which the average flow stress σ_{avg} and the average plastic strain ε_{avg} could be obtained from the *F* - *h* data from spherical indentation tests performed on the mechanically anisotropic Zr-2.5%Nb CANDU pressure tube material over the range of temperature from 25°C to 300°C. We performed spherical indentation tests, at each temperature, on the *AN*, *RN*, and *TN* planes of the tube. The *F* - *h* data were used, along with determined values of the Hill's anisotropy coefficients from our uniaxial compression tests and strain hardening exponents from our micro-pillar compression tests of this material, to calculate σ_{avg} and ε_{avg} using equations developed to describe the spherical indentation of an isotropic material, by modifying σ_{yield} in the non-dimensional parameter ϕ.

SEM images of indentations made on the *AN*, *RN* and *TN* planes of the Zr-2.5%Nb pressure tube showed that while spherical indentation of a mechanically isotropic material will result in a circular residual indentation, the indentations on this material were slightly elongated in the direction, on the plane of the indentation, of lowest σ_{yield}. It was observed that the direction of lower yield stress undergoes more plastic strain that results in a greater material pile-up which causes the indentation to appear slightly elongated in this direction.

The resulting σ_{avg} - ε_{avg} plots for indentation tests performed, with a 200 μm diameter sphere, at temperature from 25°C to 300°C indicate that this method of analysis results in the data from spherical indentations performed on the *AN*, *RN*, and *TN* planes bearing a close correspondence to the flow curves obtained from uniaxial compression tests. This confirms that this method of analysis can serve as a reliable alternative to conventional tensile and compression tests to obtain flow stress – plastic strain curves from small samples of mechanically anisotropic material with minimal sample preparation. This will be a potentially very useful test method for a variety of applications such as in-cell mechanical testing of radioactive nuclear materials.

Spherical micro-indentation tests were also performed with a small, 40 μm diameter, sphere to assess the indentation depth limitations of the proposed data analysis technique.

Comparison of the σ_{avg}-ε_{avg} plots from the deep, large diameter, spherical indentations with those from the shallow, small diameter, indentations indicates that there is a significantly different stress-strain response when the indentation depth is less than 4 μm. One clear difference is that, for the small diameter spherical indentations, σ_{avg} is largest, for a given ε_{avg}, for indentations made on the *AN* plane while σ_{avg} is largest, for indentations made on the *TN* plane when deep indentations are made with the large diameter sphere. This suggests that the local plastic strain distribution around the spherical indentation is dependent upon indentation depth and that the proportion of lateral-to-axial plastic strain during spherical indentation changes with indentation depth and possibly with increasing diameter of the indentation.

Plots of σ_{avg}-ε_{avg} curve obtained from the shallow, small diameter, indentations indicate that when the indentation depths is less than several micrometers the calculated σ_{avg} is heavily influenced by the depth dependence of the yield strength of the material and this may overshadow its dependence upon ε_{avg}.

In the third set of experiments (Chapter five), Zr^{+} irradiation was used to simulate the effect of neutron irradiation on the microstructure of Zr-2.5%Nb pressure tube samples made from the *AN*, *RN* and *TN* directions. Results from previous micro-indentation based studies, where the applied stress and strain states are less controlled, have suggested that irradiation damage has a greater effect on deformation by prismatic slip than on deformation by pyramidal slip. The data presented in Figure 5.4 supported this suggestion by indicating that the change in both the 0.2% offset yield stress and the strain hardening exponent after Zr^{+} irradiation, to a level of 7.07×10^{19} ions/m^2 E = 8.5 MeV, was significantly reduced when increasing basal pole fractions were aligned parallel to the direction of compression. This could also be observed in the change in values of the anisotropy coefficients.

When the group of non-irradiated micro-pillars were compressed at an elevated temperature of 300 °C, which was within the typical working temperature range of a Zr-2.5%Nb CANDU pressure tube, the magnitude of the flow stress decreased significantly

in all three directions but the degree of anisotropy in flow stress was retained. The decrease in flow stress has been attributed to the increased thermal energy of the dislocations within the crystal structure which made dislocation glide more permissible. This temperature (300 °C) falls within the range that has been referred to in previous studies as the "athermal flow" regime because, over this temperature range, the degree of anisotropy remains constant.

The key finding of our third experiments is that the mechanical anisotropy of the highly textured Zr-2.5%Nb alloy is considerably reduced when the alloy was in the irradiation hardened state. These results were obtained by irradiation with self-similar Zr^{+} ions and illustrated that this type of irradiation, along with subsequent testing using uniaxial micro-pillar compression, could provide an accurate simulation of neutron irradiation without causing the test material to become radioactive.

6.2 Future work

The ultimate goal of this research was to develop new methods, some of which could be used as in-cell automated testing techniques, for assessing the mechanical response of radioactive nuclear materials.

For micro-pillar compression testing, I suggest the irradiation of the pillars be carried out at reactor operating temperature (260 – 300 °C) to investigate any change in the mechanical anisotropy of the material. Previous tests carried out using pyramidal indentation demonstrated that there will be a small change. However, it will be useful to the nuclear research community if these tests were performed using uniaxial compression testing, since the stress state during indentation testing is complex because of its triaxial nature. The effect of irradiation at elevated temperatures has been found to be different than at 25^{o}C and the difference has been attributed to concurrent thermal annealing of the irradiation damage. The result obtained may therefore improve our understanding of the behavior of this material at reactor operating temperature. It could also be interesting to make TEM samples from compressed non-irradiated and irradiated micro-pillars to investigate the difference in microstructure especially with regards to the observed increase in strain localisation of the irradiated pillars.

For spherical micro-indentation testing, I suggest applying Finite Element Analysis for determining the value of the constraint factor ψ from the non-dimensional parameter ϕ. This would possibly improve the accuracy of the σ_{avg} results obtained from the measured mean contact pressure P_m.

Finally, I suggest preparing transmission electron microscope (TEM) foils from sections of the plastically deformed samples to determine the frequency of twinning during the plastic deformation of the compressed samples. This will help clarify the subject of the occurrence or otherwise of twinning in the samples during plastic deformation.

References

[1] B.A. Cheadle, C.E. Ells, W. Evans, J. Nucl. Mater. 23 (1967) 199.

[2] B. A. Cheadle, S.A. Aldridge, C.E. Ells, Can. Metall. Quart. 11 (1972) 121.

[3] R.A. Holt, P. Zhao, J. Nucl. Mater. 335 (2004) 520.

[4] W.K. Alexander, V. Fidleris, R.A. Holt in: Proceedings of 3rd International symposium on Zirconium in the Nuclear Industry, ASTM STP 633, 1977, p. 344.

[5] W.F. Hosford, The Mechanics of Crystals and Textured Polycrystals, Oxford Science Publications, 1993.

[6] G.E. Dieter, Mechanical Metallurgy, McGraw-Hill Book Company, 1988.

[7] R.J. McCabe, G. Proust, E.K. Cerreta, A. Misra, Int. J. Plast., 25 (2009) 454.

[8] A. Salinas-Rodriguez, J.H. Root, Txt. Microsc. 14 (1991) 1239.

[9] D.D. Himbeault, C.K. Chow, M.P. Puls, Metall. Mater. Trans. A 25 (1994) 135.

Curriculum Vitae

Name	Richard O. Oviasuyi
Post-secondary Education and Degrees	University of Benin Benin City, Edo State, Nigeria 1993 – 1999 B. Eng. The University of Western Ontario London, Ontario, Canada 2007 – 2008 M. Eng. The University of Western Ontario London, Ontario, Canada 2008 – 2012 PhD
Honours and Awards	Western Engineering Scholarship 2008 – 2009, 2009 – 2010, 2010 – 2011
Related work Experience	Research Assistant The University of Western Ontario London, Ontario, Canada 2008 – 2012 Teaching Assistant The University of Western Ontario London. Ontario, Canada 2008 - 2011
Publications	R.O. Oviasuyi, R.J. Klassen, Anisotropic deformation of Zr ion irradiated Zr-2.5%Nb micro-pillars at 25 °C, Journal of Nuclear materials, 421 (2012) 54 R.O. Oviasuyi, R.J. Klassen, Assessment of the anisotropic flow stress and plastic strain of Zr-2.5%Nb pressure tubes at temperature from 25 °C to 300 °C, Manuscript under review in Journal of Nuclear Materials (2012) R.O. Oviasuyi, R.J. Klassen, Deducing the stress – Strain response of anisotropic Zr-2.5%Nb pressure tubing by spherical indentation testing, Manuscript under review in Journal of Nuclear Materials (2012)